



UNIVERSITÀ DEGLI STUDI DI GENOVA
FACOLTÀ DI SCIENZE MATEMATICHE, FISICHE E NATURALI
SCUOLA DI DOTTORATO IN SCIENZE E TECNOLOGIE
PER L'INFORMAZIONE E LA CONOSCENZA
XXIV CICLO, A.A. 2009 - 2012



A THESIS SUBMITTED FOR THE DEGREE OF
Dottore di Ricerca in
Fisica

MEASUREMENT OF THE *pep* AND CNO SOLAR
NEUTRINO INTERACTION RATES IN BOREXINO

SCHOOL COORDINATOR
Prof. Lorenzo Mattera
Università degli Studi di Genova

AUTHOR
Stefano Davini
Università e sezione INFN di Genova

ADVISOR
Prof. Marco Pallavicini
Università e sezione INFN di Genova

EXTERNAL ADVISOR
Prof. Cristiano Galbiati
Princeton University

AREA 02 - SCIENZE FISICHE
SETTORE SCIENTIFICO-DISCIPLINARE: 02/A1

Introduction

All matter around us is mainly constituted by three particles: protons and neutrons, which make up the atomic nucleus, and electrons, which form the atomic shell. The Universe, however, reveals a great deal of other particles, present from its very beginning, immediately after the Big Bang. Among the still existing particles, one of the strangest and most elusive is the neutrino.

Neutrinos (ν) are neutral particles with a very low mass, which permeate the Universe and are constantly produced in many processes involving radioactive decays as well as nuclear fusion in stars. The most powerful neutrino source near the Earth is the Sun. In the core of the Sun, a series of nuclear reactions produce neutrinos. Two distinct processes, the main proton-proton (pp) fusion chain and the sub-dominant carbon-nitrogen-oxygen (CNO) cycle, are responsible for the solar energy production. In such processes, electron neutrinos (ν_e) with different energy spectra and fluxes are generated. The Sun is producing a great amount of neutrinos: the solar neutrino flux at the Earth distance is about $6 \times 10^{10} \text{ cm}^{-2}\text{s}^{-1}$.

Because neutrinos interact only via the weak interaction, they can easily penetrate huge thicknesses of matter while keeping their original features, thus allowing the study of phenomena directly connected to their origin. Indeed, while photons produced in the fusion take some hundred thousand years to travel across the $7 \times 10^5 \text{ km}$ solar radius, neutrinos take a bit more than 2 seconds. After an additional 8 minutes they reach the Earth, providing precious information concerning energy production processes in the Sun and stars in general.

Since 1970's, solar neutrino experiments have proved to be sensitive tools to test both astrophysical and elementary particle physics models. The experimental observation of neutrinos is extremely complex due to the very low interaction rates of the neutrino with matter. In order to face this problem, huge experimental detectors have been realized and placed in underground areas to avoid the background generated by cosmic rays. Solar neutrino detectors were first built to demonstrate that the sun is powered by nuclear fusion reactions. Until mid 2011, only ${}^7\text{Be}$ (from the reaction $e^- + {}^7\text{Be} \rightarrow {}^7\text{Li} + \nu_e$), ${}^8\text{B}$ (from the reaction ${}^8\text{B} \rightarrow {}^8\text{Be} + e^+ + \nu_e$), and indirectly pp (from the reaction $p + p \rightarrow {}^2\text{H} + e^+ + \nu_e$) solar neutrino fluxes from the proton-proton chain have been measured.

The number of solar ν_e observed in the experiments carried out for several years has always been lower than the one predicted by the astrophysical model which describe the behaviour of the Sun, the Standard Solar Model. The solution to this *solar neutrino problem* is neutrino oscillation. The phenomenon considers the possibility that the three types of existing neutrino (ν_e , ν_μ and ν_τ) can change their flavor while travelling.

Experiments involving solar neutrinos and reactor anti-neutrinos have shown that solar neutrinos undergoes flavor oscillation: a solar neutrino, born as a ν_e , may change flavor in the propagation from the Sun core to the terrestrial detector. If the experimental detectors devoted to study solar neutrinos are designed to detect only (or mainly) electron neutrinos, there will be a relevant decrease in the amount of neutrinos measured on the Earth. Such decrease explain the difference between the expected value of the theoretical models and the experimental data.

Results from solar neutrino experiments are consistent with the so called Mikheyev-Smirnov-Wolfenstein Large-Mixing-Angle (MSW-LMA) oscillation model, which predicts a transition from vacuum-dominated to matter-enhanced oscillations, resulting in an energy dependent electron neutrino survival probability (P_{ee}). Non-standard neutrino interaction models formulate P_{ee} curves that deviate significantly from MSW-LMA, particularly in the 1-4 MeV transition region. The mono-energetic 1.44 MeV *pep* solar neutrinos, generated in the reaction $p + e^- + p \rightarrow {}^2\text{H} + \nu_e$ which belong to the *pp* chain and whose Standard Solar Model predicted flux has one of the smallest uncertainties, are an ideal probe to evidence the MSW effect and test other competing oscillation hypotheses.

The detection of neutrinos resulting from the CNO cycle has important implications in astrophysics, as it would be the first direct evidence of the nuclear process that is believed to fuel massive stars. The total CNO solar neutrino flux is similar to that of the *pep* neutrinos, but its predicted value is strongly dependent on the inputs of the solar modelling, being 40% higher in the High Metallicity (GS98) than in the Low Metallicity (AGSS09) solar model. The measurement of the CNO solar neutrino flux may help to resolve the *solar metallicity problem*.

The Borexino experiment at Laboratory Nazionali del Gran Sasso is designed to perform solar neutrino spectroscopy below 2 MeV. The key feature that allow Borexino to pursue this physics program is its ultra low background level. The Borexino detector employs a target mass of ~ 300 tons of organic liquid scintillator, contained inside a 13.7 m diameter steel sphere, which in turn is located in a steel tank filled with ultra-pure water, in order to reduce the background arising from the natural radioactivity of the mountain rock. A solar neutrino, while interacting with an electron inside the target mass, induces the emission of scintillation light which is detected by the ~ 2000 photo-multipliers tubes (PMTs) placed in the inner surface of the steel sphere. The amount and the time pattern of PMT hits in each event allows respectively to reconstruct the energy of the recoiled electron and the position of the scattering interaction. The potential of Borexino has already been demonstrated in the high precision measurement of the 862 keV ${}^7\text{Be}$ solar neutrino flux.

This thesis is devoted to the first direct measurement of the *pep* and CNO solar neutrino interaction rate in the Borexino experiment. The detection of *pep* and CNO solar neutrinos in Borexino requires novel analysis techniques, as the expected signal interaction rate in is only a few counts per day in a 100 ton target, while the dominant background in the relevant energy region, the cosmogenic β^+ emitter ${}^{11}\text{C}$, produced in the scintillator by cosmic muon interactions with ${}^{12}\text{C}$ nuclei, is about 10 times higher.

The experimental activity

The Ph.D. work presented in this thesis has been carried out within the Borexino collaboration. My activity started on January 2009 and was carried out up to the end of 2011.

My main contributions throughout this period has been on the tuning of the Monte Carlo simulation of the Borexino detector and on the measurement of the *pep* and CNO solar neutrino interaction rates.

In the context of the Monte Carlo simulation of Borexino, my main contribution has been the high precision tuning of the energy and time response of the detector. This has been performed by improving the code related to the simulation of physical processes and the response of the electronics and tuning the related parameters. The accuracy of the simulation has been verified with data obtained during the detector calibration campaign, which I participated.

I have been leading the analysis of the *pep* and CNO neutrino rate with another graduate student, Alvaro Chavarria. In this context, my contributions have been mainly in the development, test and tuning of novel techniques for removing the ^{11}C cosmogenic background (the Three Fold Coincidence method and β^+/β^- pulse shape discrimination), the development of the probability density functions used in the fit, the development and test of the multivariate likelihood used in the analysis, and the evaluation of the statistical significance of the measurement and systematic uncertainties.

Such contributions led to the necessary sensitivity to provide the first direct detection of the *pep* solar neutrinos and the best limits on the CNO solar neutrino flux up to date. The results have been published in Physical Review Letters [1] and highlighted with a Synopsis by the APS.

The thesis layout

Chap. 1 presents a review of the current status of neutrino oscillations. The neutrino oscillations in vacuum and matter are introduced, and the phenomenology of neutrino oscillations is discussed.

In Chap. 2 the Standard Solar Model and the MSW effect are described. The observations of solar neutrinos, the discovery of solar neutrino oscillations and the current understanding of the MSW-LMA oscillation scenario are reviewed.

Chap. 3 reviews the detection of solar neutrinos in the Borexino experiment.

Chap. 4 presents a description of the Borexino detector response and its Monte Carlo simulation. The tuning of the the energy and time response of the detector simulation is described.

Chap. 5 reports on the analysis of the *pep* and CNO solar neutrino interaction rate in Borexino, which led to the first direct measurement of the *pep* solar neutrino flux and the best limit of the CNO solar neutrino flux to date.

Contents

1	Neutrino oscillations	1
1.1	Introduction	1
1.2	Neutrinos in the Standard Model of particle physics	3
1.3	Neutrino mixing and oscillations	4
1.4	Matter effects in neutrino oscillations	8
1.5	Phenomenology of neutrino oscillations	10
1.6	Conclusions and outlook	13
2	Solar neutrino observations	15
2.1	Introduction	15
2.2	The Standard Solar Model	15
2.3	The Solar Metallicity Problem	17
2.4	Production of solar neutrinos	18
2.4.1	The pp chain	19
2.4.2	The CNO chain	22
2.5	Propagation of solar neutrinos	23
2.6	Detection of solar neutrinos	26
2.7	Oscillation of solar neutrinos	28
2.8	Conclusions and outlook	29
3	The Borexino experiment	31
3.1	Introduction	31
3.2	Neutrino detection in Borexino	33
3.3	General description of the Borexino detector	35
3.4	Scintillation light in Borexino	37
3.4.1	Ionization quenching for electrons, α , and γ -rays	38
3.4.2	Time response and α/β discrimination	39
3.4.3	Positron interactions and discrimination	40
3.5	The Borexino energy spectrum	41
4	The Borexino detector response and simulation	45
4.1	Introduction	45
4.2	The Monte Carlo simulation and the physics modelling of Borexino detector	46
4.2.1	The event generation	47
4.2.2	The energy loss	49
4.2.3	The light generation	49

4.2.4	The light tracking	51
4.2.5	Photomultipliers and light guides	52
4.2.6	The electronic simulation	53
4.2.7	The reconstruction program	54
4.3	The tuning of the Borexino Monte Carlo	55
4.3.1	The calibration data	57
4.3.2	Tuning of the time response	58
4.3.3	Tuning of the energy response	60
4.4	Conclusions and outlook	64
5	Measurement of the pep and CNO solar neutrino interaction rates in Borexino	67
5.1	Introduction	67
5.2	pep ν and CNO ν s signals	68
5.2.1	pep ν signal	68
5.2.2	CNO ν s signal	68
5.3	Radioactive backgrounds	71
5.3.1	Radiogenic internal backgrounds	71
5.3.2	Cosmogenic backgrounds	73
5.3.3	External γ -ray backgrounds	75
5.4	Data selection	77
5.5	Event Selection	77
5.5.1	Selection of point-like scintillation events	77
5.5.2	Fiducial volume definition	78
5.5.3	Three-fold coincidence veto	81
5.5.4	Statistical subtraction of α -like events	84
5.6	Energy variables	84
5.6.1	Echidna nhits	85
5.6.2	MOE npe_noavg_corrected	85
5.7	β^+/β^- pulse-shape discrimination	86
5.7.1	Principles of β^+/β^- pulse-shape discrimination in liquid scintillators	86
5.7.2	β^+/β^- time profiles in Borexino	87
5.7.3	Boosted-decision-tree analysis	88
5.8	Radial and energy distributions of external γ -ray background	93
5.9	Fitting procedure	94
5.9.1	Multi-dimensional fitting strategy	95
5.9.2	Fit to the energy spectra	97
5.9.3	Fit to the β^+/β^- pulse-shape parameter.	101
5.9.4	Fit to the reconstructed radial position	102
5.10	Results	103
5.10.1	Fit result	103
5.10.2	Validation of fit method and statistical uncertainties	106
5.10.3	Systematic uncertainties	113
5.10.4	Consistency checks	118
5.10.5	The flux of pep and CNO solar neutrinos	119

5.11 Conclusions and outlook	120
6 Conclusions	123
References	125

Chapter 1

Neutrino oscillations

1.1 Introduction

Neutrinos are neutral leptons with tiny mass [2]. It is a well established experimental fact that the neutrinos (and antineutrinos) are of three types of flavours: electron, ν_e (and $\bar{\nu}_e$), muon, ν_μ (and $\bar{\nu}_\mu$), and tauon ν_τ (and $\bar{\nu}_\tau$). The notion of flavour is dynamical: ν_e is the neutrino which is produced with e^+ , or produces an e^- in charged current weak interaction processes (i.e. neutrinos or antineutrinos emitted in radioactive β decays are ν_e); ν_μ is the neutrino which is produced with μ^+ , or produces μ^- (i.e. neutrinos emitted in charged pion decay $\pi^+ \rightarrow \mu^+ + \nu_\mu$ are ν_μ); ν_τ is the neutrino which is produced with τ^+ , or can produce τ^- when absorbed [2, 3, 4, 5].

There are several neutrino sources in our world, because neutrinos and antineutrinos play a crucial role in many natural or human-made processes. The stars are very important neutrino sources: two distinct nuclear fusion processes, the main pp fusion chain and the sub-dominant CNO cycle power the stars, leading to the production of electron neutrinos with different energy and fluxes. The Sun is a very powerful neutrino source: the flux of *solar neutrinos* at Earth is $\sim 6 \times 10^{10}$ neutrinos $\text{cm}^{-2}\text{s}^{-1}$, and the energy of solar neutrinos is between 0-18 MeV [6]. The result of this PhD thesis is the first experimental detection of the mono-energetic 1.44 MeV solar *pep* neutrinos, which belong to the pp chain, and new limits on CNO solar neutrinos. Therefore, the mechanism of production, propagation, and detection of solar neutrinos will be covered in detail in the following sections.

Neutrinos are also a product of natural radioactivity: nuclear transitions, such as β decay, allow for the changing of the atomic number Z , with no change in the atomic mass A . The basic scheme of such nuclear reactions are:

$$(Z, A) \rightarrow (Z + 1, A) + e^- + \bar{\nu}_e \quad (\beta^- \text{ decay}) \quad (1.1)$$

$$(Z, A) \rightarrow (Z - 1, A) + e^+ + \nu_e \quad (\beta^+ \text{ decay}) \quad (1.2)$$

$$(Z, A) + e^+ \rightarrow (Z - 1, A) + \nu_e \quad (\text{electron capture}) \quad (1.3)$$

where (Z, A) represents a nucleus with atomic number Z and mass number A . Nuclear β decay processes have 3 particles in the final state, so the kinetic energy spectrum of the emitted neutrinos (and therefore of the emitted electrons or positrons) is continuous.

The electron capture process have 2 particles in the final state, therefore the kinetic energy of the neutrino (and of the final state nucleus) in the centre of momentum reference frame is single-lined¹, because of the conservation of energy and momentum. Nuclear β^+ decays and electron capture contribute, within the pp chain and CNO cycle, to power the Sun (Sec. 2.4).

Geo-neutrinos (geo- $\bar{\nu}_e$) are electrons antineutrinos produced in β^- decays of ^{40}K and of several nuclides in the chains of long-lived radioactive isotopes ^{238}U and ^{232}Th , which are naturally present in the Earth [7].

Neutrinos are also continuously created by high energy cosmic rays impeding on the Earth's upper atmosphere. The dominant *atmospheric neutrino* production mechanism comes from pion decay. The interaction of cosmic ray protons with nitrogen nuclei in the atmosphere lead to the production of charged pions, kaons, and other charged mesons: $p + {}^{16}\text{N} \rightarrow \pi^+, K^+, D^+$, etc. A positively charged pion decay most of the times into an antimuon and a muon neutrino ($\pi^+ \rightarrow \nu_\mu + \mu^+$), and the antimuon will decay into an antimuon neutrino, an electron neutrino and a positron ($\mu^+ \rightarrow \bar{\nu}_\mu + e^+ + \nu_e$). The energy range atmospheric neutrinos is $\sim 1 - 100$ GeV [8].

A Supernova explosion, happening when a star at least 8 times more massive than the sun collapses, releases an enormous amount of energy ($\sim 10^{51-53}$ ergs) with a sudden burst neutrinos of ~ 10 second duration. All type of neutrino flavours are emitted in a Supernova event. Supernova neutrinos were detected for the first time (also last time, so far) in 1987 by the Kamiokande detector [9]. The flux of Diffuse Supernova Neutrino Background (DSNB), composed by the neutrinos emitted from all the Supernova bursts in the past, is expected to be several tens per square centimetre per second. However, supernova relic neutrinos have not been detected so far [10].

In operating nuclear reactors, ^{235}U , ^{238}U , ^{239}Pu , and ^{241}Pu undergo fission reaction after absorbing a neutron. The fission products are generally neutron-rich unstable nuclei and perform β decays until they become stable nuclei. One $\bar{\nu}_e$ is produced in each β^- decay. Typical modern commercial light-water reactors have thermal powers of the order of 3 GW_{th}. On average each fission produces ~ 200 MeV and ~ 6 $\bar{\nu}_e$ per second, resulting in 6×10^{20} $\bar{\nu}_e$ production per second [11, 12].

Neutrinos can also be created at accelerator facilities. High-statistics and narrow neutrino beams are produced from the decay of focused high-energy π mesons and the subsequent decay of muons [4].

The experiments with solar, atmospheric, reactor and long-baseline accelerator neutrinos have provided compelling evidences for the existence of neutrino oscillations, *i.e.* transitions in flight between the different flavour neutrinos ν_e, ν_μ, ν_τ (antineutrinos $\bar{\nu}_e, \bar{\nu}_\mu, \bar{\nu}_\tau$), caused by nonzero neutrino masses and neutrino mixing. The current understanding of the neutrino mixing and oscillations is outlined in this chapter.

The chapter is organised as follows. In Section 1.2 I review the role of the neutrino and its interactions in the Standard Model of particle physics. In Section 1.3, the neutrino flavor mixing and neutrino oscillations are introduced. The basic equations for neutrino oscillations in vacuum are derived. Section 1.4 describes the neutrino oscillations in matter. In Section 1.5 I review the phenomenology of neutrino oscillations.

¹ assuming that the kinetic energy in the initial state is negligible

1.2 Neutrinos in the Standard Model of particle physics

Among the three different flavour neutrinos and antineutrinos, no two are identical. To account for this fact, in the framework of quantum mechanics, the states which describe different flavour neutrinos are orthogonal: $\langle \nu_{l'} | \nu_l \rangle = \delta_{l'l}$, $\langle \bar{\nu}_{l'} | \bar{\nu}_l \rangle = \delta_{l'l}$, and $\langle \bar{\nu}_{l'} | \nu_l \rangle = 0$. The flavour of a given neutrino is Lorentz invariant. It is also well known from the existing data (all neutrino experiments were done so far with relativistic neutrinos or antineutrinos), that the flavour neutrinos ν_l (antineutrinos $\bar{\nu}_l$), are always produced in weak interaction processes in a state that is predominantly left-handed (LH) (right-handed (RH)). To account for this fact, ν_l and $\bar{\nu}_l$ are described in the Standard Model (SM) by a chiral LH flavour neutrino field $\nu_{lL}(x)$, $l = e, \mu, \tau$. For massless ν_l , the state of ν_l ($\bar{\nu}_l$) which the field $\nu_{lL}(x)$ annihilates (creates) is with helicity $-1/2$ (helicity $+1/2$). If ν_l has a non-zero mass m , the state of ν_l ($\bar{\nu}_l$) is a linear superposition of the helicity $-1/2$ and $+1/2$ states, but the helicity $+1/2$ state (helicity $-1/2$ state) enters into the superposition with a coefficient $\propto m/E$, E being the neutrino energy, and thus is strongly suppressed. In the framework of the Standard Model of particle physics, the LH flavour neutrino field $\nu_{lL}(x)$, together with the LH charged lepton field $l_L(x)$, forms an $SU(2)_L$ doublet. In the absence of neutrino mixing and zero neutrino masses, $\nu_{lL}(x)$ and $l_L(x)$ can be assigned one unit of the additive lepton charge L_l and the three charges L_l ($l = e, \mu, \tau$) are conserved by the weak interaction (at least at the lowest order in perturbation theory).

In the Standard Model of particle physics, neutrinos interactions are described in the Electroweak Sector. The standard electroweak model is based on the gauge group $SU(2) \times U(1)$, with gauge bosons W_μ^i ($i = 1, 2, 3$, and μ is the four-vector index), and B_μ for the $SU(2)$ and $U(1)$ factors, respectively, and the corresponding gauge coupling constants g and g' . The LH fermion field of the i^{th} fermion flavour family transforms as $SU(2)_L$ doublets $\Psi_i = \begin{pmatrix} \nu_i \\ l_i^- \end{pmatrix}$ and $\begin{pmatrix} u_i \\ d_i' \end{pmatrix}$, where $d_i' \equiv \sum_j V_{ij} d_j$, and V is the Cabibbo-Kobayashi-Maskawa mixing matrix. The RH fields are $SU(2)$ singlets. In the Standard Model there are three fermion families and one single complex Higgs doublet which is introduced for gauge vector bosons and charged leptons mass generation.

After spontaneous symmetry breaking, the ElectroWeak Lagrangian density for the fermion fields ψ_i can be written [2]:

$$\mathcal{L}_F = \sum_i \bar{\psi}_i \left(i\partial - m_i - \frac{gm_i H}{2M_W} \right) \psi_i \quad (1.4)$$

$$- \frac{g}{2\sqrt{2}} \sum_i \bar{\Psi}_i \gamma^\mu (1 - \gamma^5) (T^+ W_\mu^+ + T^- W_\mu^-) \Psi_i \quad (1.5)$$

$$- e \sum_i q_i \bar{\psi}_i \gamma^\mu \psi_i A_\mu \quad (1.6)$$

$$- \frac{g}{2 \cos \theta_W} \sum_i \bar{\psi}_i \gamma^\mu (g_V^i - g_A^i \gamma^5) \psi_i Z_\mu ; \quad (1.7)$$

$\theta_W = \tan^{-1}(g'/g)$ is the electroweak mixing angle; $e = g \sin \theta_W$ is the positron electric charge; $A = B \cos \theta_W + W^3 \sin \theta_W$ is the (massless) photon field; $W^\pm = (W^1 \mp iW^2)/\sqrt{2}$ and $Z = -B \sin \theta_W + W^3 \cos \theta_W$ are the massive charged and neutral weak boson fields

respectively; T^+ and T^- are the weak isospin raising and lowering operators.

The vector and axial-vector couplings are:

$$g_V^i = t_{3L}(i) - 2q_i \sin^2 \theta_W \quad (1.8)$$

$$g_A^i = t_{3L}(i) \quad (1.9)$$

where $t_{3L}(i)$ is the weak isospin of fermion i ($+1/2$ for ν_i and u_i ; $-1/2$ for l_i and d_i), q_i is the charge of the fermion i in units of e .

The terms describing neutrino interactions in the electroweak Lagrangian are the second and the fourth. The second term represents charged-current weak interaction. For example, the coupling of a W boson to an electron e and an electron neutrino ν_e is

$$- \frac{e}{2\sqrt{2}\sin\theta_W} \left[W_\mu^- \bar{e}\gamma^\mu(1 - \gamma^5)\nu_e + W^+ \bar{\nu}_e\gamma^\mu(1 - \gamma^5)e \right]. \quad (1.10)$$

For momenta small compared to M_W , this term gives rise to the effective four-fermion interaction with the Fermi constant given by $G_F\sqrt{2} = g^2/8M_W^2$. The fourth term in the electroweak Lagrangian is the weak neutral-current interaction.

At present there is no evidence for the existence of states of relativistic neutrinos (antineutrinos) which are predominantly right-handed (left-handed), ν_R ($\bar{\nu}_L$). If RH neutrinos and LH antineutrinos exist, their interaction with matter should be much weaker than the weak interaction of the flavour LH neutrinos and RH antineutrinos; for this reason, ν_R ($\bar{\nu}_L$) are often called *sterile* neutrinos (antineutrinos) [13]. In the formalism of the Standard Model, the sterile ν_R and $\bar{\nu}_L$ can be described by $SU(2)_L$ singlet RH neutrino fields. In this case, ν_R and $\bar{\nu}_L$ have no gauge interactions, i.e., do not couple to the weak W^\pm and Z^0 bosons. If present in an extension of the Standard Model, the RH neutrinos can play a crucial role in the generation of neutrino masses and mixing, and in understanding of the remarkable disparity between the magnitudes of neutrino masses and the masses of charged leptons and quarks.

1.3 Neutrino mixing and oscillations

Solar neutrino experiments (Homestake [14], Kamiokande [15], GALLEX-GNO [16, 17, 18], SAGE [19], Super-Kamiokande [20, 21], SNO [22, 23, 24], Borexino [25, 26, 1]), atmospheric neutrino experiments (Super-Kamiokande [27, 28]), reactor neutrino experiments (KamLAND [29, 30, 31], DoubleChooz [32]), and long-baseline accelerator neutrino experiments (K2K [33], MINOS [34, 35, 36], Opera [37], T2K [38]) have provided compelling evidences for the existence of neutrino oscillations, transitions in flight between the different flavour neutrinos ν_e , ν_μ , ν_τ (antineutrinos $\bar{\nu}_e$, $\bar{\nu}_\mu$, $\bar{\nu}_\tau$), caused by nonzero neutrino masses and neutrino mixing [39, 40].

The existence of flavour neutrino oscillations implies that if a neutrino of a given flavour, say ν_e , with energy E is produced in some weak interaction process, at a sufficiently large distance L from the ν_e source the probability to find a neutrino of a different flavour, say ν_μ , $P(\nu_e \rightarrow \nu_\mu; E, L)$, is different from zero. $P(\nu_e \rightarrow \nu_\mu; E, L)$ is called the $\nu_e \rightarrow \nu_\mu$ oscillation or transition probability. If $P(\nu_e \rightarrow \nu_\mu; E, L) \neq 0$, the probability that ν_e will not change into a neutrino of a different flavour, the ν_e

Survival Probability $P(\nu_e \rightarrow \nu_e; E, L)$ will be smaller than one. If only electron neutrinos ν_e are detected in a given experiment, and they take part in oscillations, one would observe a *disappearance* of electron neutrinos on the way from the ν_e source to the detector. As a consequence of the results of the experiments quoted above, the existence of oscillations of the solar ν_e , atmospheric ν_μ and $\bar{\nu}_\mu$, accelerator ν_μ and reactor $\bar{\nu}_e$, driven by nonzero neutrino masses and neutrino mixing, was firmly established. There are strong indications that, under certain conditions, the solar ν_e transitions are affected by the solar matter (Sec. 2.4 and [41, 42]).

Oscillation of neutrinos are a consequence of the presence of flavour neutrino mixing, or lepton mixing. In the framework of a local quantum field theory, used to construct the Standard Model, this means that the LH flavour neutrino fields $\nu_{lL}(x)$ which enter into the expression for the lepton current in the CC weak interaction Lagrangian (1.5), are linear combinations of the fields of three (or more) neutrinos ν_i , having masses $m_i \neq 0$:

$$\nu_{lL}(x) = \sum_i U_{li} \nu_{iL}(x), \quad l = e, \mu, \tau, \quad (1.11)$$

where $\nu_{iL}(x)$ is the LH component of the field of ν_i possessing a mass m_i and U is the *neutrino mixing matrix*. Eq (1.11) implies that the individual lepton charges $L_l, l = e, \mu, \tau$ are not conserved. Thus, the neutrino state created in the decay $W^+ \rightarrow l^+ + \nu_l$ is in the state

$$|\nu_l\rangle = \sum_i U_{li}^* |\nu_i\rangle \quad (1.12)$$

where the sum extend up to all massive neutrino states. This superposition of neutrino mass eigenstates, produced in association with the charged lepton of flavour l , is the state we refer to as the neutrino of flavour l .

All existing compelling data on neutrino oscillation can be described assuming 3 flavour neutrinos and 3 massive neutrino states [2]. In this description, the mixing matrix U is then a 3×3 unitary matrix. Assuming CPT invariance, the unitarity of U guarantees that the only charged lepton a ν_l can create in a CC weak interaction is a l , with the same flavour as the neutrino [39, 40].

The process of neutrino oscillation is quantum mechanical to its core, and it is a consequence of the existence of nonzero neutrino masses and neutrino (lepton) mixing. The complete derivation of the neutrino oscillation probability would require a full wave packet treatment for the evolution of the massive neutrino states [43]. Here is presented a simplified version of this derivation, with no use of wave packet formalism, corresponding to a plane-wave description. This derivation accounts only for the movement of the centre of the wave packet describing ν_i , and is valid only for the propagation of neutrinos in vacuum. A derivation of the neutrino oscillation probability in the matter is given in section 1.4. The amplitude for the oscillation $\nu_\alpha \rightarrow \nu_\beta$, $\text{Amp}(\nu_\alpha \rightarrow \nu_\beta)$, is a coherent sum over the contributions of all the ν_i :

$$\text{Amp}(\nu_\alpha \rightarrow \nu_\beta) = \sum_i U_{\alpha i}^* \text{Prop}(\nu_i) U_{\beta i} \quad (1.13)$$

where $\text{Prop}(\nu_i)$ is the amplitude for a ν_i to propagate from the source to the detector. From elementary quantum mechanics, the propagation amplitude $\text{Prop}(\nu_i)$ is

$\exp[-im_i\tau_i]$, where m_i is the mass of ν_i , and τ_i is the proper time that elapses in the ν_i rest frame during its propagation. By Lorentz invariance, $m_i\tau_i = E_it - p_iL$, where L is the lab-frame distance between the neutrino source and the detector, t is the lab-frame time taken for the beam to traverse this distance, and E_i and p_i are, respectively, the lab-frame energy and momentum of the ν_i component of the neutrino.

In the oscillation probability, only the relative phases of the propagation amplitudes for different mass eigenstates will have physical consequences. The relative phase of $\text{Prop}(\nu_i)$ and $\text{Prop}(\nu_j)$, $\delta\phi_{ij}$, is given by

$$\delta\phi_{ij} = (p_j - p_i)L - (E_i - E_j)t \quad (1.14)$$

To an excellent approximation, $t \simeq L/\bar{v}$, where $\bar{v} = (p_i + p_j)/(E_i + E_j)$ is an approximation to the average of the velocities of the ν_i and ν_j components of the beam. For relativistic neutrinos, which corresponds to the conditions in both past and currently planned future neutrino oscillation experiments [2], $\bar{v} \simeq c$, and $E = \sqrt{p^2 + m^2} \simeq p$ with extremely small deviations proportional to m^2/E . With these approximations, the relative phase of the amplitude for different mass eigenstates becomes

$$\delta\phi_{ij} \simeq (m_j^2 - m_i^2) \frac{L}{2E} \quad (1.15)$$

The phase difference $\delta\phi_{ij}$ is Lorentz-invariant. The amplitude of oscillation $\nu_\alpha \rightarrow \nu_\beta$ for neutrino with energy E , at distance L from the source is:

$$\text{Amp}(\nu_\alpha \rightarrow \nu_\beta) = \sum_i U_{\alpha i}^* e^{-im_i^2 L/2E} U_{\beta i} \quad (1.16)$$

The *oscillation probability* in vacuum is then

$$\begin{aligned} P(\nu_\alpha \rightarrow \nu_\beta; E, L) &= \delta_{\alpha\beta} \\ &- 4 \sum_{i>j} \text{Re}(U_{\alpha i}^* U_{\beta i} U_{\alpha j} U_{\beta j}^*) \sin^2[1.27 \Delta m_{ij}^2 (L/E)] \\ &- 2 \sum_{i>j} \text{Im}(U_{\alpha i}^* U_{\beta i} U_{\alpha j} U_{\beta j}^*) \sin[2.54 \Delta m_{ij}^2 (L/E)] \quad (1.17) \end{aligned}$$

Here, $\Delta m_{ij}^2 = m_i^2 - m_j^2$ is in eV^2 , L is in km, and E is in GeV, and the identity

$$\Delta m_{ij}^2 (L/4E) \simeq 1.27 \Delta m_{ij}^2 (\text{eV}^2) \frac{L(\text{km})}{E(\text{GeV})} \quad (1.18)$$

has been used. This expression is valid if neutrino propagation happens in vacuum. If the neutrino propagates in matter, the coherent scattering on electrons can lead to regeneration effects, and modify the expression for the oscillation probability [41, 42]. Matter effects in neutrino oscillation are described in Sec. 1.4 and Sec. 2.5.

It follows from Eq. (1.17) that in order for neutrino oscillation to occur, at least two massive neutrinos states ν_i should have different mass, and lepton mixing should take place. The neutrino oscillation effects are relevant if

$$\frac{|\Delta m_{ij}^2| L}{2E} \geq 1 \quad (1.19)$$

One can relate the oscillation probabilities for neutrinos and antineutrinos, assuming that CPT invariance holds:

$$P(\bar{\nu}_\alpha \rightarrow \bar{\nu}_\beta) = P(\nu_\beta \rightarrow \nu_\alpha) \quad . \quad (1.20)$$

But, from Eq. (1.17) we see that

$$P(\nu_\beta \rightarrow \nu_\alpha; U) = P(\nu_\alpha \rightarrow \nu_\beta; U^*) \quad . \quad (1.21)$$

Thus, when CPT invariance holds,

$$P(\bar{\nu}_\alpha \rightarrow \bar{\nu}_\beta; U) = P(\nu_\alpha \rightarrow \nu_\beta; U^*) \quad (1.22)$$

That is, in vacuum, the probability for oscillation of an antineutrino is the same as for a neutrino, except that the mixing matrix U is replaced by its complex conjugate. Thus, if U is not real, and if all the terms in U are different from zero, the neutrino and antineutrino oscillation probabilities can differ by having opposite values of the last term in Eq (1.17), and this imply a violation of CP invariance. However, even if CP invariance holds in neutrino mixing, neutrino and antineutrino oscillation probabilities can be different when the propagation occurs in matter, because of the different coherent scattering amplitudes for neutrinos and antineutrinos in the matter (see Sec. 1.4 and Sec. 2.5).

The data of neutrino oscillations experiments can be often analysed assuming 2-neutrino mixing (see Sec. 1.5 for the phenomenology behind this approximation):

$$|\nu_l\rangle = \cos\theta|\nu_1\rangle + \sin\theta|\nu_2\rangle, \quad |\nu_x\rangle = -\sin\theta|\nu_1\rangle + \cos\theta|\nu_2\rangle, \quad (1.23)$$

where θ is the neutrino mixing angle in vacuum, and ν_x is another flavour neutrino, $x = l' \neq l$. In this case, the oscillation probability equations become [44]:

$$P^{2\nu}(\nu_l \rightarrow \nu_l) = 1 - \sin^2 2\theta \sin^2 \left(\frac{\Delta m^2 L}{4E} \right) \quad (1.24)$$

$$P^{2\nu}(\nu_l \rightarrow \nu_{l'}) = 1 - P^{2\nu}(\nu_l \rightarrow \nu_l) \quad (1.25)$$

The survival probability depends on two factors: on $\sin^2 \left(\frac{\Delta m^2 L}{4E} \right)$, which exhibits oscillatory dependence on the distance L and on the neutrino energy E (hence the name *neutrino oscillations*), and on $\sin^2 2\theta$, which determines the amplitude of the oscillations. In order to observe the neutrino oscillations, two conditions have to be fulfilled: the mixing angle should be different from zero, large enough to allow the detection of the disappearance or appearance of neutrinos, and $\Delta m^2 L \gtrsim 2E$, otherwise the oscillations do not have enough space to develop on the way to the neutrino detector.

If the dimensions of the neutrino source or the size of the detector are not negligible in comparison with the oscillation length, or the energy resolution of the detector is not high enough, the oscillating term will be averaged out, leading to a flat, energy independent survival probability:

$$P^{2\nu}(\nu_l \rightarrow \nu_l) = 1 - \frac{1}{2} \sin^2 2\theta. \quad (1.26)$$

This approximation holds for sub MeV solar neutrinos, such as solar pp ν s. For solar neutrinos with energy above 1 MeV, such as pep ν s and ^8B ν s, matter effects are relevant, leading again to an energy dependent neutrino survival probability (see Sec. 2.5).

1.4 Matter effects in neutrino oscillations

The presence of matter can change drastically the pattern of neutrino oscillations: neutrinos can interact with the particles forming the matter. When, for instance, ν_e and ν_μ propagates in matter, they can scatter on electrons (e^-), protons (p) or neutrons (n) present in matter. Accordingly, the Hamiltonian of the neutrino system in matter, $H_m = H_0 + H_{int}$, differs from the Hamiltonian in vacuum H_0 , being H_{int} the interaction Hamiltonian describing the interaction of neutrinos with the particles of matter.

The incoherent elastic and the quasi-elastic scattering have a negligible effect on the solar neutrino propagation in the Sun and on the solar, atmospheric, accelerated and reactor neutrino propagation in the Earth: even in the centre of the Sun, where the matter density is relatively high ($\sim 150 \text{ g/cm}^3$), a ν_e with energy of 1 MeV has a mean free path with respect of the indicated scattering processes of $\sim 10^{10} \text{ km}$. The solar radius is much smaller: $R_\odot = 6.96 \cdot 10^5 \text{ km}$, and almost all the solar neutrinos can escape the Sun easily.

The ν_e and ν_μ coherent elastic scattering on the particles of matter generates non-trivial indices of refraction of the ν_e and ν_μ in matter [41]: $k(\nu_e) \neq 1$, $k(\nu_\mu) \neq 1$, and $k(\nu_e) \neq k(\nu_\mu)$. The indices of refraction for ν_e and ν_μ are different because in the ordinary matter there are no muons or muonic atoms, and the difference $k(\nu_e) - k(\nu_\mu)$ is determined essentially by the difference of the real parts of the forward $\nu_e - e^-$ and $\nu_\mu - e^-$ elastic scattering amplitudes [41]. Due to the flavour symmetry of the neutrino - quark (neutrino - nucleon) neutral current interaction, the forward $\nu_e - p, n$ and $\nu_\mu - p, n$ elastic scattering amplitudes are equal and therefore do not contribute to the difference of interest. The imaginary parts of the forward scattering amplitudes (responsible, in particular, for decoherence effects) are proportional to the corresponding total scattering cross-sections and in the case of interest are negligible in comparison with the real parts. The real parts of the $\nu_{e,\mu} - e^-$ elastic scattering amplitudes can be calculated in the Standard Model. To leading order in the Fermi constant G_F , only the tree-level amplitude with exchange of a W^\pm -boson contributes to the process. One finds the following result for $k(\nu_e) - k(\nu_\mu)$ in the rest frame of the scatters [41, 45]:

$$k(\nu_e) - k(\nu_\mu) = -\frac{1}{E} \sqrt{2} G_F N_e, \quad (1.27)$$

where N_e is the electron number density in matter and E is the energy of the neutrino.

Given $k(\nu_e) - k(\nu_\mu)$, the system of evolution equations describing the $\nu_e \leftrightarrow \nu_\mu$ oscillations in matter reads [41]:

$$i \frac{d}{dt} \begin{pmatrix} A_e(t, t_0) \\ A_\mu(t, t_0) \end{pmatrix} = \begin{pmatrix} -\epsilon(t) & \epsilon' \\ \epsilon' & \epsilon(t) \end{pmatrix} \begin{pmatrix} A_e(t, t_0) \\ A_\mu(t, t_0) \end{pmatrix} \quad (1.28)$$

where $A_{e,\mu}(t, t_0)$ is the amplitude probability to find $\nu_{e,\mu}$ at time t of the evolution of the system if at time t_0 the neutrino ν_e or ν_μ has been produced and

$$\epsilon(t) = \frac{1}{2} \left[\frac{\Delta m^2}{2E} \cos 2\theta - \sqrt{2} G_F N_e(t) \right], \quad \epsilon' = \frac{\Delta m^2}{4E} \sin 2\theta. \quad (1.29)$$

The term $\sqrt{2} G_F N_e(t)$ in $\epsilon(t)$ accounts for the effects of matter on neutrino oscillation. The system of evolution equations describing the oscillations of antineutrinos $\bar{\nu}_e \leftrightarrow \bar{\nu}_\mu$ in

matter has exactly the same form except for the matter term in $\epsilon(t)$ which changes sign. The effect of matter in neutrino oscillations is usually called the Mikheyev, Smirnov, Wolfenstein (or MSW) effect.

Consider first the case of $\nu_e \leftrightarrow \nu_\mu$ oscillations in matter with constant density: $N_e(t) = N_e = \text{const}$. Due to the interaction term H_{int} in H_m , the eigenstates of the Hamiltonian of the neutrino system in vacuum $|\nu_{1,2}\rangle$ are not eigenstates of H_m . The eigenstates $|\nu_{1,2}^m\rangle$ of H_m are related to $|\nu_{e,\mu}\rangle$ by the unitary transformation:

$$|\nu_e\rangle = |\nu_1^m\rangle \cos \theta_m + |\nu_2^m\rangle \sin \theta_m, \quad |\nu_\mu\rangle = -|\nu_1^m\rangle \sin \theta_m + |\nu_2^m\rangle \cos \theta_m. \quad (1.30)$$

Here θ_m is the neutrino mixing angle in matter [41],

$$\sin 2\theta_m = \frac{\tan 2\theta}{\sqrt{(1 - \frac{N_e}{N_e^{res}})^2 + \tan^2 2\theta}}, \quad \cos 2\theta_m = \frac{1 - N_e/N_e^{res}}{\sqrt{(1 - \frac{N_e}{N_e^{res}})^2 + \tan^2 2\theta}}, \quad (1.31)$$

where the quantity

$$N_e^{res} = \frac{\Delta m^2 \cos 2\theta}{2E\sqrt{2}G_F} \simeq 6.65 \cdot 10^6 \frac{\Delta m^2 [\text{eV}^2]}{E [\text{MeV}]} \cos 2\theta \text{cm}^{-3} N_A \quad (1.32)$$

is called (for $\Delta m^2 \cos 2\theta > 0$) *resonance density* [42, 45], N_A being Avogadro's number. The probability of $\nu_e \leftrightarrow \nu_\mu$ transition in matter with $N_e = \text{const}$ has the form [41]

$$P_m^{2\nu}(\nu_e \rightarrow \nu_\mu) = |A_\mu(t)|^2 = \frac{1}{2} \sin^2 2\theta_m \left(1 - \cos 2\pi \frac{L}{L_m}\right) \quad (1.33)$$

where $L_m = 2\pi/(E_2^m - E_1^m)$ is the oscillation length in matter, being the difference of the adiabatic states $|\nu_{1,2}^m\rangle$

$$E_2^m - E_1^m = \frac{\Delta m^2}{2E} \left(\left(1 - \frac{N_e}{N_e^{res}}\right)^2 \cos^2 2\theta + \sin^2 2\theta \right)^{\frac{1}{2}} \quad (1.34)$$

As Eq. 1.31 indicates, the dependence of $\sin^2 2\theta_m$ on N_e has a resonance character [42]. Indeed, if $\Delta m^2 \cos 2\theta > 0$, for any $\sin^2 2\theta \neq 0$ there exists a value of N_e given by N_e^{res} , such that when $N_e = N_e^{res}$ we have $\sin^2 2\theta_m = 1$. This implies that the presence of matter can lead to a strong enhancement of the oscillation probability $P_m^{2\nu}(\nu_e \rightarrow \nu_\mu)$ even when the $\nu_e \leftrightarrow \nu_\mu$ oscillations in vacuum are suppressed due to a small value of $\sin^2 2\theta$. For obvious reasons

$$N_e^{res} = \frac{\Delta m^2 \cos 2\theta}{2E\sqrt{2}G_F} \quad (1.35)$$

is called the *resonance condition* [42, 45], while the energy at which the resonance condition holds, for given N_e and $\Delta m^2 \cos 2\theta$, is referred as the *resonance energy*, E^{res} .

Two limiting cases are $N_e \ll N_e^{res}$ and $N_e \gg N_e^{res}$. If $N_e \ll N_e^{res}$, we have from Eq. 1.31, $\theta_m \simeq \theta$, and neutrinos oscillate practically as in vacuum. In the limit $N_e \gg N_e^{res}$ one finds $\theta_m \simeq \pi/2$ ($\cos 2\theta_m \simeq -1$) and the presence of matter suppresses the $\nu_e \leftrightarrow \nu_\mu$ oscillations. In this case $|\nu_e\rangle \simeq |\nu_2^m\rangle$, $|\nu_\mu\rangle = -|\nu_1^m\rangle$, ν_e piratically coincides with the heavier matter eigenstates, while ν_μ coincides with the lighter one.

Since the neutral current weak interaction of neutrinos in the Standard Model is flavour symmetric, the formulae and results obtained in this session are valid for the case of $\nu_e - \nu_\tau$ mixing and $\nu_e \leftrightarrow \nu_\tau$ oscillation in matter as well. The case of $\nu_\mu - \nu_\tau$ mixing, however, is different: to a relatively good precision $k(\nu_\mu) \simeq k(\nu_\tau)$ and the $\nu_\mu \leftrightarrow \nu_\tau$ oscillations in the matter of the Sun and the Earth proceed piratically as in vacuum.

The analogs equations for the oscillation of antineutrinos, $\bar{\nu}_e \leftrightarrow \bar{\nu}_\mu$, in matter can formally be obtained by replacing N_e with $(-N_e)$. Depending on the sign of $\Delta m^2 \cos 2\theta$, the presence of matter can lead to resonance enhancement either of the $\nu_e \leftrightarrow \nu_\mu$ or of the $\bar{\nu}_e \leftrightarrow \bar{\nu}_\mu$ oscillations, but not of both type of oscillations. This disparity between the behaviour of neutrinos and that of antineutrinos is a consequence of the fact that the ordinary matter in the Sun or in the Earth is not charge-symmetric (it contains e^- , p , n , but does not contain their antiparticles) and therefore the oscillations in matter are neither CP nor CPT invariant [46]. Thus, even in the case of 2 neutrino mixing and oscillations, $P_m^{2\nu}(\nu_e \rightarrow \nu_{\mu(\tau)}) \neq P_m^{2\nu}(\bar{\nu}_e \rightarrow \bar{\nu}_{\mu(\tau)})$.

The high energy solar neutrino (ν_e) data evidences that $\Delta m^2 \cos 2\theta > 0$ in the solar sector of neutrino oscillation. In particular, the observed deficit of solar ν_e with energy $> \text{few MeV}$ can only be explained with the MSW enhancement happening in the propagation of the neutrinos from the centre to the surface of the Sun (see Sec. (2.5)). The solar 1.44 MeV *pep* ν s, whose first time experimental detection is the subject of this thesis, have an ideal energy to probe the MSW effect in the energy region between the vacuum dominated and matter enhanced regime of oscillation.

1.5 Phenomenology of neutrino oscillations

All existing neutrino oscillation data² can be described assuming 3-flavour neutrino mixing. The data on the invisible decay width of the Z^0 boson is compatible with only 3 light flavour neutrinos coupled to Z^0 [49, 2]. It follows from the existing data that at least 3 of the neutrinos ν_j must be light and must have different masses.

The neutrino oscillation probabilities depends on $\Delta m_{ij}^2 = (m_i^2 - m_j^2)$ and on the mixing matrix U . On the other hand, a given experiment searching for neutrino oscillation is characterised by the average energy of the neutrinos being studied, \bar{E} , and by the source-detector distance L . The requirement in Eq. (1.19) determines the minimal value of a generic neutrino mass squared difference to which the experiment is sensitive. Because of the interference nature of neutrino oscillations, oscillation experiments can probe, in general, rather small values of Δm^2 . Values of $\min(\Delta m^2)$ characterising qualitatively the sensitivity of different experiments are given in Table 1.1.

In the case of 3-neutrino mixing, there are only two independent neutrino masses squared differences, say Δm_{21}^2 and Δm_{31}^2 . The numbering of massive neutrinos ν_i is conventional. It follows from neutrino oscillation experiments that one of the two independent neutrino mass squared differences is much smaller in absolute value than the second one. In particular, the neutrino mass squared difference observed in the oscillation atmospheric ν_μ and $\bar{\nu}_\mu$, often called Δm_{atm}^2 , is much larger in absolute value than

²except for the LSND result [47], that has not been confirmed by MiniBOONE [48]

Source	Type of ν	\bar{E} [MeV]	L [km]	$\min(\Delta m^2)[\text{eV}^2]$
Sun	ν_e	~ 1	$1.5 \cdot 10^8$	$\sim 10^{11}$
Reactor	$\bar{\nu}_e$	~ 1	~ 100	$\sim 10^{-5}$
Reactor	$\bar{\nu}_e$	~ 1	~ 1	$\sim 10^{-3}$
Atmospheric	$\nu_\mu, \bar{\nu}_\mu, \nu_e, \bar{\nu}_e$	$\sim 10^3$	$\sim 10^4$	$\sim 10^{-4}$
Accelerator	$\nu_\mu, \bar{\nu}_\mu$	$\sim 10^3$	$\sim 10^3$	$\sim 10^{-3}$

Table 1.1: Features and Δm^2 sensitivity of different neutrino oscillation experiments.

the neutrino mass squared difference responsible for the solar ν_e and reactor $\bar{\nu}_e$ oscillation, often called Δm_{sun}^2 . It proves convenient, from the point of view of relating the mixing angles to observables, to identify $|\Delta m_{21}^2|$ with the smaller of the two neutrino masses squared differences, $|\Delta m_{sun}^2|$. Then the larger neutrino mass squared difference $|\Delta m_{31}^2|$ or $|\Delta m_{32}^2|$ can be identified with $|\Delta m_{atm}^2|$. The convention widely used, is to number the massive neutrinos in such a way that $m_1 < m_2$, so that Δm_{21}^2 is not negative. With these choices made, there are two possibilities: either $m_1 < m_2 < m_3$, or $m_3 < m_1 < m_2$. The former possibility is conventionally called *direct hierarchy*, and the latter is called *inverse hierarchy*. The sign of Δm_{atm}^2 (Δm_{31}^2) and the type of hierarchy in neutrino mass spectrum is still unknown at this time. Using these conventions, the measured values of the neutrino mass square differences are [2]:

$$\Delta m_{21}^2 \simeq 7.6 \cdot 10^{-5} \text{eV}^2, \quad |\Delta m_{31}^2| \simeq 2.4 \cdot 10^{-3} \text{eV}^2, \quad \Delta m_{21}^2/|\Delta m_{31}^2| \simeq 0.032 \quad (1.36)$$

The effects of Δm_{31}^2 or Δm_{32}^2 in the oscillation of solar ν_e , and of Δm_{21}^2 in the oscillation of atmospheric ν_μ and $\bar{\nu}_\mu$, and of accelerator ν_μ , are relatively small and sub-dominant. This is due to the fact that $|\Delta m_{21}^2| \ll |\Delta m_{31}^2|$, and in the differences in L , \bar{E} and L/\bar{E} (as well in the production and propagation of neutrinos) in the solar, atmospheric and accelerator experiments.

This fact can be obtained from Eq. (1.17), using the information that one neutrino mass squared difference is much smaller in absolute value than the other mass squared difference. Keeping only the dominant Δm^2 term, in Eq. (1.17), it is possible to treat the neutrino mixing and oscillation as an effective 2-state phenomenon. The neutrino mixing and oscillation probabilities in the 2-neutrino mixing are given in Eq. (1.23, 1.24, 1.25).

Most of the solar ν_e , reactor $\bar{\nu}_e$, atmospheric and long baseline accelerator ν_μ and $\bar{\nu}_\mu$ experiments can be described in the 2-neutrino formalism. The mixing angle that is responsible for solar ν_e (and long baseline reactor $\bar{\nu}_e$) oscillation is called *solar* mixing angle θ_{sun} . The mixing angle responsible for atmospheric and long baseline ν_μ and $\bar{\nu}_\mu$ oscillation is called *atmospheric* mixing angle θ_{atm} .

The neutrino mixing matrix U can be parametrised by 3 angles and 1 CP violation phase³. In order to relate the parameters to the physical observable, it is convenient to parametrise U in such a way that the 2-neutrino mixing angle θ_{sun} and θ_{atm} can be

³ In general, a $n \times n$ unitary matrix can be parametrised by $n(n-1)/2$ angles and $n(n+1)/2$ phases. Because of the invariance of the content of a quantum field theory under a reparametrization of the fields, the number of physical phases is less than the total number of phases. If the massive neutrinos

identified as 2 of the 3 mixing angles. The usual parametrisation of the neutrino mixing matrix U is:

$$U = \begin{bmatrix} c_{12}c_{13} & s_{12}c_{13} & s_{13}e^{-i\delta} \\ -s_{12}c_{23} - c_{12}s_{23}s_{13}e^{i\delta} & c_{12}c_{23} - s_{12}s_{23}s_{13}e^{i\delta} & s_{23}c_{13} \\ s_{12}s_{23} - c_{12}c_{23}s_{13}e^{i\delta} & -c_{12}s_{23} - s_{12}c_{23}s_{13}e^{i\delta} & c_{23}c_{13} \end{bmatrix} \quad (1.37)$$

where $c_{ij} = \cos \theta_{ij}$, $s_{ij} = \sin \theta_{ij}$, the angles $\theta_{ij} = [0, \pi/2]$, $\delta = [0, 2\pi]$ is the Dirac CP violation phase.

Short baseline reactor $\bar{\nu}_e$ experiments (Palo Verde [50], CHOOZ [51], Double Chooz [32]), and long baseline accelerator ν_μ experiments (T2K [38], MINOS [36]), have shown that $|U_{e3}|^2 = |\sin \theta_{13}|^2 \ll 1$. Because of this, one can identify θ_{12} as θ_{sun} and θ_{23} as θ_{atm} . The solar neutrino data have shown that $\Delta m_{21}^2 \cos 2\theta_{12} > 0$ (Sec. 2.4). In the convention employed, this means that $\cos 2\theta_{12} > 0$.

Supposing that in a given experiment $|\Delta m_{31}^2 L / (2E)| \geq 1$, and $\Delta m_{21}^2 L / (2E) \ll 1$. This is the case for the oscillations of reactor $\bar{\nu}_e$ on a distance $L \sim 1$ km (CHOOZ, Double Chooz, Daya Bay [52], Reno [53] experiments), for the oscillation of the accelerator ν_μ with distance $L \sim 10^3$ km (K2K, T2K, MINOS, OPERA experiments). Under this conditions, keeping only the oscillating terms involving Δm_{31}^2 , the oscillation probability in Eq. (1.17) becomes:

$$P(\nu_\alpha \rightarrow \nu_\beta) \simeq P(\bar{\nu}_\alpha \rightarrow \bar{\nu}_\beta) \simeq \delta_{\alpha\beta} - 2|U_{\alpha 3}|^2 (\delta_{\alpha\beta} - |U_{\beta 3}|^2) \left(1 - \cos \frac{\Delta m_{31}^2 L}{2E}\right) \quad (1.38)$$

The survival probability for oscillation of reactor $\bar{\nu}_e$ on a distance $L \sim 1$ km, is given by Eq. 1.38 choosing $\alpha = \beta = e$:

$$P(\bar{\nu}_e \rightarrow \bar{\nu}_e) = P(\nu_e \rightarrow \nu_e) \simeq 1 - 2|U_{e3}|^2 (1 - |U_{e3}|^2) \left(1 - \cos \frac{\Delta m_{31}^2 L}{2E}\right) \quad (1.39)$$

The probability for oscillation of accelerator ν_μ into ν_e (or vice-versa) is given Eq. 1.38 choosing $\alpha = \mu$, $\beta = e$:

$$P(\nu_\mu \rightarrow \nu_e) \simeq 2|U_{\mu 3}|^2 |U_{e3}|^2 \left(1 - \cos \frac{\Delta m_{31}^2 L}{2E}\right) \quad (1.40)$$

$$= \frac{|U_{\mu 3}|^2}{1 - |U_{e3}|^2} P^{2\nu}(|U_{e3}|^2, m_{31}^2) \quad (1.41)$$

Here $P^{2\nu}(|U_{e3}|^2, m_{31}^2)$ is the probability of the 2 neutrino transition $\nu_e \rightarrow (s_{23}\nu_\mu + c_{23}\nu_\tau)$ due to Δm_{31}^2 and a mixing with angle θ_{13} , where,

$$\sin^2 \theta_{13} = |U_{e3}|^2, \quad s_{23}^2 = \sin^2 \theta_{23} \equiv \frac{|U_{\mu 3}|^2}{1 - |U_{e3}|^2}, \quad c_{23}^2 \equiv \cos^2 \theta_{23} = \frac{|U_{\tau 3}|^2}{1 - |U_{e3}|^2} \quad (1.42)$$

are Dirac particles, only $(n-1)(n-2)/2$ phases are physical and can be responsible for CP violation in the lepton sector. In the case the massive neutrinos ν_i are Majorana particles, i.e. particles that coincide with his own antiparticles, 2 additional physical CP violation phases, called Majorana phases, are present in U . However, Majorana phases have no effects in the neutrino oscillation phenomena and will not mentioned further.

In certain cases the dimensions of the neutrino source, ΔL , are not negligible in comparison with the oscillation length. Similarly, when analysing neutrino oscillation data one has to include the energy resolution of the detector, ΔE , in the analysis. As can be shown [54], if $\Delta L \gg E/\Delta m^2$, and/or $L\Delta m^2\Delta E/E^2 \gg 1$, the oscillating terms in the neutrino oscillation probabilities will be averaged out. This is the case for Solar neutrino oscillations in vacuum. In this case (as well as in the case of sufficiently large separation of the ν_i and ν_j neutrino wave packets at the detection point) the interference terms in the oscillation probability (or survival probability) will be negligibly small and the neutrino flavour conversion will be determined by the average probabilities:

$$P(\nu_\alpha \rightarrow \nu_\beta) \simeq \sum_i |U_{\beta i}|^2 |U_{\alpha i}|^2. \quad (1.43)$$

This is the 3-neutrino mixing analog of Eq. 1.26.

Suppose next that in the case of 3-neutrino mixing, $\Delta m_{21}^2 L/2E \sim 1$, while at the same time $|\Delta m_{31(32)}|^2 L/2E \gg 1$ and the oscillations due to Δm_{31}^2 and Δm_{32}^2 are averaged out due to integration over the region of neutrino production, the energy resolution function, etc. This is the case for the oscillations of reactor $\bar{\nu}_e$ observed by the KamLAND experiment [31]. In this case we get for the ν_e and $\bar{\nu}_e$ survival probabilities:

$$P(\bar{\nu}_e \rightarrow \bar{\nu}_e) \simeq |U_{e3}|^4 + (1 - |U_{e3}|^2)^2 P^{2\nu}(\bar{\nu}_e \rightarrow \bar{\nu}_e), \quad (1.44)$$

$$P^{2\nu}(\bar{\nu}_e \rightarrow \bar{\nu}_e) = P^{2\nu}(\nu_e \rightarrow \nu_e) = 1 - \sin^2 2\theta_{12} \sin^2 \left(\frac{\Delta m^2 L}{4E} \right) \quad (1.45)$$

being the ν_e and $\bar{\nu}_e$ survival probability in the case of 2-neutrino oscillation driven by the angle θ_{12} and Δm_{21}^2 , with θ_{12} determined by

$$\cos^2 \theta_{12} = \frac{|U_{e1}|^2}{1 - |U_{e3}|^2}, \quad \sin^2 \theta_{12} = \frac{|U_{e2}|^2}{1 - |U_{e3}|^2}. \quad (1.46)$$

The existing neutrino oscillation data allow us to determine the parameters which drive the solar neutrino and the dominant atmospheric neutrino oscillations with a relatively good precision, and to obtain rather stringent limits on the mixing angle θ_{13} . A comprehensive review on the solar, atmospheric, reactor, and accelerator neutrino oscillation experiments and their impact on the determination of θ_{12} , θ_{23} , θ_{13} , Δm_{21}^2 , and Δm_{31}^2 can be found on [2]. The relevant solar neutrino measurements and their impact on the determination of θ_{12} and Δm_{21}^2 are discussed extensively in Sec. 2.

1.6 Conclusions and outlook

After the spectacular experimental progress made in the studies of neutrino oscillations, further understanding of the pattern of neutrino masses and neutrino mixing, of their origins and the status of the CP symmetry in the lepton sector requires an extensive and challenging program of research. One of the targets of such a research program include the high precision measurement of the oscillation parameters that drive the solar neutrino oscillations and test the MSW effect with neutrinos of different energies. Solar neutrinos are sensitive probe for pursuing this program.

Chapter 2

Solar neutrino observations

2.1 Introduction

Both the first evidence and the first discoveries of neutrino flavor transformation have come from experiments which detected neutrinos from the Sun [55, 22, 23]. This discovery was remarkable, not only because it was unexpected, but because it was made initially by experiments designed to different physics. Ray Davis's solar neutrino experiment [56] was created to study astrophysics, not the particle physics of neutrinos.

Observation of solar neutrinos directly addresses the theory of stellar structure and evolution, which is the basis of the standard solar models (SSMs). Neutrinos are indeed the only particles which can travel undisturbed from the solar core to us, providing details about the inner workings of the Sun. The Sun as a well-defined neutrino source also provides extremely important opportunities to investigate nontrivial neutrino properties such as nonzero mass, flavor mixing, neutrino oscillations, and MSW effect because of the wide range of matter density and the great distance from the Sun to the Earth. The solar neutrino flux is energetically broadband, free of flavor backgrounds, and passes through quantities of matter obviously unavailable to terrestrial experiments.

The chapter is organised as follows. In Section 2.2 I describe the Solar Standard Model. In Section 2.3, the solar metallicity problem is presented. Section 2.4 reports on the pp fusion chain and the CNO cycle which fuel the Sun and produce solar neutrinos. In Section 2.5 I describe the propagation of solar neutrinos in the Sun, with emphasis on the MSW effect. In Section 2.6 I review the experiments which have detected solar neutrinos, describing the detection method and their result. The discovery of solar neutrino oscillations, as well with the current understanding of the MSW-LMA oscillation scenario is discussed in Section 2.7.

2.2 The Standard Solar Model

The stars are powered by nuclear fusion reactions. Two distinct processes, the main pp fusion chain and the sub-dominant CNO cycle, are expected to fuel the Sun and produce solar neutrinos with different energy spectra and fluxes (see Sec. 2.4 and [6]).

The combined effect of these reactions is written as

$$4p \rightarrow {}^4\text{He} + 2e^+ + 2\nu_e . \quad (2.1)$$

Positrons annihilate with electrons. The overall reaction releases about 26.7 MeV into kinetic energy of the final particles, including neutrinos [6]. Each conversion of four proton into an ${}^4\text{He}$ nucleus is known as a *termination* of the chain of energy generating reactions that accomplishes the nuclear fusion. The thermal energy that is supplied by nuclear fusion ultimately emerges from the surface of the Sun as sunlight. Energy is transported in the deep solar interior mainly by photons, which means that the opacity of matter to radiation is important. The pressure that supports the Sun is provided largely by the thermal motions of the electrons and ions. Some of the principal assumptions used in constructing standard solar models are [6]:

- Hydrostatic equilibrium: the Sun is assumed to be in hydrostatic equilibrium, that is, the radiative and particle pressures of the model exactly balances gravity. Observationally, this is known to be an excellent approximation since a gross departure from hydrostatic equilibrium would cause the Sun to collapse (or expand) in a free-fall time of less than a hour.
- Energy transport by photons or by convective motions: in the deep interior, where neutrinos are produced, the energy transport is primarily by photon diffusion; the calculated radiative opacity is a crucial ingredient in the construction of a model and has been the subject of a number detailed studies.
- Energy generation by nuclear reactions: the primary energy source for radiated photons and neutrinos is nuclear fusion, although the small effects of gravitational contraction (or expansion) are also included.
- Abundance changes caused only by nuclear reactions: the initial solar interior is presumed to have been chemically homogeneous. In regions of the model that are stable to matter convection, changes in the local abundances of individual isotope occur only by nuclear reactions.

A *Standard Solar Model* is the end product of a sequence of models. The calculation of a model begins with the description of a main sequence star that has a homogeneous composition. Hydrogen burns in the stellar core, supplying both the radiated luminosity and the thermal pressure that supports the star against the gravity. Successive models are calculated by allowing for composition changes caused by nuclear reactions, as well as the mild evolution of other parameters, such as the surface luminosity and the temperature distribution inside the star. The models that describe later times in an evolutionary sequence have inhomogeneous compositions.

A satisfactory solar model is a solution of the evolutionary equation that satisfies boundary conditions in both space and time. Solar astrophysicists seek models with a fixed mass M_\odot , with a total luminosity L_\odot , and with an outer radius R_\odot at an elapsed time of $4.6 \cdot 10^9$ years (the present age of the Sun, determined accurately from meteoritic ages). The assumed initial values of chemical composition and entropy are iterated until an accurate description is obtained of the Sun. The solution of the evolution equations

determines the initial values for the mass fractions of hydrogen, helium, and heavy elements, the present distribution of physical variables inside the Sun, the spectrum of acoustic oscillation frequencies observed on the surface of the Sun, and the neutrino fluxes [6].

The most elaborate SSM calculations have been developed by Bahcall and his collaborators¹, who define their SSM as the solar model which is constructed with the best available physics and input data. Therefore, their SSM calculations have been rather frequently updated. SSM's labelled as BS05(OP) [57], BSB06(GS) and BSB06(AGS) [58], BPS08(GS) and BPS08(AGS) [59], and BPS11(GS) and BPS11(AGSS) [60] represent recent model calculations.

Here, OP means that newly calculated radiative opacities from the Opacity Project are used. The later models are also calculated with OP opacities. GS and AGS refer to old and new determinations of solar abundances of heavy elements. There are significant differences between the old, higher heavy element abundances (henceforth GS, [61]) and the new, lower heavy element abundances (henceforth AGS, [62] and AGSS, [63]). The models with GS are consistent with helioseismological data, but the models with AGS and AGSS are not [64]. The measurement of the flux of the neutrinos resulting from the CNO cycle may help to resolve this *Solar Metallicity Problem*.

2.3 The Solar Metallicity Problem

The solar heavy-element abundance², Z , is one of the important inputs in solar model calculations. The heavy-element abundance affects solar structure by affecting radiative opacities [6]. The abundance of oxygen, carbon, and nitrogen also affect the energy generation rates through the CNO cycle (see Sec. 2.4 and [6]). The effect of Z on opacities changes the boundary between the radioactive and convective zones, as well as the structure of radiative region; the effect of Z on energy generation rates can change the structure of the core [64]. Solar Z is not only important in modelling the Sun, it is also important for other fields of astrophysics. The heavy-element abundance of the Sun is usually used as a reference in studies of the metallicity of stars, the chemical evolution of galaxies; thus, an accurate knowledge of solar metallicity is important.

Till the early part of last decade, the solar abundance compilation of Grevesse and Sauval (GS98, [61]), with the ratio between heavy-element and hydrogen abundance $Z/X = 0.023$, was used. In a series of papers Allende-Prieto [65, 66] and Asplund and others [67, 68] have revised the spectroscopic determinations of the solar photospheric composition using sophisticated 3D stellar atmospheric models. These models were obtained by 3D radiation-hydrodynamic simulations of the near-surface layers of the Sun. Their results indicated that the solar carbon, nitrogen, and oxygen abundances are lower by about 35% to 45% than those listed by GS98. The revision of the oxygen abundance led to a comparable change in the abundances of neon and argon too, since these abundances are generally measured through the abundance ratio for Ne/O and Ar/O. Additionally, Asplund [69] also determined a lower value (by about 10%) for

¹ Bahcall passed away in 2005, but his program to improve SSM is still pursued by his collaborators

² in astrophysics, any element with atomic number greater than helium is labelled as heavy-element, or metal

the photospheric abundance of silicon compared with the GS98 value. As a result, all the elements for which abundances are obtained from meteoritic measurements have seen their abundances reduced by a similar amount. These measurement have been summarised by Asplund, Grevesse and Sauval (AGS05, [62]). The net result of these changes is that Z/X for the Sun is reduced to 0.0165 (or $Z = 0.0122$) in AGS05, about 28% lower than the previous value of GS98 $Z/X \sim 0.023$. The most recent and complete revision by Asplund et al. (AGSS09, [63]) also shows a reduction in the abundances of the volatile CNO elements and Ne with respect to the older compilation of solar abundances of GS98.

The consequence of this reduction of the solar Z/X is that the structure of the solar models do not agree well with the helioseismically determined structure of the Sun any more [64]. In particular, the relative sound-speed and density in solar models with the AGS05 abundances disagrees with the experimental data a lot more than models with GS98 abundances. The main reason for the disagreement is the difference in the position of the convection zone (CZ) base between the model and the Sun. The AGS05 model has its CZ base at $0.729R_{\odot}$, in contrast the CZ base of the Sun is at $0.713 \pm 0.001R_{\odot}$ [64]. Additionally, solar models with AGS05 abundances have lower helium abundances (Y) than the Sun, $Y = 0.230$ rather than the helioseismically determined solar helium abundance of $Y = 0.2485 \pm 0.0034$ [64]. The GS98 solar model by contrast has CZ base at $0.715R_{\odot}$ and helium abundance of $Y = 0.243$, much closer to the real solar values.

A competitive source of information about the solar core that may solve the Solar Metallicity Problem are the neutrino emitted in the CNO cycle. SSMs with high heavy-element abundance, such as BPS08(GS) [59], predict a total CNO neutrino flux of $(5.4 \pm 0.8) \times 10^8 \text{ cm}^{-2} \text{ s}^{-1}$, while SSMs with low heavy-element abundance, such as AGSS09, predict a 30% lower CNO flux of $(3.8_{-0.5}^{+0.6}) \times 10^8 \text{ cm}^{-2} \text{ s}^{-1}$ [60]. One of the result of this PhD thesis is the strongest constrain on the CNO neutrino flux up to date, which leads to the strongest test of the solar metallicity up to date (see Sec. 5.10).

2.4 Production of solar neutrinos

The solar neutrinos are produced by some of the fusion reactions in the pp chain or the CNO cycle [6]. In both processes, the net effect is the fusion of four protons in a ${}^4\text{He}$ nucleus. About 600 million tons of hydrogen are burned every second to supply the solar luminosity. The main nuclear burning mechanism in the Sun is the proton-proton chain (or pp chain). A sub dominant and still undetected process for the energy generation in the Sun is the Carbon-Nitrogen-Oxygen cycle (or CNO cycle), in which the fusion of four protons into a ${}^4\text{He}$ nucleus is achieved through reactions involving carbon, nitrogen and oxygen. The CNO cycle is supposed to be a dominant process for massive stars ($> 1.5, M_{\odot}$), in which the heavy-element abundance is high. The SSM prediction for the fluxes from neutrino-producing reactions is given in Table 2.4. Fig. 2.1 shows the solar neutrino spectra calculated with the BS05(OP) model which is similar to the BPS08(GS) model.

In the following subsections, the reactions of pp chain and CNO cycle, as well with the neutrinos created in such processes, are described in detail.

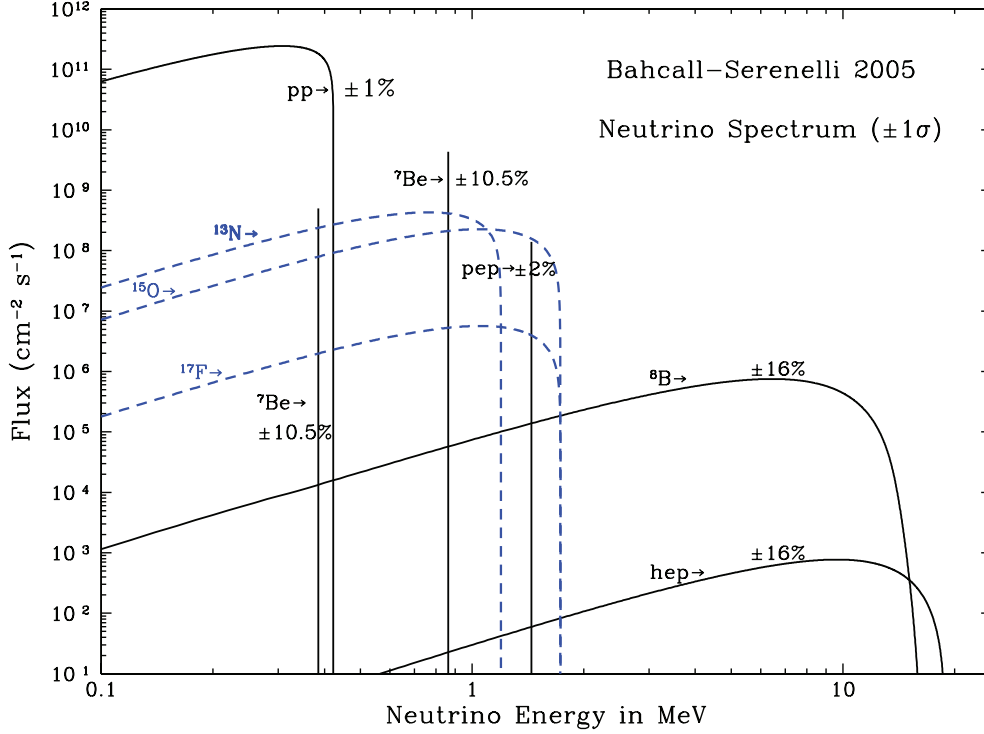


Figure 2.1: The solar neutrino spectrum predicted by the BS05(OP) standard solar model [57]. The neutrino fluxes are given in units of $\text{cm}^{-2}\text{s}^{-1}\text{MeV}^{-1}$ for continuous spectra and $\text{cm}^{-2}\text{s}^{-1}$ for line spectra. The numbers associated with the neutrino sources show theoretical errors of the fluxes.

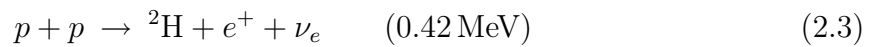
2.4.1 The pp chain

The pp chain has three branches, named pp - I, pp - II and pp - III. The net process in each termination of the pp chain is:



with Q-value³ $Q=24.7$ MeV. In some cases, the process is $4p + e^- \rightarrow {}^4\text{He} + e^+ + 2\nu_e$. The positrons annihilate with free electrons in the solar plasma (with γ -rays with total energy of $2m_e c^2 = 1.02$ MeV emitted for each annihilation). The total energy gain in each termination of the pp chain is ~ 26.7 MeV, on which, on average, only a small amount is carried away by neutrinos. The energy of the neutrinos emitted in the pp chain depends on its particular termination.

The first step of each branch is one of this weak interaction processes (the energy available to the final states body, the Q-value, is written in brackets):



³the Q-value is defined as the difference between the initial state total mass and final state total mass, and it is equal, in natural units, to the total kinetic energy available to the final state particles

Reaction	Abbr.	Energy (MeV)	GS98 Flux	AGSS09 Flux	exp
$pp \rightarrow {}^2\text{H} e^+ \nu$	pp	0 - 0.42	5.98 (1 ± 0.006)	6.03 (1 ± 0.006)	10^{10}
$pe^- p \rightarrow {}^2\text{H} \nu$	pep	1.44	1.44 (1 ± 0.012)	1.47 (1 ± 0.012)	10^8
${}^3\text{He} p \rightarrow {}^4\text{He} e^+ \nu$	hep	0 - 19.79	8.04 (1 ± 0.30)	8.31 (1 ± 0.30)	10^3
${}^7\text{Be} e^- \rightarrow {}^7\text{Li} \nu$	${}^7\text{Be}$	0.862 (0.383)	5.00 (1 ± 0.07)	4.56 (1 ± 0.07)	10^9
${}^8\text{B} \rightarrow {}^8\text{Be} e^+ \nu$	${}^8\text{B}$	0 - 17.98	5.58 (1 ± 0.14)	4.59 (1 ± 0.14)	10^6
${}^{13}\text{N} \rightarrow {}^{13}\text{C} e^+ \nu$	${}^{13}\text{N}$	0 - 1.19	2.96 (1 ± 0.14)	2.17 (1 ± 0.14)	10^8
${}^{15}\text{O} \rightarrow {}^{15}\text{C} e^+ \nu$	${}^{15}\text{O}$	0 - 1.73	2.23 (1 ± 0.15)	1.56 (1 ± 0.15)	10^8
${}^{17}\text{F} \rightarrow {}^{17}\text{C} e^+ \nu$	${}^{17}\text{F}$	0 - 1.74	5.52 (1 ± 0.17)	3.40 (1 ± 0.16)	10^6
CNO cycle	CNO	0 - 1.74	5.24 (1 ± 0.84)	3.76 (1 ± 0.60)	10^8

Table 2.1: Neutrino-producing reactions in the Sun (first column), their abbreviations (second column), and their energy (third column). The neutrino fluxes predicted by the GS98 (High Metallicity) and AGSS09 (Low Metallicity) leading standard solar model [60], in units of ($\text{cm}^{-2}\text{s}^{-1}$), are listed in the fourth and fifth and sixth column.

$$p + e^- + p \rightarrow {}^2\text{H} + \nu_e \quad (1.44 \text{ MeV}) \quad (2.4)$$

The reaction (2.3), called *pp reaction*, is the basis for the whole *pp* chain. More than 99% of the terminations of the *pp* chain pass through the *pp* reaction. The rate for this primary reaction is too slow for to be measured in the laboratory at relevant energies since the reaction proceeds via the weak interaction. However, the rate can be calculated accurately using the theory of low-energy weak interactions and the measured properties of the proton-proton scattering and the deuteron. The neutrino emitted in this process, called *pp* ν , has a maximum energy of 0.42 MeV. The *pp* ν flux predicted by the SSM has the smallest uncertainties due to the solar luminosity constraint [70].

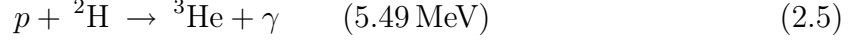
The reaction (2.4) is called *pep reaction*, and the mono-energetic (1.44 MeV) neutrino emitted in this process is called *pep* ν . The *pep* reaction is important in principle since the ratio of *pep* ν to *pp* ν is practically independent of the solar models, thus *pep* ν contain essentially the same information about the rate of the basic fusion reactions as do the lower energy *pp* ν . The rate for the *pep* reaction can be calculated accurately using weak interaction theory in terms of the rate of the *pp* reaction. The ratio between the *pep* and *pp* terminations, and therefore the ratio between *pep* ν and *pp* ν fluxes is ~ 0.04 . Due to the solar luminosity constraint, the flux of *pep* ν predicted by the SSM has the second lowest uncertainty (1.2%) [6, 70].

The *pp* and *pep* reactions proceed via the weak interaction, so their cross sections are lower respect to strong or electromagnetic processes in the chain. Therefore *pp* and *pep* reactions are a bottleneck for the *pp* chain, and basically determine the total nuclear fusion rate and the solar luminosity.

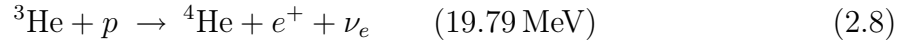
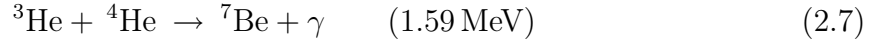
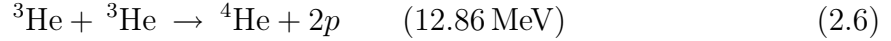
One of result of this PhD thesis is the first time direct detection of the *pep* solar neutrinos, and the corresponding measurement of the *pep* solar neutrino flux (see Sec. 5.10).

The $pp - I$ branch

The $pp - I$ branch of the pp chain proceeds through the reaction:



The ${}^3\text{He}$ nucleus can interact in three different ways:



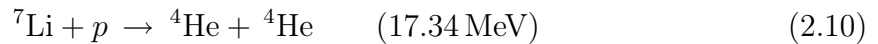
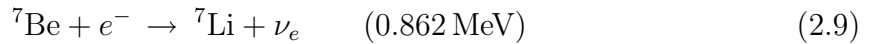
The cross sections of the reactions Eq. 2.5, Eq. 2.6, and Eq. 2.7 have been measured by the LUNA collaboration [71, 72, 73, 74, 75]. The reaction (2.6) is the dominant termination in the Sun, because of the abundance of ${}^3\text{He}$; SSMs predict this reaction to complete $\sim 85\%$ of pp chain terminations.

The reaction (2.8), called *hep reaction* is a weak interaction process which produces the highest-energy solar neutrinos. The neutrinos from this reactions are extremely rare, and have never been detected so far [76].

The reaction (2.7) leads to the two important neutrino-producing reactions involving ${}^7\text{Be}$. The two terminations involving the ${}^7\text{Be}$ nucleus are called $pp - II$ and $pp - III$.

The $pp - II$ branch

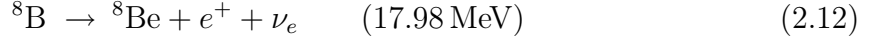
In the Sun, ${}^7\text{Be}$ is almost always destroyed by electron capture, usually from free electrons in the solar plasma:



The rate of the process (2.9) can be calculated accurately using weak interaction theory. The mono-energetic neutrino emitted in the electron capture of the ${}^7\text{Be}$ is called ${}^7\text{Be } \nu$. The ${}^7\text{Li}$ nucleus can be generated in an excited state with energy 487 keV, with branching factor of 10%. Therefore, the energy of ${}^7\text{Be } \nu$ can be either 862 keV or 384 keV. The flux of ${}^7\text{Be } \nu$ has been measured with a precision of 5% by the Borexino experiment [25, 77, 78].

The $pp - III$ branch

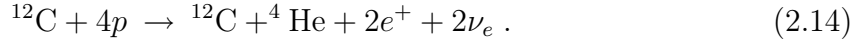
The ${}^7\text{Be} + p$ reaction occurs only rarely in the SSMs, in about 1 out of 5000 terminations of the pp chain (the ${}^7\text{Be}$ electronic capture reaction is about a thousand time more probable):



Nevertheless, this branch is of crucial importance since it leads to high energy ${}^8\text{B} \nu$. ${}^8\text{B} \nu$ s have an extremely historical importance: they have been the first detected solar neutrinos in the Homestake experiment in the 60s [55, 14], and their detection with different channel in SNO lead to first evidence of neutrino oscillation [22, 23, 79, 80]. The first time detection of ${}^8\text{B} \nu$ s with a 3 MeV threshold (kinetic energy of electron recoil) has been performed in Borexino [81].

2.4.2 The CNO chain

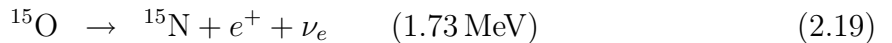
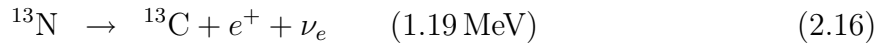
In the set of reaction in the *carbon-nitrogen-oxygen cycle* (CNO cycle), the overall conversion of four protons to form an helium nucleus, two positrons, and two electron neutrinos is achieved with the aid of ${}^{12}\text{C}$, the most abundant heavy isotope in normal stellar condition:



The total energy release is the same as for the pp chain (26.7 MeV).

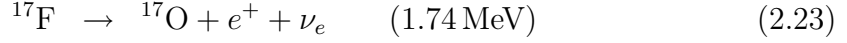
The energy production in the CNO cycle only constitutes a small contribution to the total luminosity in the Sun (of the order of $\sim 1\%$ in the SSMs). The Coulomb barrier between a proton and carbon or nitrogen nuclei is much higher than the one between two protons or helium nuclei, therefore the CNO cycle can only occur at temperature much higher than the temperature needed for pp chain [6]. The CNO cycle is believed to be the dominant mechanism of energy production massive stars ($> 1.5M_\odot$).

The CNO cycle have two sub-cycles: the CN cycle and the sub-dominant NO cycle. The NO cycle rate is about 2×10^{-2} the CN rate. The reactions in the CN cycle are:



The half lifes of ${}^{13}\text{N}$ and ${}^{15}\text{O}$ are about some minutes. The α -decay of the excited ${}^{16}\text{O}^*$ has a higher branching ratio respect to its γ decay. The cross sections of the reactions

Eq. 2.18 and Eq. 2.21, have been measured by the LUNA collaboration [82, 83, 84]. The γ -decay of $^{16}\text{O}^*$ is the first process in the NO cycle:



The neutrinos resulting from the CNO cycle are called CNO ν s. The energy spectrum of the CNO ν s is the sum of three continuous spectra with end point energies of 1.19 MeV (^{13}N), 1.73 MeV (^{15}O), and 1.74 MeV (^{17}F). The total predicted CNO ν s flux is strongly dependent on the inputs of the solar modelling, being 40% higher in the High Metallicity (GS98) than in the Low Metallicity (AGSS09) solar model (see Sec. 2.3, Table 2.4). The detection of neutrinos resulting from the CNO cycle has important implications in astrophysics, as it would be the first direct evidence of the nuclear process that is believed to fuel massive stars ($> 1.5M_{\odot}$). Furthermore, its measurement may resolve the solar metallicity problem.

One of the results of this PhD thesis is the strongest constraint of the CNO solar neutrino flux to date (see Sec. 5.10).

2.5 Propagation of solar neutrinos

The solar ν_e s undergo oscillations while they propagate from the central part of the Sun, where they are produced, to the terrestrial detector. Because of the large range of matter density in the Sun, matter effects (see Sec. 1.4) have a significant role in the solar neutrino oscillations. The electron number density N_e changes considerably along the neutrino path in the Sun: it decreases monotonically from the value of $\sim 100 \text{ cm}^{-3} N_A$ in the centre of the Sun to 0 at the surface of the Sun. According to the contemporary solar models, N_e decreases approximately exponentially in the radial direction towards the surface of the Sun:

$$N_e(t) = N_e(t_0) \exp\left(-\frac{t - t_0}{r_0}\right), \quad (2.25)$$

where $(t - t_0) \simeq d$ is the distance travelled by the neutrino in the Sun, $N_e(t_0)$ is the electron number density at the point of ν_e production in the Sun, r_0 is the scale-height of the change of $N_e(t)$ and one has [6, 58] $r_0 \sim 0.1R_{\odot}$.

Consider the case of 2-neutrino mixing in matter, Eq. (1.31). If N_e changes with t (or equivalently with distance) along the neutrino trajectory, the matter-eigenstates, their energies, the mixing angle, and the oscillation length in the matter become, through their dependence on N_e , also functions of t . The behaviour of the neutrino system can be understood in term of a two-level system whose Hamiltonian depends on time. The relevant cases for solar neutrinos, are that the electron number density at the point of a solar ν_e production in the Sun much bigger, or much smaller than the resonance density.

In the case $N_e(t_0) \gg N_e^{res}$, $\theta_m(t_0) \simeq \pi/2$ and the state of the electron neutrino in the initial moment of evolution of the system practically coincides with the heavier of

the two matter eigenstates:

$$|\nu_e\rangle \simeq |\nu_2^m(t_0)\rangle . \quad (2.26)$$

When neutrinos propagate to the surface of the Sun they cross a layer of matter in which $N_e = N_e^{res}$. Correspondingly, the evolution of the neutrino system can proceed basically in two ways: either evolve adiabatically or jump.

In the *adiabatic evolution*, characterised by the negligible probability of the jump from the upper matter eigenstate to the lower matter eigenstate, the system can stay on the state $|\nu_2^m(t)\rangle$ up to the final moment t_s , when the neutrino reaches the surface of the Sun. At the surface of the Sun $N_e(t_s) = 0$ and therefore $\theta_m(t_s) = \theta$, $|\nu_{1,2}^m(t_s)\rangle = |\nu_{1,2}\rangle$. Thus, in this case the state describing the neutrino system at t_0 will evolve continuously into the state $|\nu_2\rangle$ at the surface of the Sun. The probabilities to find ν_e and ν_μ at the surface of the Sun are then (Eq. (1.23)):

$$P(\nu_e \rightarrow \nu_e; t_s) \simeq |\langle \nu_e | \nu_2 \rangle|^2 = \sin^2 \theta \quad (2.27)$$

$$P(\nu_e \rightarrow \nu_\mu; t_s) \simeq |\langle \nu_\mu | \nu_2 \rangle|^2 = \cos^2 \theta . \quad (2.28)$$

Under the assumption made, a $\nu_e \rightarrow \nu_\mu$ conversion with $P > 0.5$ is possible.

The other possibility is realised if in the resonance region the system jumps from the upper matter eigenstate to the lower matter eigenstate and after that the system continues to be in the state $|\nu_1^m(t)\rangle$ until the neutrino reaches the surface of the Sun.

The value of the jump probability P' plays a crucial role in the solar neutrino oscillations. There exist a whole spectrum of possibilities since P' can have any value from 0 to $\cos^2 \theta$ [85, 86]. In the literature, the transitions are called *nonadiabatic* if P' is non negligible. In order for the evolution to be adiabatic, $N_e(t)$ should change sufficiently slow along the neutrino path [87]. Numerical studies have shown [42] that solar neutrinos can undergo both adiabatic and nonadiabatic transition, and the matter effect can be substantial in the solar neutrino oscillations for $10^{-8} \text{eV}^2 < \Delta m_{sun}^2 < 10^{-4} \text{eV}^2$ and $10^{-4} < \sin^2 2\theta_{sun} < 1.0$.

The evolution equations Eq. (1.28) for the neutrino state in matter can be solved exactly for N_e changing exponentially, as in Eq. (2.25), along the neutrino path in the Sun [85, 88]. On the basis of the exact solution it was possible to derive a complete and accurate analytic description of the matter-enhanced transitions of solar neutrinos in the Sun for any values of Δm_{sun}^2 and θ_{sun} [41, 42, 85, 86].

The survival probability for a ν_e produced in the central part of the Sun on its way to the surface of the Sun is given by

$$P_{\odot}^{2\nu}(\nu_e \rightarrow \nu_e) = \frac{1}{2} + \left(\frac{1}{2} - P'\right) \cos 2\theta_m \cos 2\theta , \quad (2.29)$$

where θ_m is the mixing angle in matter at the point of ν_e production and the jump probability P' in terms of Δm^2 , $\sin^2 \theta$, the neutrino energy E , and r_0 (Eq. 2.25) is given in [85]. This equation is only valid for the convention $\Delta m_{21}^2 > 0$ but for both signs of $\cos 2\theta_{12}$.

The current solar neutrino and KamLAND data suggest that $\Delta m_{21}^2 \simeq 7.6 \cdot 10^{-5} \text{eV}^2$. For $\Delta m_{21}^2 > 10^{-7} \text{eV}^2$, the averaging over the region of neutrino production in the Sun renders negligible all interference terms which appear in Eq. (1.25). Thus, the survival

probability of a ν_e while it travels from the central part of the Sun to the surface of the Earth is effectively equal to the survival probability of the ν_e while it propagates from the central part to the surface of the Sun (Eq. (2.29)).

If the solar ν_e transitions are adiabatic, $P' \simeq 0$ and $\cos 2\theta_m \simeq -1$, the survival probability given by Eq. (2.29) becomes [42]

$$P_{\odot}^{2\nu}(\nu_e \rightarrow \nu_e) \simeq \frac{1}{2} - \frac{1}{2} \cos 2\theta = \sin^2 \theta. \quad (2.30)$$

The solar neutrino and KamLand data⁴ suggest $\sin^2 2\theta_{12} \sim 0.8$. For such mixing angle, the adiabatic transitions are realised if $E/\Delta m^2$ lies approximately in the range $(2 \cdot 10^4 - 3 \cdot 10^7) \text{ MeV/eV}^2$ [86]. This result is relevant for the interpretation of the solar ${}^8\text{B}$ ν data, detected by Super-Kamiokande, SNO and Borexino. The measured survival probability for ${}^8\text{B}$ ν of energy $E > 5 \text{ MeV}$ is $P(\nu_e \rightarrow \nu_e) \simeq 0.3$. A solar ν_e survival probability $< 1/2$ is not allowed by oscillations in vacuum (Eq. (1.26)), therefore the data evidence that ${}^8\text{B}$ ν oscillations are driven by matter effects. The survival probability given in Eq. (2.30) is indeed either bigger or smaller than $1/2$ depending on the sign of $\cos 2\theta$. Thus, the possibility of $\cos 2\theta < 0$ is ruled out by the data. Given the convention $\Delta m_{21}^2 > 0$ adopted, the data imply that $\Delta m_{21}^2 \cos 2\theta_{12}$. The solar ν_e oscillation undergoing for $E > 5 \text{ MeV}$ are often called *Matter Enhanced*.

If $E/\Delta m^2$ is sufficiently small so that $N_e(t_0) \ll N_e^{res}$, we have $P' \simeq 0$, $\theta_m \simeq 0$ and the oscillations take place in the Sun as in vacuum [42]:

$$P_{\odot}^{2\nu}(\nu_e \rightarrow \nu_e) \simeq 1 - \sin^2 2\theta, \quad (2.31)$$

which is the average two-neutrino survival probability in vacuum (Eq. (1.26)). This expression describes with good precision the transitions of the solar pp ν . The solar ν_e oscillation undergoing in the energy region of pp ν s are often called *Vacuum Dominated*.

The energy region between the vacuum dominated and matter enhanced solar ν_e oscillation regime is called *Transition Region*. The current framework of solar neutrino oscillation, MSW-LMA, predicts a smooth transition of the ν_e survival probability between the two regions, resulting in an energy dependent ν_e survival probability P_{ee} . The solar ν_e survival probability as a function of the energy and the corresponding P_{ee} measurement from solar neutrinos are shown in Fig. 5.25.

The solar ν_e survival probability in the case of 3-neutrino mixing takes a simple form for $|\Delta m_{31}^2| \gg |\Delta m_{21}^2|$. Indeed, for the energies of solar neutrinos $E < 10 \text{ MeV}$, N_e^{res} corresponding to Δm_{31}^2 satisfies $N_e(t_0) \ll N_e^{res}$. As a consequence, the oscillations due to Δm_{31}^2 proceed as in vacuum. The averaging over the region of ν_e production in the Sun strongly suppress the oscillations due to Δm_{31}^2 . The 3-neutrino solar ν_e survival probability is then [89, 90]:

$$P_{\odot}^{3\nu}(\nu_e \rightarrow \nu_e) \simeq \sin^4 \theta_{13} + \cos^4 \theta_{13} P_{\odot}^{2\nu}(\Delta m_{21}^2, \theta_{12}; N_e \cos^2 \theta_{13}), \quad (2.32)$$

where $P_{\odot}^{2\nu}(\Delta m_{21}^2, \theta_{12}; N_e \cos^2 \theta_{13})$ is given by Eq. (2.29) in which $\Delta m^2 = \Delta m_{21}^2$, $\theta = \theta_{12}$ and the solar e^- number density N_e is replaced by $N_e \cos^2 \theta_{13}$.

⁴ in the literature, the configuration of Δm_{21}^2 and θ_{12} suggested by the solar neutrino and KamLand data is often called Large Mixing Angle (LMA). Recently, the Borexino collaboration have validated the LMA configuration with solar ν_e only, i.e. without using KamLand $\bar{\nu}_e$ data and the assumption of CPT invariance [26]

2.6 Detection of solar neutrinos

So far, solar neutrinos have been observed by chlorine (Homestake) and gallium (SAGE, GALLEX and GNO) radiochemical detectors and water Cherenkov detectors using light water (Kamiokande and Super-Kamiokande) and heavy water (SNO). Recently, low energy solar neutrinos have been successfully observed by the liquid scintillator detector Borexino.

A pioneering solar neutrino experiment by Davis and collaborators at Homestake using the $^{37}\text{Cl} - ^{37}\text{Ar}$ method proposed by Pontecorvo [91] started in the late 1960's. This experiment exploited ν_e absorption on ^{37}Cl nuclei followed by the produced ^{37}Ar decay through orbital e^- capture,

$$\nu_e + ^{37}\text{Cl} \rightarrow ^{37}\text{Ar} + e^- . \quad (2.33)$$

The neutrino energy threshold is 814 keV. The ^{37}Ar nuclei produced are radioactive, with a half life ($\tau_{1/2}$) of 34.8 days. After an exposure of the detector for two or three times $\tau_{1/2}$, the reaction products were chemically extracted and introduced into a low background proportional counter, where they were counted for a sufficient long period to determine the exponentially decaying signal and a constant background. Solar model calculations predict that the dominant contribution in the chlorine experiment came from ^8B neutrinos, but ^7Be , pep and CNO neutrinos also contributed.

From the very beginning of the solar neutrino observations [55], it was recognised that the observed flux was significantly smaller than the SSM predictions, provided nothing happens to the ν_e after the creation in the solar interior. This deficit has been called *the Solar Neutrino problem*.

Gallium experiments (GALLEX and GNO at Gran Sasso in Italy and SAGE at Baksan in Russia) exploit the reaction

$$\nu_e + ^{71}\text{Ga} \rightarrow ^{71}\text{Ge} + e^- . \quad (2.34)$$

The neutrino energy threshold is 233 keV. The dominant contribution is given by the most abundant pp neutrinos. However, the solar model calculations predict almost half of the capture rare in gallium due to other solar neutrinos. GALLEX presented the first evidence of pp ν observation in 1992 [16]. The GALLEX Collaboration finished observations in early 1977 [17]. Since April, 1998, the GNO (Gallium Neutrino Observatory) collaboration continued the observation until April 2003. The GNO and GNO + GALLEX joint analysis results are presented in [18]. SAGE initially reported very low flux [92], but later observed similar flux to that of GALLEX. The latest SAGE results are published in [19]. The SAGE experiment continues to collect data.

In 1987, the Kamiokande experiment in Japan succeeded in real-time solar neutrino observations, exploiting ν_e scattering,

$$\nu_x + e^- \rightarrow \nu_x + e^- , \quad (2.35)$$

in a large water-Cherenkov detector. This experiment takes advantage of the directional correlation between the incoming neutrino and the recoil electron. This feature greatly helps the clear separation of the solar-neutrino signal from the background. The

Kamiokande result gave the first direct evidence that neutrinos come from the direction of the Sun [93]. Later, the high-statistics Super-Kamiokande experiment [94, 95, 21] with a 50-kton water Cherenkov detector replaced the Kamiokande experiment. Due to high thresholds (7 MeV in Kamiokande and 5 MeV at present in Super-Kamiokande) the experiments observe pure ^8B solar neutrinos. The $\nu - e$ elastic scattering is sensitive to all active neutrinos $x = e, \mu, \tau$. However, the sensitivity to ν_μ and ν_τ is much smaller than the sensitivity to ν_e , being $\sigma(\nu_{\mu,\tau} - e) \sim 0.16\sigma(\nu_e - e)$.

In 1999, a new real time solar neutrino experiment, SNO (Sudbury Neutrino Observatory), in Canada started observation. This experiment used 100 tons of ultra-pure heavy water (D_2O) contained in a spherical acrylic vessel, surrounded by an ultra-pure H_2O shield. SNO measured ^8B solar neutrinos via the charged-current (CC) and neutral current (NC) reactions

$$\nu_e + d \rightarrow e^- + p + p \quad (CC), \quad (2.36)$$

and

$$\nu_x + d \rightarrow \nu_x + p + n \quad (NC), \quad (2.37)$$

as well as ν_e elastic scattering on electron (Eq. (2.35)). The CC reaction is sensitive only to ν_e , while the NC reaction is sensitive to all active neutrinos. This is a key feature to solve the solar neutrino problem. If it is caused by flavour transition such as neutrino oscillations, the solar neutrino fluxes measured by CC and NC reactions would show a significant difference. The neutrino energy threshold of the CC reaction is 1.4 MeV and the e^- energy is strongly correlated with the ν_e energy. Thus, the CC reaction provides an accurate measure of the shape of the ^8B ν energy spectrum. The contributions from CC reaction and ν_e scattering can be distinguished by using different $\cos \phi$ distributions, where ϕ is the angle of the e^- momentum with respect to the Sun-Earth axis. While the ν_e elastic scattering events have a strong forward peak, CC events have an approximate angular distribution of $1 - 1/3 \cos \phi$. The neutrino energy threshold of the NC reaction is 2.2 MeV. In the pure D_2O [22, 23], the signal of the NC reaction was neutron capture in deuterium, producing a 6.25 MeV γ -ray. In this case, the capture efficiency was low and the deposited energy was close to the detection threshold of 5 MeV. In order to enhance both the capture efficiency and the total γ -ray energy (8.6 MeV), 2 tons of NaCl were added to the heavy water in the second phase of the experiment [79]. Subsequently NaCl was removed and an array of ^3He neutron counters were installed for the third phase measurement [80]. These neutrons counters provided independent NC measurement with different systematics from that of the second phase, and thus strengthened the reliability of the NC measurement.

Borexino at Gran Sasso in Italy started solar neutrino observation in May 2007. Borexino detects solar neutrinos via ν_e scattering in 300 tons of ultra-pure liquid scintillator [96]. The flux of the mono-energetic 862 keV ^7Be solar neutrinos has been directly observed for the first time [78, 77]. Recently, a precise measurement of the ^7Be ν at 5% precision has been published by the Borexino collaboration [25]. Borexino has also measured solar ^8B ν with an analysis threshold as low as 3 MeV (effective electron kinetic energy) [81]. The first time detection of pep and the strongest limits so far on CNO solar neutrinos in Borexino are the results of this PhD thesis. More details on the Borexino detector and the pep and CNO solar neutrinos analysis will be given

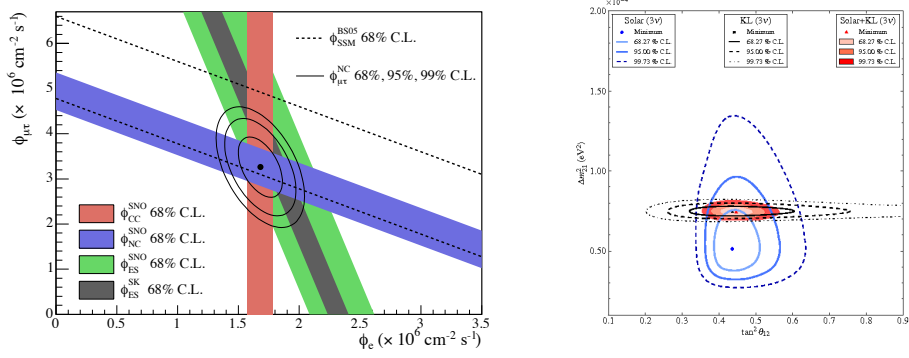


Figure 2.2: **Left panel:** Fluxes of ${}^7\text{Be}$ solar neutrinos, $\Phi(\nu_e)$ and $\Phi(\nu_\mu \text{ or } \nu_\tau)$, deduced from the SNO's CC, ES and NC results of the salt phase measurement [79]. The BS05(OP) standard solar model prediction [57] is also shown. **Right panel:** Three-flavor neutrino oscillation analysis contour for Δm_{21}^2 and θ_{12} , using both solar ν_e and KamLand $\bar{\nu}_e$ results. This figure is taken from [98].

in the Section 5. Measurements of low energy solar neutrinos are important not only to test the SSM further, but also to study the MSW effect over the energy region spanning from sub-MeV to 10 MeV.

2.7 Oscillation of solar neutrinos

The results from all the solar neutrino experiments, except SNO's NC result, indicate significantly less flux than expected from the solar-model prediction. This deficit has been understood as due to neutrino flavor conversion. In 2001, the initial SNO CC result combined with the Super-Kamiokande's high-statistics $\nu_e e$ elastic scattering result [76] provided direct evidence for the flavour conversion of solar neutrinos [22]. Later, SNO's NC measurements further strengthened this conclusion [23]. Fig. (2.2) shows the salt phase result of the flux of ν_μ or ν_τ versus the flux of ν_e . The non-zero flux of ν_μ or ν_τ is a strong evidence for the neutrino flavor conversion. These results are consistent with those expected from the LMA (large mixing angle) solution of solar neutrino oscillation in matter [41, 42] with $\Delta m_{sun}^2 \sim 5 \cdot 10^{-5} \text{ eV}^2$ and $\tan^2 \theta_\odot \sim 0.45$. However, with the SNO data alone, the possibility of other solutions cannot be excluded with sufficient statistical significance.

The KamLAND experiment in Japan observed reactor $\bar{\nu}_e$ disappearance, with a flux-weighted average distance of $\sim 180 \text{ km}$ between source and detector [29]. Under the assumption of CPT invariance in the neutrino sector, a combined global solar ν_e + KamLAND $\bar{\nu}_e$ analysis showed that the LMA is the unique solution to the solar neutrino problem with $> 5\sigma$ CL [97]. A combined global solar analysis using the recent high-statistics measurement of the absence of day-night asymmetry of the ${}^7\text{Be}$ ν in Borexino have shown that the LMA is the unique solution without using $\bar{\nu}_e$ data from KamLand, *i.e.* without assuming CPT invariance [26].

The mixing angle θ_{12} and the mass splitting Δm_{21}^2 in two-neutrino and three-neutrino

oscillation framework are obtained from a global analysis including all the solar neutrino (SNO, Super-Kamiokande, chlorine, gallium, and Borexino) and the KamLAND data. One recent update can be found in [98]. The allowed parameter regions obtained from [98] are shown in Fig. 2.2. The best fit parameters obtained from the global solar + KamLAND analysis are $\Delta m_{21}^2 = 7.46_{-0.19}^{+0.20} \cdot 10^{-5} \text{eV}^2$ and $\tan^2 \theta_{12} = 0.427_{-0.024}^{+0.027}$, and those from the global solar analysis are $\Delta m_{21}^2 = 5.13_{-0.96}^{+1.29} \cdot 10^{-5} \text{eV}^2$ and $\tan^2 \theta_{12} = 0.427_{-0.028}^{+0.028}$.

2.8 Conclusions and outlook

The MSW-LMA scenario is our current understanding of solar neutrino oscillations. This scenario yields to an electron neutrino survival probability P_{ee} that depends on the neutrino energy. The energy dependence $P_{ee}(E)$ is predicted with high accuracy in the context of MSW-LMA oscillations and the Solar Standard Model (see Sec. 2.4).

Before the Borexino measurements, precision tests to the P_{ee} , thus to MSW-LMA oscillations, were only available with high energy ^8B solar neutrinos, in the matter-enhanced energy region. Spectral measurements or high precision measurements of sub MeV solar neutrinos, in the vacuum-dominated energy region, were not available. Before Borexino, the detection of sub MeV solar neutrinos were only performed with gallium and chlorine radiochemical experiments, which are only sensitive the total neutrino flux above the reaction threshold. Thus, the predictions of the MSW-LMA scenario in the vacuum-dominated and transition region of the P_{ee} were poorly tested.

Moreover, reactor neutrino experiments are only sensitive to $\bar{\nu}_e$, therefore one has to assume that ν_e oscillations behave in the same way of $\bar{\nu}_e$ oscillations (*i.e.* CPT invariance holds in the neutrino sector) in order to combine ν_e and $\bar{\nu}_e$ oscillation data to determine the oscillation parameters and test the oscillation models.

A direct measurement of low energy pp , ^7Be , and pep solar neutrino flux is needed in order to test the MSW-LMA prediction in the vacuum-dominated and transition energy region. A real-time experiment also allows searches for day-night asymmetries, which can be used to further test the oscillation models.

Spectral measurements of sub-MeV solar neutrinos are also valuable for solar physics. In particular, a measurement of the CNO neutrino flux may help solving the solar metallicity controversy (see Sec. 2.3).

The Borexino detector has been built with the goal of providing an high precision measurement of ^7Be solar neutrinos and potentially measure pep and CNO solar neutrinos.

Chapter 3

The Borexino experiment

3.1 Introduction

Borexino is a large volume liquid scintillator detector [96]. It is located deep underground (~ 3800 m of water equivalent) in the Hall C of the Laboratori Nazionali del Gran Sasso (LNGS) in Italy, where the muon flux is suppressed by a factor $\sim 10^6$.

The main goal of the experiment is the detection of low energy solar neutrinos, such as the ${}^7\text{Be}$ solar neutrinos, whose precision detection is the primary goal of Borexino, and *pep* and CNO solar neutrinos, whose detection is the argument of this PhD thesis. The motivating physics goal of low energy solar neutrino detection is to directly probe the nuclear reaction processes in the Sun, and explore neutrino oscillations over a broader range of energies than has been done to date.

Recent solar neutrino results of Borexino include a high-precision measurement of ${}^7\text{Be}$ neutrinos [25], the measurement of day-night asymmetry of ${}^7\text{Be}$ solar neutrinos [26], a measurement of ${}^8\text{B}$ solar neutrinos with a threshold recoil electron energy of 3 MeV [81], and the first time direct evidence of *pep* solar neutrinos and the strongest constraint up to date on CNO solar neutrinos [1]. Other recent results beside solar neutrino physics include the study of solar and other unknown anti-neutrino fluxes [99], observation of Geo-Neutrinos [100], and experimental limits on the Pauli-forbidden transitions in ${}^{12}\text{C}$ nuclei [101]. The physics goal of the experiment also include the detection of a nearby supernova, the measurement of the time of flight of ν_μ between CERN and LNGS, the search for sterile neutrinos and neutrino magnetic moment by means of a powerful neutrino source, and the search for very rare events like the electron decay.

In Borexino low energy neutrinos of all flavors are detected by means of their elastic scattering of electrons. The electron recoil energy is converted into scintillation light which is then collected by a set of photomultipliers (PMTs).

This technique has several advantages over both the water Cherenkov detector and the radiochemical detectors used so far in solar neutrino experiments. Water Cherenkov detectors, in fact, cannot effectively detect solar neutrinos whose energy is below few MeV, both because the Cherenkov light yield is low and because the intrinsic radioactive background cannot be reduced to sufficiently low levels. On the other hand, radiochemical experiments cannot intrinsically perform spectral measurements and do not detect events in real time.

An organic liquid scintillator solves the aforementioned problems: the low energy neutrino detection is possible because of the high light yield that in principle allow the energy threshold to be set down to a level of a few tens of keV¹; the organic nature of the scintillator, and its liquid form at the ambient temperature, provide very low solubility of ions and metal impurities, and yield the technical possibility to purify the material as request. However, being the scintillator light emitted isotropically, no measurement of the direction of the incoming neutrino is possible and the neutrino induced events are intrinsically indistinguishable from β and γ radioactivity, posing formidable requirements in terms of radiopurity of the scintillator and of the detector materials.

The order of magnitude of sub-MeV solar neutrino interaction rate is a few tens counts/day for about 100 ton of active target material and with an energy threshold of 200 keV. This rate corresponds to an equivalent activity of $\sim 10^{-9}$ Bq/kg. If one compares this low number with a the typical radioactivity of materials (air and drinking water ~ 10 Bq/kg, rock ~ 100 -1000 Bq/kg) one can see that the core of the Borexino detector must be 9-10 orders of magnitude less than anything in the Earth in order to perform low energy solar neutrino measurement. Typical radioactive contaminants in solid materials and water are ^{238}U and ^{232}Th daughters, and ^{40}K . Air and commercial available nitrogen are typically contaminated by noble gas like ^{222}Rn , ^{85}Ar , and ^{85}Kr .

The necessity to measure such a low neutrino flux with a massive detector poses severe requirements in term of radiopurity for the scintillator itself and for the surrounding materials. Additionally, the neutrino target (~ 100 ton of fiducial volume in Borexino) must be almost completely shielded from external γ radiation and neutrons originating from the rock and from the detector materials.

For almost 20 years the Borexino collaboration has been addressing this problem by developing suitable purification techniques for scintillator, water, and nitrogen, by performing careful material selections, by developing innovative cleaning techniques for material surfaces. Purification processes to remove radioactive impurities to achieve the internal background requirements were investigated in earlier studies with the prototype of the Borexino detector, the Counting Test Facility (CTF) [102, 103]. Following the successful CTF research, the basic strategy employed for Borexino is to purify the scintillator with a combination of distillation, water extraction, and nitrogen gas stripping, all standard processes, but adapted for high cleanliness and low radioactivity. The special procedures for scintillator purification and material fabrication resulted in very low internal backgrounds. The current low background has made possible measurements of ^7Be neutrinos with high accuracy, measurements of ^8B and *pep* neutrinos, and strong limits on CNO neutrinos.

This chapter is devoted to describe the detection of solar neutrinos in the Borexino experiment. The chapter is organised as follows. In Section 3.2 I review the solar neutrino signal detection in Borexino. In Section 3.3, the Borexino detector is described briefly. Section 3.4 report on the Borexino scintillator and the scintillation mechanism. Special care has been taken in the description of the quenching effect, the time response and pulse shape discrimination. In Section 3.5 I describe the Borexino energy spectrum

¹However, the unavoidable contamination of ^{14}C that is present in any organic liquid practically limits the neutrino detection window above ~ 200 keV.

and the basic analysis methods which lead to the high precision measurement of ${}^7\text{Be}$ solar neutrino rate.

3.2 Neutrino detection in Borexino

In Borexino low energy neutrinos of all flavors are detected by means of their elastic scattering of electrons:

$$\nu_x + e^- \rightarrow \nu_x + e^- . \quad (3.1)$$

In elastic scattering, the incoming neutrino is deflected through an angle θ with respect to its original direction. The neutrino transfers a portion of its energy to the electron (assumed to be initially at rest), which is then known as a *recoil electron*. Because all angles of scattering are possible, the kinetic energy transferred to the electron can vary to zero to a large fraction of the neutrino energy.

The expression that relates the energy transfer and the scattering angle for any given elastic scattering interaction can be derived by writing simultaneous equations for the conservation of energy and momentum. One can easily show that

$$E'_\nu = \frac{E_\nu}{1 + \frac{E_\nu}{m_e c^2} (1 - \cos \theta)} , \quad (3.2)$$

where m_e is the mass of the electron (0.511 MeV), E_ν is the energy of the incoming neutrino, and E'_ν is the energy of the neutrino after interaction. The kinetic energy of the recoil electron is

$$T_e = E'_\nu - E_\nu . \quad (3.3)$$

For small scattering angles θ , very little energy is transferred. Some of the original energy is always retained by the incident neutrino, even in the extreme case of $\theta = \pi$, when energy transfer to the recoil electron is maximum. The maximum kinetic energy of an electron that undergoes elastic scattering with a neutrino of energy E_ν is then

$$T_e^{max} = \frac{E_\nu}{1 + \frac{m_e c^2}{2E_\nu}} . \quad (3.4)$$

For the monoenergetic 862 keV ${}^7\text{Be}$ and 1.44 MeV *pep* solar neutrinos, T_e^{max} is respectively at 665 keV and 1.22 MeV.

The rate of $\nu - e$ elastic scattering interaction in a given target is the product of the incoming neutrino flux, the number of electrons in the target, and the elastic scattering cross section, integrated over the energy range of the neutrino flux. In the case of Borexino, the incoming neutrino flux is the solar neutrino flux, whose magnitude and spectrum is discussed in Sec. 2.4, and the target is the pseudocumene within the fiducial volume used in the analysis.

The cross section of the $\nu - e$ elastic scattering interaction is well known, and its expression can be derived in the framework of the standard model of particle physics. At the lowest order in perturbation theory, the differential cross section is:

$$\frac{d\sigma_\nu}{dT_e}(E_\nu, T_e) = \frac{\sigma_e}{m_e} \left[g_l^2 + g_r^2 \left(1 - \frac{T_e}{E_\nu} \right)^2 - g_l g_r \frac{m_e T_e}{E_\nu^2} \right] , \quad (3.5)$$

where

$$\sigma_e = \frac{2G_F^2 m_e^2}{\pi \hbar^4} = 88.06 \cdot 10^{-46} \text{ cm}^2, \quad (3.6)$$

$g_l = \pm \frac{1}{2} + \sin^2 \theta_W$, and $g_r = \sin^2 \theta_W \simeq 0.23$, where θ_W is the electroweak mixing angle. In case of ν_e elastic scattering $g_l^{(\nu_e)} \simeq 0.73$, while for ν_μ and ν_τ $g_l^{(\nu_{\mu,\tau})} \simeq -0.27$. Radiative corrections to the electron recoil energy spectra and to the total cross sections are computed for $\nu-e$ elastic scattering by solar neutrinos in [104]. Radiative corrections change monotonically the electron recoil spectrum for incident ^8B solar neutrinos, with the relative probability of observing recoil electrons being reduced by about 4% at the highest electron energies. For pp and ^7Be solar neutrinos, the recoil spectra are not affected significantly.

Borexino can detect neutrinos of all flavors, but ν_e have a larger cross section than ν_μ and ν_τ , because ν_e interact through charged and neutral current, while ν_μ and ν_τ interact only via the neutral current. The ratio of the cross sections, evaluated at different neutrino energy ranges, is:

$$\left(\frac{\sigma_{\nu_\mu, \nu_\tau}}{\sigma_{\nu_e}} \right)_{E_{\nu_{pp}}} \sim \frac{1}{3.7}, \quad \left(\frac{\sigma_{\nu_\mu, \nu_\tau}}{\sigma_{\nu_e}} \right)_{E_{\nu_{Be}}} \sim \frac{1}{4.7}, \quad \left(\frac{\sigma_{\nu_\mu, \nu_\tau}}{\sigma_{\nu_e}} \right)_{E > 5 \text{ MeV}} \sim \frac{1}{6.6} \quad (3.7)$$

Considering also the oscillation of solar neutrinos, the total rate R of $\nu - e$ elastic scattering interactions expected in Borexino is:

$$R = N_e \int dE \frac{d\Phi}{dE}(E) \left(P_{ee}(E) \sigma_{\nu_e}(E) + (1 - P_{ee}(E)) \sigma_{\nu_\mu, \nu_\tau}(E) \right), \quad (3.8)$$

where N_e is the number of electron in the active target, $\frac{d\Phi}{dE}$ is the differential energy spectrum of the considered solar neutrinos, and $P_{ee}(E)$ is the survival probability for solar ν_e of energy E . The expected interaction rate in Borexino for the each solar neutrino component is reported in Table 3.1.

The electron scattered by neutrinos are detected by means of the scintillation light, retaining the information on the kinetic energy of the electron. The information on the direction of the recoil electrons is lost, because the scintillation light is emitted isotropically. The scintillation light is detected with an array of 2200 photomultiplier tubes mounted on the inside surface of the stainless steel sphere. The number of photomultipliers hit is a measure of the energy imparted to the electron, but has no sensitivity to the direction of the neutrino. The position of the scintillation event is determined by a photon time-of-flight method.

The neutrino induced events are intrinsically indistinguishable from β and γ decays. To discriminate between the neutrino events and β and γ decay events, a careful analysis on the energy spectrum of the detected events is performed. The basic signature for monoenergetic neutrinos (like ^7Be or pep solar neutrinos) in the energy spectrum is a box-like edge of the recoil electrons, with end point at T_e^{max} . The exact shape of the energy spectrum of the events induced by neutrino interactions is governed by the solar neutrino energy spectrum and the $\nu - e$ elastic scattering differential cross section.

Solar neutrino	Electron recoil end point [MeV]	Expected rate [counts/(day·100ton)]	Main backgrounds in Borexino
pp	0.26	133	^{14}C
^7Be	0.665	47.3 ± 3.4	^{85}Kr , ^{210}Bi
pep	1.22	2.80 ± 0.04	^{11}C , ^{210}Bi
CNO	1.52	5.4 ± 0.8 ($3.8^{+0.6}_{-0.5}$)	^{11}C , ^{210}Bi
^8B	17.72	0.49 ± 0.05	^{208}Tl , Ext. γ

Table 3.1: The expected interaction rate in Borexino for the main solar neutrino components. Borexino has already directly measured the rates of ^7Be , pep , and ^8B solar neutrinos and has put limits on the interaction rate due to CNO solar neutrinos [25, 26, 1, 81]. The pp solar neutrinos might be directly measured in future by Borexino. The expected rates are based on the latest high metallicity SSM, using MSW - LMA oscillation parameters [2, 59]. For CNO neutrinos, the expected interaction rate based on the low metallicity SSM is also reported. In the second column, the electron recoil spectrum end points T_e^{max} , computed with Eq. 3.4, are reported. The prominent backgrounds for the detection of each solar neutrino component in Borexino are listed in the last column.

3.3 General description of the Borexino detector

The Borexino detector is extensively described in Refs. [96, 105, 106]. In this section, the main features of the Borexino detector are recalled. The purification techniques and plants are covered in [107, 108]. The Borexino detector is schematically depicted in Figure 3.1-Left.

Borexino is a scintillator detector with an active mass of 278 tons of pseudocumene (PC, 1,2,4-trimethylbenzene $\text{C}_6\text{H}_3(\text{CH}_3)_3$), doped with 1.5 g/l of flour PPO (2, 5-trimethylbenzene, $\text{C}_{15}\text{H}_{11}\text{NO}$) as a solute [109, 110]. The PC/PPO solution adopted in Borexino as a liquid scintillator satisfies specific requirements: high scintillation yield ($\sim 10^4$ photons/MeV), high light transparency [111], and fast decay time (~ 3 ns), all essential for good energy resolution and good discrimination between β -like events and events due to α decays.

The scintillator is contained in a thin ($125 \mu\text{m}$) nylon vessel (Inner Vessel, IV) [112] and is surrounded by two concentric PC buffers (323 and 567 tons) doped with 5.0 g/l of DMP (dimethylphthalate) that is added as a light quencher in order to further reduce the scintillation yield of pure PC. The two PC buffers are separated by a second thin nylon membrane (Outer Vessel, OV) to prevent ^{222}Rn emanated from the external materials to diffuse towards the scintillator. The scintillator and buffers are contained in a stainless steel sphere (SSS) with diameter 13.7 m. A picture of the inner and outer vessel taken during a calibration campaign is shown in Fig. 3.1-Right.

The scintillation light is detected via 2212 8" PMTs uniformly distributed on the inner surface of the SSS [113, 114]. For each detected photon, the arrival time and the charge are measured by means of a suitable analog and digital electronics chain. The Borexino main trigger fires when at least N_{thr} PMTs each detected at least one photo-

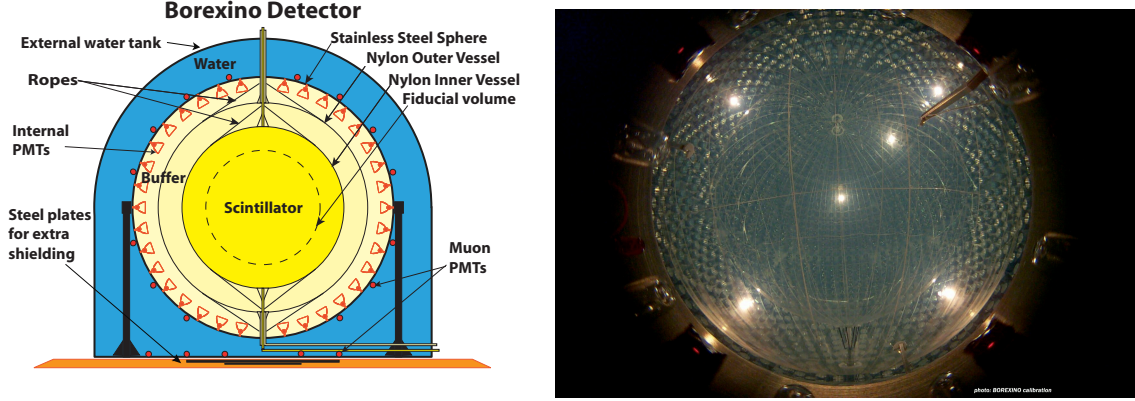


Figure 3.1: **Left:** Schematic drawing of the Borexino detector [96]. **Right:** The inner and outer nylon vessels in the Stainless Steel Sphere.

electron within a time window of 60 ns. The typical value is $N_{\text{thr}} = 25$, corresponding approximately to an energy threshold of 60 keV. When a trigger occurs, the time and charge of each PMT that has detected at least one photoelectron in a time gate of $16 \mu\text{s}$ is recorded. The time is measured by a Time to Digital Converter (TDC) with a resolution of about 0.5 ns, while the charge (after integration and pulse shaping) is measured by means of an 8 bit Analog to Digital Converter (ADC). This time resolution is smaller than the intrinsic time jitter of the PMTs which is 1.1 ns.

The stainless steel sphere of Borexino is enclosed in a 18.0 m diameter, 16.9 m high domed water tank (WT), containing 2100 tons of ultrapure water as an additional shielding against external backgrounds (γ -rays and neutrons from the rock). Additional 208 8" PMTs instrument the water tank and detect the Cherenkov light radiated by muons in the water shield, serving as a muon counter and muon tracker [105]. The muon flux, although reduced by a factor of $\sim 10^6$ by the 3800 m water equivalent depth of the Gran Sasso Laboratory, is of the order of $1 \text{ m}^{-2}\text{h}^{-1}$, corresponding to ~ 4300 muons per day crossing the detector. The readout sequence can also be activated by the outer detector by means of a suitable triggering system which fires when at least six PMTs detect light in a time windows of 150 ns.

The key requirement in the technology of Borexino is achieving extremely low radioactive contamination, at or below the interaction rate of 50 counts/(day·100ton) expected for solar ${}^7\text{Be}$ neutrinos. The design of Borexino is based on the principle of graded shielding, with the inner core scintillator at the centre of a set of concentric shells of increasing radiopurity. All components were screened and selected for low radioactivity [106], and the scintillator and the buffers were purified on site at the time of filling [107, 108]. Position reconstruction of the events, as obtained from the PMTs timing data via a time-of-flight algorithm, allows to fiducialize the active target: approximately 2/3 of the scintillator serves as an active shield. Assuming secular equilibrium in the Uranium and Thorium decay chains, the Bi-Po delayed coincidence rates in the fiducial volume of Borexino imply ${}^{238}\text{U}$ and ${}^{232}\text{Th}$ levels of $(1.67 \pm 0.06) \times 10^{-17} \text{ g/g}$ and, $(4.6 \pm 0.8) \times 10^{-18} \text{ g/g}$, respectively, 10 to 100 times lower than the original design goals of Borexino [25].

3.4 Scintillation light in Borexino

The choice of the scintillator mixture used in the Borexino detector was performed taking into account both its optical properties [109, 111] and the radiopurity constraints dictated by the experiment physics goals. The PC+PPO (1.5 g/l) solution adopted in Borexino as a liquid scintillator satisfies specific requirements: high scintillation yield, high light transparency, and fast decay time, all essential for good energy and spatial resolution and good discrimination between α and β events. This section is devoted to recall the physics of the scintillation in liquid organic compounds, and describe the characteristics of the scintillation light in Borexino.

It is known that in an organic scintillator the fluorescence is a property of a single molecule [115]. The carbon bond in aromatic molecules is made by electrons lying in the so called σ bond and π bond. The π electron energy levels are quantized in a series of singlet S_{ij} and triplet T_{ij} states where i denotes the electron energy levels and j denotes the vibrational sub-levels. The fluorescence light is emitted in radiative transitions from the first excited state S_1 to one of the vibrational sub-levels of the fundamental state.

Charged particle losing energy in the PC + PPO medium leads to the ionisation and excitation mostly of the PC molecules (the solvent) which are present in large quantities with respect to PPO one (the fluor). Several processes may happen ranging from the excitation of a π electron in a singlet S_{ij} state, or the ionisation of a π electron with possible subsequent recapture in a singlet or triplet excited state, excitation or ionisation of σ electrons. Direct transitions into a triplet state $S_{0j} \rightarrow T_{ij}$ are forbidden due to spin selection rules.

The PPO molecules get excited by radiative (emission of photons from the PC and absorption in PPO) or non radiative transfer processes (dipole-dipole interaction between excited PC molecules and a PPO molecule). For solute concentration like the ones in Borexino non radiative transfer should dominate. Again, fluorescence light can only be emitted by de-excitation of π electrons in PPO: the π electrons of in the S_{ij} states promptly reach (through non radiative processes) their first excited state S_{10} and the scintillation light is emitted in the transition between this first excited state toward one of the fundamental states S_{0j} . The radiative decay of the PPO excited molecules is responsible for the observed fluorescence, The emission spectrum of the Borexino scintillator mixture, with a peak at 360 nm match well the phototube peak efficiency [96].

The concentration of PPO in PC has been optimised to obtain the maximum *yield* (that is the maximum energy transfer from PC to PPO) and the fastest time response to allow the scintillation event position reconstruction, while minimising PPO self-absorption.

The PPO emission time is exponential with a time constant of 1.6 ns. By collision, excitation energy can be transferred to a triplet excitation state T_{10} . This triplet state has a lower energy than the singlet state. It is therefore impossible to return to the singlet state by non-radiative transition, but radiative transition are also forbidden by spin selection rules. The only way to de-excite is the interaction with another solvent molecule in the same triplet state. This phenomenon leads to the delayed fluorescence. The time distribution of the emitted fluorescence photons and the light yield depend on

the various molecular processes taking place as a consequence of the particle energy loss. Such phenomena do not simply depend on the total energy deposited in the scintillator, but mainly on how the energy is deposited, in particular on the value of the deposited energy per length dE/dx . This leads a dependence on the particle type: heavy ionizing particles like α particles have a large dE/dx which produces large ionization or excitation density, increasing the probability of transitions to triplet states and the emission of the delayed fluorescence. The difference in the amount of light emitted at longer times for α and β events is the basis of the α/β discrimination capability.

3.4.1 Ionization quenching for electrons, α , and γ -rays

The emission of scintillation light in an organic liquid scintillator deviate significantly from a simple linear relation on the particle energy loss. The scintillation yield strongly depends on the energy loss per unit of length (dE/dx): large dE/dx , produces large ionization (or excitation) density, which favour molecular processes where the energy is dissipated in non-radiative ways. The dissipation of the energy deposited in the scintillator in non-radiative ways is called *quenching* [115].

The total amount of light emitted by the scintillator by a charged particle that loses its kinetic energy E can be written as:

$$L = YEQ(E) , \quad (3.9)$$

where E is the initial kinetic energy of the charged particle, Y is a multiplicative parameter called *scintillator light yield*, and $Q(E) \leq 1$ is the *quenching factor*.

The energy loss of a charged particle is related to the particle type; heavy ionizing particles, like α particles, have large dE/dx . For this reason, the quenching factor $Q(E)$ for an α particle is larger with respect to a β particle with the same kinetic energy. The amount of scintillation light induced by a α decay is lower than the amount of light emitted by a β decay with the same energy.

Gamma rays can not directly excite the molecules of the scintillator. The interactions of γ -rays in the scintillator are observed by detecting the scintillation light emitted by the various electrons (and positrons) scattered (or produced) in the electromagnetic shower generated by the parent γ through photoelectric effect, Compton scattering, and pair production. Every electron deposits in the scintillator an amount of energy which is a fraction of the initial energy of the γ -ray. The amount of scintillation light generated by the γ -ray is then obtained summing over all the electron contributions:

$$L_\gamma = Y \sum_i E_i Q(E_i) . \quad (3.10)$$

The ionization quenching strongly influences the response of the scintillator to γ -rays. In particular, the amount of scintillation light induced by a γ -ray is lower than the amount emitted by an electron with the same energy.

Cherenkov light can also be produced in the scintillator if the electron velocity is high enough. The contribution of the Cherenkov light on the total light emitted depends on the energy of the electron (or the primary high energy γ -ray), and accounts for $\sim 10\%$ for a 1 MeV electron.

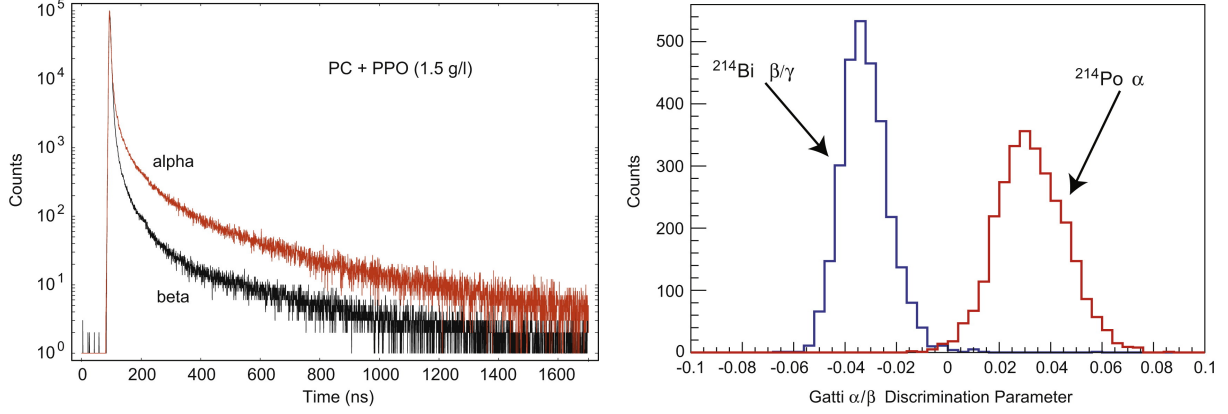


Figure 3.2: **Left panel** Time response of the Borexino scintillator mixture for α and β particles. **Right panel**: Gatti variable for ^{214}Bi (β) and ^{214}Po (α) events. The two components are clearly separated.

3.4.2 Time response and α/β discrimination

The time response of the PC + PPO mixture chosen for Borexino, measured for α and β particles on small sample of scintillator, is shown in Fig. 3.2 (left) and can be phenomenologically described by the sum of few exponentials having time constants τ_i :

$$S(t) = \sum_{i=1}^N \frac{q_i}{\tau_i} \exp\left(-\frac{t}{\tau_i}\right), \quad (3.11)$$

where $N = 4$ and q_i is the fraction of the light emitted following the time behaviour e^{-t/τ_i} . The first exponential (corresponding to the fastest time decay) accounts for the most of the emitted light ($\sim 90\%$ for β events and $\sim 65\%$ for α events). The difference in the scintillation emission times (*pulse shape*) for α and β particles, can be used to identify or discriminate which particle lead to the scintillation event (*particle identification via pulse shape discrimination*).

Several methods can be used to discriminate α and β events, leading to different pulse shape discrimination parameters [116]. One simple parameter, called *tail to total ratio* (or *tailtot ratio*), is simply the ratio between the number of photoelectron hits in the tail (i.e. after a particular time) and the total number of photoelectrons hits in the event.

A powerful method used in Borexino to discriminate α and β events is based on the *Gatti Optimal Filter* [117, 116]. For both α and β events, it is built a normalized reference shape that represent the probability distribution $P(t)$ for a photon to be emitted at a certain time t . The reference shapes are binned in time for ease of comparison with experimental data. If we denote the respective probability distributions as $P_\alpha(t)$ and $P_\beta(t)$ and the reference shapes as $r_\alpha[t]$ and $r_\beta[t]$ then we have:

$$r_\alpha[t] = \int_t^{t+\Delta t} P_\alpha(t) dt \quad (3.12)$$

$$\sum_{t=0}^{\infty} r_\alpha[t] = \int_0^{\infty} P_\alpha(t) dt = 1 \quad (3.13)$$

where Δt is the bin width. The same relations hold for $r_\beta[t]$ and $P_\beta(t)$.

The Gatti parameter for an event with a (binned and normalized) time profile $e[t]$ is then defined as:

$$g_e \equiv \sum_{t=0}^{\infty} e[t] \cdot w[t] \quad (3.14)$$

where

$$w[t] \equiv \frac{r_\alpha[t] - r_\beta[t]}{r_\alpha[t] + r_\beta[t]}. \quad (3.15)$$

For time bins where both reference shapes are zero, the weight $w[t]$ is set to zero. Fig. 3.2 (right) shows the Gatti variable for the α and β samples obtained from the $^{214}\text{Bi} - ^{214}\text{Po}$ fast coincidence decay. If an event with N photoelectrons is drawn from the α (β) probability distribution, then the corresponding Gatti parameter is also a probability distribution G_α (G_β). It can be shown that the mean and the variance of this distribution are

$$\overline{G_\alpha} = \sum_{t=0}^{\infty} r_\alpha[t] \cdot w[t], \quad (3.16)$$

$$\text{var}(G_\alpha) = \frac{1}{N} \sum_{t=0}^{\infty} r_\alpha[t] \cdot w^2[t] - (\overline{G_\alpha})^2, \quad (3.17)$$

and the same equations hold for events drawn from the β probability time distribution [117]. The absolute value for the means of the G_α and G_β distributions are the same (they differ in sign) and are independent of the number of photoelectrons N (i.e. on the energy of the event). These conditions are exactly true only if the event pulse shape is sampled for an infinite amount of time. For real data, sampled in a finite time window, the mean of the two distributions can be no longer equal in absolute value, and electronic dead times and dark noise may lead to an energy dependence. The variance of the distributions are different and get large for low N , resulting in a worse α/β discrimination power at lower energy. More details and informations on the Gatti parameter and its implementation and usage in Borexino can be found in the PhD thesis [118] and [119].

3.4.3 Positron interactions and discrimination

The time profile of the scintillation and the quenching for a positron event is different with respect an electron event of the same energy. After the positron deposits its kinetic energy in the scintillator, the positron will annihilate with an electron, emitting two back-to-back γ -rays. A slight difference in the time distribution of the scintillation signal arises from the time lag of few ns in the physical process of electron-positron annihilation as well as from the presence of annihilation γ -rays, which present a distributed, multi-site event topology and a larger average ionization density than electron interactions [120].

Prior to annihilation, the positron emitted in the ^{11}C decay may form a bound state with an electron in the scintillator, the positronium. The ground state of positronium has two possible configurations depending on the relative orientations of the spins of the electron and the positron: the spin singlet state ($S = 0$, $M_S = 0$), called para-positronium (p-Ps), with a mean life of 125 ps in vacuum, and the spin triplet state

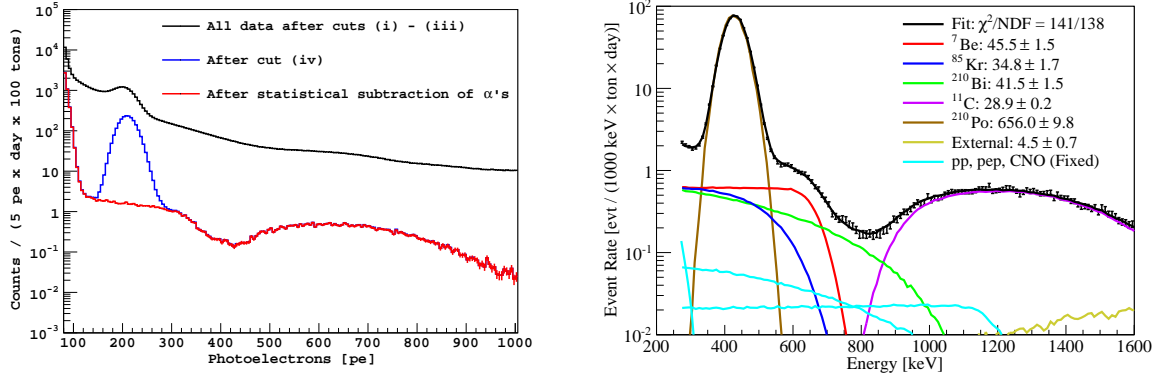


Figure 3.3: **Left:** The raw photoelectron charge spectrum after the basic cuts i-iii (black), after the fiducial volume cut i-iv (blue), and after the statistical subtraction of the α -emitting contaminants (red) (see Sec. 5.5.4). The description of the cuts is the following: (i) muons and all events within a time window of 300 ms after a muon are rejected, (ii) events with multiple time clusters within the same hardware data acquisition gate and events within 2 ms and 1.5 m of another event are rejected, (iii) noise and strange events are rejected, (iv) the reconstructed vertex is required to be within a 3.021 m fiducial radius and the vertex vertical distance from the detector centre is < 1.67 m. **Right:** A Monte Carlo based fit over the energy region 270-1600 keV; the event energies are estimated using the number of photons detected by the PMT array. Rate values in the legend are integrated over all energies and are quoted in units of counts/(day \cdot 100ton).

($S = 1$, $M_S = -1, 0, 1$), called ortho-positronium (o-Ps), with a mean lifetime in vacuum equal to 140 ns. In liquid scintillator, however, the lifetime of o-Ps is reduced because of interactions with the surrounding medium: processes like spin-flip, or pick-off annihilation on collision with an anti-parallel spin electron, lead to the two body decay with lifetimes of a few nanoseconds. Laboratory measurements of o-Ps properties common organic liquid scintillators leads to ~ 3 ns mean life and $\sim 50\%$ formation probability [121]. The delay introduced by the o-Ps lifetime is comparable to the faster scintillation time constant (~ 3 ns), and therefore is expected to introduce a distortion in the time distribution of hit PMTs with respect to a pure β^- event of the same reconstructed energy. Additional distortions are expected from the diffuse geometry of events resulting from the positronium decay, due to the non-null free mean path of the ensuing γ -rays.

More details on the β^+/β^- pulse shape discrimination performed in Borexino for the measurement of the *pep* neutrino interaction rate can be found in Sec. 5.7.

3.5 The Borexino energy spectrum

An offline reconstruction code is employed in Borexino to reconstruct the time, the energy, and the position of each recorded event. As a first step, the code identify in the recorded gate the *clusters*, groups of time-correlated PMT hits that belong to

a unique physical event. The number of PMT hits and the total charge (number of photoelectrons) of the cluster are used as estimators of the energy of the event (see Sec. 4.2.7 for a more detailed description of the energy estimators). The position is determined using a photon time of flight method. The understanding of the detector energy response function, and the accuracy and precision of the position reconstruction algorithm have been confirmed by means of an extensive calibration campaign using α , β , γ , and neutron sources deployed within the active target (see [25] and Sec. 4.3.1).

By measuring the position of each events, one can define a Fiducial Volume (FV) such that the residual external background due to the detector peripheral structures can be suppressed. Approximately 2/3 of the scintillator serves as an active shield (see Sec. 5.5.2). The time profile of the PMT hits of each cluster is also used to identify the event type. Particularly, muons crossing the buffer (if not already tagged by the outer detector), α particles, and β -like events can be discriminated by mean of the mean time of the cluster, or the ratio between the number of hits in the tail and the total number of hits (tail-to-total ratio), and of several $\alpha - \beta$ discriminating procedures like the Gatti optimal filter (see Sec. 3.4.2). Borexino has also some separation power to discriminate between β^+ decays and electron recoils (or β^- decays), mainly because of the finite lifetime of the ortho-positronium bound state in the liquid scintillator that delays a fraction of hits in β^+ events (see Sec. 3.4.3 and Sec. 5.7).

The observed energy spectrum based on 740.7 days of total life time before and after basic cuts is shown in Figure 3.3. The expected box-like spectrum of recoil electrons scattered by the 862 keV mono-energetic ^7Be neutrinos is apparent at 665 keV. All the end points of the reconstructed energy spectra are scaled to an higher energy, due to the effect of the energy resolution of the detector.

Prominent backgrounds are also apparent in the spectrum. Below ~ 250 keV the spectrum is dominated by ^{14}C decays (β^- , $Q = 156$ keV, half-life 5700 years) intrinsic to the scintillator [122]. Also the pileup of ^{14}C decays is contributing to the background in this energy region. The peak at ~ 440 keV is due to α decay of ^{210}Po (α , $Q = 5.41$ MeV, light yield quenched by ~ 13 , half-life 138 days), a daughter of ^{222}Rn out of secular equilibrium with the other isotopes in the sequence. The ^{85}Kr (β^- , $Q = 687$ keV, half-life 10.7 years) is a radioactive isotope found in the atmosphere and it is present in the data due to a small leak of air into the scintillator while filling the detector. The ^{210}Bi (β^- , $Q = 1.16$ MeV, half-life 120 hours) is a daughter of ^{210}Pb (β^- , $Q = 63$ keV, half-life 22.2 years), another daughter of ^{222}Rn out of secular equilibrium with the isotopes in the sequence. The continuous spectrum above 800 keV is the positron spectrum of cosmogenic ^{11}C (β^+ , $Q = 1.98$ MeV, half-life 20 minutes), produced *in situ* by muon interactions on ^{12}C in the scintillator [123]. External γ -ray background, mainly due to ^{208}Tl and ^{214}Bi decays in the detector peripheral structures, provides a small contribution above ~ 1.3 MeV.

^{85}Kr and ^{210}Bi decays are the main backgrounds in the energy region sensitive to the ^7Be solar neutrino interactions, while ^{210}Bi and ^{11}C decays are the main background in the energy region sensitive to the *pep* and CNO solar neutrino interactions (see also Table 3.1).

The study of fast coincidence decays of $^{214}\text{Bi} - ^{214}\text{Po}$ (from ^{238}U) and $^{212}\text{Bi} - ^{212}\text{Po}$ (from ^{232}Th) yields, under the assumption of secular equilibrium, concentration mea-

measurements of $(1.67 \pm 0.06) \times 10^{-17} \text{ g}(^{238}\text{U})/\text{g}$ and $(4.6 \pm 0.8) \times 10^{-17} \text{ g}(^{232}\text{Th})/\text{g}$ in the scintillator. The ^{85}Kr content in the scintillator is also probed through the rare decay sequence $^{85}\text{Kr} \rightarrow ^{85m}\text{Rb} + e^- + \bar{\nu}_e$, $^{85m}\text{Rb} \rightarrow ^{85}\text{Rb} + \gamma$ ($\tau = 1.5 \mu\text{s}$, BR 0.43%) that offers a delayed coincidence tag, and the resulting measurement for the activity of ^{85}Kr is $(30.4 \pm 5.3 \pm 1.3) \text{ counts}/(\text{day} \cdot 100\text{ton})$ [25, 77].

The basic analysis method used in Borexino to evaluate the solar neutrino signal rate is a fit to the energy spectrum. In such fits, the weight for the solar neutrino signal and the main radioactive background components are left as free parameter. This is usually done for energy spectra constructed from both the number of PMTs hit and the total collected charge in the event [25]. The *probability density functions* (pdfs), that are the energy reference spectra for the neutrino and radioactive background signals used in the fit, are generated with two independent methods, one which is Monte Carlo based and one which uses an analytic modelling of the detector response. Usually, the fit to the energy spectrum constructed from the number of PMTs hit is performed with the Monte Carlo based pdfs, while the fit to the energy spectrum constructed from the total charge is performed with the analytic based pdfs. Both methods benefit from an extensive campaign of detector calibrations. In order to perform precision measurement of the solar neutrino interaction rates, the modelling of the energy response function must be tuned with very high accuracy. The tuning of the Monte Carlo of the Borexino detector, using the detector calibration data, has been one of my commitments within the Borexino collaboration. A description of the Borexino Monte Carlo, highlighted on the tuning procedure and the accuracy obtained, is outlined in Chapter 4.

Although the simple fit to the energy spectrum has lead to the 5% precision measurement of the ^7Be solar neutrino interaction rate [25], this analysis technique alone is not sufficient to evidence the *pep* and CNO solar neutrino signals and measure their interaction rate, because of the high background rate due to the cosmogenic β^+ emitter ^{11}C . Novel analysis procedures to suppress the ^{11}C background have been developed and adopted for the *pep* and CNO solar neutrino analysis. Such techniques, whose development, application, and tuning have been part of my commitments within the Borexino collaboration, are described in Chapter 5.

Chapter 4

The Borexino detector response and simulation

4.1 Introduction

The physics program of the Borexino experiment, in particular the solar neutrino detection, calls for an accurate and complete understanding of the detector response. An high precision measurement of the ${}^7\text{Be}$ solar neutrino flux, a measurement of ${}^8\text{B}$ solar neutrinos with low energy threshold, a direct measurement of the rare signal from *pep* solar neutrinos, and strong limits of the CNO solar neutrino flux all require a strict control of detector stability, energy calibration, spatial reconstruction of the events, and pulse shape analysis.

This understanding was indeed achieved and implemented in a detailed full Monte Carlo simulation of the Borexino detector which now reproduces the data with accuracy of 1% or better for all quantities relevant for data analysis. In order to reach the understanding and modelling of the Borexino detector response with high accuracy, an extensive calibration of the detector with α , β , γ , and neutron sources deployed in the active target has been performed. Besides, a high activity ${}^{228}\text{Th}$ source was deployed in the outermost buffer region, outside the active volume [124, 125]. These calibration campaigns have been crucial to develop, debug, upgrade, and fine-tune the full Monte Carlo simulation chain of Borexino. In particular, the calibration data has been instrumental to validate the physics model used to describe the scintillation behaviour, the light propagation, and the detector response to the light signal.

The upgrading, debugging, and tuning of the Monte Carlo simulation code has been one of my commitments within the Borexino collaboration.

The full Monte Carlo simulation is extensively used in all the measurements in Borexino. For what concerns the *pep* and CNO solar neutrino measurement (see Chapter 5), the full Monte Carlo simulations have been used in particular for:

- generate the reference energy spectra for the neutrino signal and radioactive backgrounds used in the fits of the energy spectrum constructed from the numbers of PMTs hit (see Sec. 3.5 and Sec. 5.9.2.2);
- generate the reference energy spectra and the spatial distribution profile of the

external γ -ray background components (see Sec. 5.8);

- generate time profiles of the PMTs hit for electron and positron events to investigate the ortho-positronium formation in PC and study the feasibility of a $\beta^+-\beta^-$ pulse shape discrimination in Borexino (see Sec. 5.7);
- generate the reference profile for many of the pulse shape discrimination variables based on the Gatti method (see Sec. 3.4.2 and Sec. 5.7.3).

Other use of the Monte Carlo simulations include the search for the best compromise between ^{11}C rejection and fiducial exposure preservation in the TFC veto (see Sec. 5.5.3), the evaluation of the systematic uncertainties involved with the uncertainty in the energy response and in the position reconstruction (see Sec. 5.10.3), and the check of the reliability of the fit results and uncertainties with simulated event distributions (see Sec. 5.10.2).

The chapter is organised as follows. A description of the Borexino Monte Carlo chain and the physical models implemented therein are outlined in Sec. 4.2 of this chapter. In Sec. 4.3 I describe the tuning procedure used to tune the parameters of the energy and time response of the detector. The accuracy of the simulation is shown comparing real and simulated calibration data.

4.2 The Monte Carlo simulation and the physics modelling of Borexino detector

Particles depositing energy in the Borexino Inner Vessel or in the buffer regions produce scintillation and Cherenkov light which propagate inside the detector and eventually reach the PMTs, yielding a detectable signal.

For each event, the Borexino detector is measuring the number of photons detected by each PMT, the charge of each photon hit and the relative time among hits of different PMTs. The physical informations that can be extracted from the data are the amount of energy deposited in the scintillator (roughly proportional to the total number of collected hits or to the total integrated charge), the event position (making a time-of-flight fit to the time distribution of the hits), and, in some cases, the particle type, from a pulse shape analysis of the time scintillation signal pattern.

The accuracy in the modelling of the relation between the measured observables and the physical quantities relies on the understanding of all the physical processes governing the particle energy loss in the various materials, the scintillator light production, propagation and detection. Besides, it depends on the characteristics of the detector electronics and of the triggering system.

The Borexino full Monte Carlo simulation has been designed and optimised to fully model and reproduce all these processes up to the signal detection, providing simulated events in the very same format produced by real data acquisition. In this way, the event reconstruction and analysis can be used on both real and simulated data, and blind analysis is in principle possible.

The full Monte Carlo simulation chain consists of a set of numerical codes that

- generates the event (in particular, elastic scattering interactions based on the solar neutrino spectrum, radioactive decays, calibration source events, muons and cosmogenic production, antineutrino interactions);
- simulates the energy loss of each specific particle in every material present in the detector;
- generates the scintillation or Cherenkov photons from the particle energy loss in the media and the property of the scintillator and the buffer;
- tracks each single scintillation photon including its interaction with the scintillator and with the materials until a photomultiplier is reached or the photon is lost;
- generates the PMT pulse signal and the measured signals taking into account the specific design of the front end and digital electronics chains of Borexino;
- simulates the trigger response and produce the final output for triggering events;
- produces a set of data formally identical to the real raw data.

These simulated data are then decoded and reconstructed with the same offline code used for the real data.

The Borexino simulation chain is structured in three (or four) independent programs:

- GeNeb, an optional Fortran code for event generation and energy deposit.
- g4bx, a Geant4¹ based code for the event generation, energy loss, light generation and tracking.
- bx_elec, the electronics simulation code that simulates the trigger, the response of the electronics and produces an output in the same format of the raw data.
- Echidna, the offline reconstruction code, which can be used to reconstruct simulated data in the same way of real data.

4.2.1 The event generation

Several event generators have been built within the Borexino Monte Carlo simulation code, including generators for elastic scattering events of each solar neutrino component, radioactive decays (within the RDM module), calibrations sources, muons and cosmogenic production, neutrons, and antineutrino interactions.

¹Geant4 is a object oriented C++ toolkit for the simulation of the passage of particles through matter. The tools of the package permits to build an accurate modelling of the detector geometry and materials [126].

4.2.1.1 The solar neutrino generator

A special event generator that simulates elastic scattering interactions for each specie of solar neutrino has been developed in g4bx. The solar neutrino energy spectra are taken from the computation of John Bahcall and his collaborators [127]. The oscillation effects, which turns some ν_e into ν_μ or ν_τ are included. The electron neutrino survival probability (P_{ee}) is calculated in the framework of the LMA-MSW oscillations (see Sec. 2.7). The solar neutrino generator simulates the flavour conversion according to the energy of the neutrino and the oscillation parameters Δm_{sun}^2 and θ_{sun} given as input. The Sun matter effects are computed according to [128]. The kinetic energy of the electron recoils are randomly extracted according to Eq. 3.5.

4.2.1.2 The radioactive decay generators

Several radioactive decay generators are available in the Borexino Monte Carlo framework. One generator is implemented within the Fortran code GeNeb, originally developed at the beginning of the project and extensively used during the CTF runs in the '90s to prove the feasibility of the experiment. GeNeb can generate each radioactive chain and computes the energy deposit for α , β and γ particles in the scintillator using the EGS4 library.

In g4bx, the main radioactive decay generator is Radioactive Decay Module (RDM) implemented within Geant4. RDM and the associated classes are used to simulate the decay of radioactive nuclei by α , β^\pm and γ emission and by electron capture (EC). The simulation model is empirical and data-driven, and uses the Evaluated Nuclear Structure Data File (ENSDF, [129]). If the daughter of a nuclear decay is an excited isomer, its prompt de-excitation is treated.

Another radioactive decay generator in g4bx is the custom SCS generator, which is used to generate "by hand" the energy spectra of some nuclear decays. The SCS model is used to generate the spectral shapes which are wrongly implemented on RDM, or which have different references in literature, like ^{14}C or ^{210}Bi . More details on the GeNeb, RDM and SCS generators, as well as figures with energy spectra can be found in the Borexino internal note [130].

4.2.1.3 The positron generator

Special care was devoted to generate positrons interactions. As described in Section 3.4.3, in a fraction of the cases, positrons are captured by electrons before annihilation and form positronium [120]. The positronium may be created in the ortho-positronium (o-Ps) state, which has a mean life in the scintillator of ~ 3 ns [121], comparable to the faster scintillation constant. This effect delays the annihilation, the further energy deposit of the annihilation γ -rays, and the corresponding scintillation emission. o-Ps decays in 2 γ -rays because of the *peak off* effect.

The life time of ortho-positronium in PC+PPO mixture was measured in [121] and is ~ 3 ns while the ortho-positronium formation probability was found to be $\sim 50\%$. The o-Ps generation and the related delay in the annihilation γ -rays interactions have significant impact on the emission time of the detected scintillation light (pulse shape).

The difference in the pulse shape of an electron event with respect to a positron event has been used to discriminate β^- decay (or e^- recoils) from the ^{11}C β^+ decay (see Sec. 5.7).

A special event generator that simulates this effect has been developed. According to the input o-Positronium formation probability, the code generates positron annihilations and positronium decays. The latter process is simulated as a three-body vertex, composed by an electron, and two delayed annihilation gammas. The use of electrons instead of positrons is an approximation aimed to simplify the simulation, and motivated by the almost identical energy losses, with the exception of the annihilation process. The delay of the gamma generation is ruled by an exponential law depending on the o-Positronium mean life, given as input.

4.2.1.4 The calibration source generator

Great care was devoted to the simulation of the γ and neutron calibration source runs (see Sec. 4.3.1). The construction of the quartz vial and the water solution containing the radioactive source is included in the detector geometry and material construction. The calibration source is simulated in its real position, given as input. The decay of the radioactive source is simulated taking into account the correct branches of the decay.

4.2.2 The energy loss

The tools of the Geant4 package implemented within the Borexino Montecarlo Code allow to build an accurate modelling of the detector geometry and materials: the outer tank, Stainless Steel sphere, nylon vessels, photomultipliers and light cones, are constructed with real sizes and material compositions. Special tools have been added to take into account the real shape of the Inner Vessel and its time dependent deviations from a spherical shape.

The Geant4 libraries simulate the energy loss of each type of particle in every material of the detector (scintillator, quencher, water, nylon, aluminium, steel). The relative low energy of the typical events in Borexino make the tracking of each daughter (i.e. Compton electrons or e^+e^- pairs in γ -rays interactions) possible and preferable, allowing in principle high accuracy in the predictions. The standard Geant4 libraries are used for these processes. The stopping range of α particles is very short and can be neglected in the simulation, so the energy loss is effectively point-like.

4.2.3 The light generation

Two distinct physical processes generate light in the Borexino detector: the scintillation process and the Cherenkov process. The former is the dominating process, being the Cherenkov contribution at the level of $\sim 10\%$ for an electron of ~ 1 MeV. Within g4bx, special modules generate scintillation and Cherenkov optical photons according to the particle type and the deposited energy. A large part of the Monte Carlo tuning that we have performed is involving the scintillation photon yield, the quenching effect, and the time distribution of the emitted scintillation light.

4.2.3.1 Scintillation light

The amount and time distribution of the emitted scintillation photons depend on various molecular processes taking place as a consequence of the particle energy loss. The physics mechanisms involved in the scintillation process are outlined in Section 3.4, and more details can be found in the textbook [115].

The emission of light can not be simulated *ab initio* (i.e. at molecular level), because too many molecules and processes should be taken into account, resulting in an impractical simulation time. In the Borexino Monte Carlo, the emission of scintillation light is modelled in a semi-empirical way.

The mean number optical photons emitted in the scintillation process is first computed from the primary particle (e^- or α) energy loss, including the quenching effect. The scintillation model used in the Borexino Monte Carlo is the semi-empirical Birks model [115]. The Birks model relates the scintillation emission to the average ionization particle energy loss, dE/dx , and on the phenomenological *Birks parameter* k_B . The Birks parameter depends on the scintillator composition and properties, and on the length of the acquisition time. For most of the organic scintillators and setups, k_B is of the order of 10^{-2} cm/MeV, but its precise value cannot be predicted, and has to be determined experimentally. It is not still clear whether the Birks parameter have to be the same for different type of particles. In Borexino, we define a Birks parameter for each particle type, and we tuned it independently on the others. It turned out that Birks parameters for different particle type have very similar values. The Birks semi-empirical formula yields the scintillation light yield dL produced when a particle loses energy in a distance dx with the stopping power dE/dx :

$$\frac{dL}{dx} = \frac{L_0 dE/dx}{1 + k_B \cdot dE/dx} \quad (4.1)$$

The Birks parametrisation is a macroscopic description of quenching, and can not be used directly in a stochastic approach as in Monte Carlo simulations. In the Birks model, in fact, the quenching effect is obtained by comparing the initial energy of the primary particle with the energy deposited in the detector. In particular, all energy deposits due to secondaries produced by the primary particle (like δ -rays or X-rays) are assumed to belong to the primary. On the other side, in the Monte Carlo approach, each particle is treated independently. A correct parametrisation of the Birks formalism requires therefore to make the model compatible in a Geant4 framework, by evaluating the quenching factor for the primary ionizing particle, and inheriting the same factor to each daughter. The ingredients for this simulation approach are: an *a priori* parametrisation of the energy loss, required by the Birks equation, and a table of quenching factors as function of the energy, built at the initialisation phase, to speed up the simulation.

The mean number of emitted scintillation photons is obtained integrating Eq. 4.1 on the particle range:

$$L(E) = L_0 \int_0^E \frac{dE}{1 + k_B \cdot dE/dx} \quad (4.2)$$

One of the limiting case of Eq. 4.1 is $k_B \cdot dE/dx \ll 1$: in such cases, the light yield

$L(E)$ is approximately proportional to the particle energy loss ΔE :

$$L(E) \simeq L_0 \Delta E . \quad (4.3)$$

This is a relatively good approximation for electrons of few MeV.

When the denominator in Eq. 4.2 differ significantly from 1, the light yield is lower than in Eq. 4.3, yielding an intrinsic non linearity between the energy loss ΔE and the emitted scintillation $L(E)$. This non linearity has to be properly modelled and accounted in the data analysis. In the Birks model, the quenching factor $Q(E)$, that is the ratio between the true light yield and the one expected from the simple linear law 4.3, assume the form (see Eq. 3.9)

$$Q(E) = \frac{1}{E} \int_0^E \frac{dE}{1 + k_B dE/dx} \quad (4.4)$$

and it is always lower than one. The deviation of the measured light yield from Eq. 4.3 is increasingly important for protons, α particles, and nuclear fragments due to the high ionization per unit length. The quenching effect is also important for electrons and γ -rays with energy below few hundreds keV, as described in Sec. 3.4.1). The two parameters used to model the scintillation and the quenching L_0 and k_B are not known a priori, and are obtained by comparison between simulated data and the measured one (see Sec. 4.3.3)

For every electrons with energy E the mean number of scintillation photons to generate is computed in g4bx through Eq. 3.9 with $Q(E)$ given by Eq. 4.4 and obtained using the expression of dE/dx reported in [131] including the correction for positrons. The accuracy of dE/dx at very low energies (below and around 10 keV) is a subject of scientific debate still in progress [132].

The number of scintillation photon to generate is then randomly fluctuated according to the Poisson statistics. The wavelength of the each scintillation photon is generated according to the measured emission spectrum of the PC+PPO (1.5 g/l) scintillator mixture or PC+DMP buffer liquid [109]. The emission time of each scintillation photon is randomly generated according to the semi-phenomenologically response of the scintillator, Eq. 3.11, with different parameters for α and β particles (see Sec. 3.4.2 and Sec. 4.3.2).

4.2.3.2 Cherenkov light

Cherenkov photons are generated according to the Frank Tamm law in the wavelength range between 245 nm and 1800 nm. Ultraviolet Cherenkov photons that would not be directly detected by the photomultipliers are also generated and tracked: they can be absorbed by the PC or PPO and reemitted at higher wave length and thus they can originate detectable signals.

4.2.4 The light tracking

Each optical photon is individually tracked applying of all relevant physics processes (emission, absorption and re-emission, scattering on molecules, reflection on surfaces,

refraction between different media and absorption), allowing in principle high accuracy in the predictions.

Photon tracking takes into account the interactions of the emitted photons with each single component of the scintillator and or the buffer. These processes include elastic Rayleigh scattering of photons, absorption and re-emission of photons on PPO molecules, absorption of photons by DMP molecules and also photon absorption in thin nylon vessels. The cross-sections (or equivalently the wavelength dependent attenuation length $\Lambda(\lambda)$) for these interactions have been obtained from measurements of the extinction coefficient as a function of the wavelength [111] while the scintillator refraction index has been measured with a reflectometer.

In our model the light absorbed by PPO molecules is re-emitted with the probability $Q=0.82$ if the wavelength of the absorbed photon is lower than 375 nm and $Q=0.15$ for wavelength higher than 375 nm. We assume that the light is re-emitted in the IV with the PPO emission spectrum. The re-emitted photons are modelled with an isotropic distribution and emission mean time $\tau = 1.1$ ns.

Interaction of light with PC for $\lambda > 310$ nm is simulated as Rayleigh scattering with an angular distribution $P(\theta) = 1 + \cos^2(\theta)$, without time delay, and with no shift in the wavelengths of emitted photons. At shorter wavelengths the interaction with PC is simulated as attraction by PC molecules with the following energy transfer to PPO and re-emission by PPO with probability $Q=0.4$ and emission time $\tau = 2.7$ ns.

In buffer medium the light interacts with DMP molecules also as with the PC. The interaction with DMP leads to full photons absorption. Interaction with the PC is considered as Rayleigh scattering for $\lambda > 310$ nm. At shorter wavelengths the interaction with PC is simulated as attraction by PC molecules followed by re-emission with probability $Q=0.04$ with buffer scintillation spectrum and emission time $\tau = 2.8$ ns.

This light propagation model was already validated in CTF detector [111].

The Geant4 code optical photon simulation takes into account the Borexino detector optical surfaces and the processes of light reflection and refraction such as reflection of light from the PMT photocathodes, PMT aluminium light guides, stainless steel vessel, refraction of light on the borders of scintillator, nylon vessels and pseudocumene buffer. Finally photons are detected by PMT with a probability following the wavelength dependence of photomultipliers quantum efficiency.

4.2.5 Photomultipliers and light guides

A model for photomultiplier tubes (PMTs) is implemented in g4bx code to fasten the calculations: the segment of sphere with photocathode surface and the aluminium cylinder to model the PMT backup. All PMTs installed in the detector are build in the simulation in their exact positions. The optical photons are detected taking into account the measured wavelength dependences of PMT quantum efficiency and the relative PMT quantum efficiency of each PMT. The quantum efficiency of Borexino PMTs as a function of wavelength was measured with laser techniques [113] before PMT installation into Borexino and checked during detector operation period.

The polished aluminium lightguides [133] and the reflection of photons from the light guide surfaces also simulated.

For each photon detected (hit), the time of the hit and the PMT logical number are written to the output of g4bx. The PMT logical number describes the real logical electronics channel and PMT position in the detector. The simulation of PMT response to detected photons is done in bx_elec, the electronics part of the Borexino MonteCarlo simulation code.

4.2.6 The electronic simulation

The Geant4 code g4bx produces an output with the list of photons that gave a signal in a PMT, and the list of the hit times. Another C++ program, bx_elec, simulates the electronics chain and the triggering system, producing as an output a file formally identical to real data for all events that met the trigger conditions. The description of bx_elec is outlined of this section.

The electronics simulation program first includes the effect of the PMT transit time spread (approximately a gaussian with $\sigma \sim 1$ ns and a second peak at 60 ns) and includes the after-pulse signal with a fixed probability of 2.5%. The after-pulse signal was measured for all PMTs in a dark-room before installation in Borexino. Then, the hits due to PMT dark noise are using an average value equal to the measured one in the real data run. The typical dark noise rate is below 1 kHz for most of the PMTs. In the real detector, all PMTs are carefully aligned in time by means of a laser pulse that is synchronously delivered to each photocathode. This laser pulse is fired every 0.5 ns in all runs, so that alignment can be continually monitored. The accuracy of the alignment is better than PMT time jitter, so no other effect must be included in the simulation.

Then the code simulates the response of the electronics chain. Borexino electronics is made by an analogue front end and a digital board which works both as a TDC and as an ADC [96].

The analogue board provides two signals: a linear amplification of the PMT signal, and a gate-less integrated signal. The first linear signal is discriminated by the digital board to measure the time of the pulse (with 0.5 ns resolution), while the integrated signal is sampled by the ADC to measure the charge of each pulse. The integrator circuit is such that the signal is almost constant for 80 ns after the pulse, and then decays with a time constant of 500 ns because of the AC coupling between PMT and front-end. In order to minimise the noise in the charge measurement, when the linear signal goes above the discriminator threshold, the integrated signal is sampled twice with an 8-bit ADC, once before the signal rise and a second time after 80 ns. The real charge is proportional to the difference of these two ADC values. After each hit the digital board is dead for approximately 140 ns. This means that when two hits closer than 140 ns hit the same PMT, the second hit is lost for the time information. If the time difference is less than 80 ns the charge measurement of the detected hit will be doubled, while in the interval between 80 and 140 ns the second hit is completely lost. Although the frequency of multiple hits in the same PMT is rather small, especially at low energy, this effect must be accurately simulated to reproduce the energy response of the detector. The frequency of double hits depends on the event position (if the scintillation event is close to a group of PMTs, these see more light and the frequency

is higher) and on the energy, introducing a small non linearity and non uniformity that must be included in the analysis.

The electronics simulation code generates the charge associated to the pulse using an exponential plus a gaussian distribution to reproduce the single photoelectron response of the PMTs. The specific parameters for each PMT and the weight of the two contributions (different in the case of dark noise events and real scintillation events) have been obtained from the analysis of the real data. Then a PMT pulse with that charge is generated using a trapezoidal shape to approximate the rise and fall time of the signal, and the crossing of the discriminator threshold is simulated.

The program handles the front end behaviour properly summing the charge of the pulse produced on the same PMT within the 80 ns integration time; it takes also into account "the pileup effect" of the integrator output, i.e. the fact that a pulse detected on a given channel produces a raise of the integrator baseline and a following exponential decay that influences the measurement of the charge of the following pulses. The 140 ns dead time is of course included in the simulation.

A physical trigger in Borexino and in the Monte Carlo happens when N_{Thr} hits are detected within a time window Δt . Typically $N_{\text{Thr}}=25$ and $\Delta t=100$ ns. The Monte Carlo reproduces also the time structure of the acquired data which is due to details of the design of the digital board. In fact when the trigger is generated all the hits happening in a time window (acquisition gate) having typically 16 μs of duration are acquired. This is a time about 10 times longer than the maximum expected duration of a single physical scintillation event. The acquisition gate contains the true scintillation event and several dark noise hits happening before and after the trigger. Multiple scintillation events due to fast radioactive decays may produce events with hits in the same gate and this effect is properly simulated in the Monte Carlo. Additional informations present in the real data like the generation of the GPS time are also included in the code.

Finally, the code is also capable of including the effect of noisy and bad channels. During normal data taking, a dedicated program makes a complete check of the electronics during the run, and store into a data base the list of dead or noisy channels. The electronics simulation program reads this data base and can therefore simulate a run in the same running condition. This is particularly important to correct for detector instabilities. All simulations used for physics analysis are therefore done simulating the real Borexino detector, and not the ideal one.

4.2.7 The reconstruction program

The principal features of the Borexino reconstruction program (Echidna, and the additional high level reconstruction step MOE) are outlined in Sec. 3.5.

Three basic energy estimators are available (both in the data and in the Monte Carlo):

- npmts: the number of PMTs having at least one hit.
- nhits: the number of hits detected by the electronics. Multiple hits on the same PMT are included if their time distance is higher than 140 ns.

- charge (npe): the sum of the charge of signal of every PMT as measured by the digital boards (taking into account the 80 ns integration time and dead time) and normalized, for each PMT, to the peak position of each single photoelectron response.

These three basic energy estimator can then be implemented in several ways, depending on the considered length of the cluster (either fixed or variable), the presence of additional dead time after the 140 ns to remove spurious hit due to re-triggering, and the application of the subtraction of the expected dark noise hits.

The variables used in the *pep* ν and CNO ν s analysis are described in Sec. 5.6.

4.3 The tuning of the Borexino Monte Carlo

The simulation of the scintillation and the optical process requires a large number of parameters to be fixed and given as input to the Monte Carlo code. Such parameters determine the way physical and electronics processes take place in the simulation, and in the end, they are responsible of the output of the simulation, such as the time distribution of hit PMTs and the total number of hit PMTs. The understanding of such processes and the tuning of the corresponding models and parameters in the simulation leads to the understanding of the detector energy and time response, allowing high precision measurements, like the ^7Be solar neutrino flux [25], and measurements of rare signals, like the *pep* and CNO solar neutrino interactions (see chapter 5).

In order to reach the understanding and modelling of the Borexino detector response with high accuracy, an extensive calibration of the detector with α , β , γ , and neutron sources deployed in the scintillator active target has been performed after one year and a half of data taking (see Sec. 4.3.1 and the PhD thesis [134] for more details). The set of calibration campaigns, which I participated, have been completed in November 2008, January 2009, and June and July 2009. Besides, a high activity ^{228}Th source was deployed in July 2010 in the outermost buffer region, outside the active volume [124, 125].

The goal of the Borexino calibration campaigns was in particular to:

- Measure the accuracy of the event position reconstruction for events generated in the whole vessel and in the energy range from about $E_{min} \simeq 100$ keV up to $E_{max} \simeq 7$ MeV.
- Measure the resolution of the event position reconstruction as a function of the event position and energy.
- Calibrate the absolute energy scale from ~ 100 keV to ~ 7 MeV, with particular emphasis in the ^7Be ν and *pep* ν energy region, i.e. ~ 200 keV up to ~ 2 MeV.
- Measure the energy resolution.
- Measure the non-uniformity of the energy response as a function of the event position and of the energy.

- Check the effect of the external background.

The accuracy of the event position reconstruction is important for all solar neutrino measurements. The real neutrino target is a fiducial volume (FV) defined by software cuts on the reconstructed event position (see Sec. 5.5.2). A bias or a non uniform response in energy or position can bias the measured spectrum and lead to the systematic errors.

Spectral distortions due to non-linearity or position dependence of the energy resolution (see Sec. 5.5.2.2) are also crucial, and the absolute energy calibration is particularly important to disentangle the ${}^7\text{Be}$ ν signal from the ${}^{85}\text{Kr}$ background and the *pep* ν signal from the ${}^{210}\text{Bi}$ background.

Finally, the external background, is a non negligible contribution in the energy region above one MeV and is therefore important for the *pep* CNO and ${}^8\text{B}$ neutrinos. A precise knowledge and understanding of this background is mandatory in order to use a larger fiducial volume (see Sec. 5.5.2 and Sec. 5.8).

The calibration campaign of Borexino provided a clean sample of data that has been used to check the accuracy of the results of Borexino Monte Carlo code and to precisely tune the values of the relevant parameter in the simulation of the physics and electronics process. The parameters that have been optimised are:

- The absolute scintillator photon yield L_0 (see Sec. 3.4). This is expected to be in the range $\sim 10^4$ photons/MeV but its precise value has to be experimentally determined.
- The k_B quenching factor for β , α and protons (see Sec. 3.4.1).
- The values of the scintillation parameters that describe its time response τ_i and q_i (see Sec. 3.4.2 and Eq. 3.11).
- The reflection probability of the sphere and of the surface of the concentrators.
- The PPO re-emission probability.
- A scaling factor for the PPO and PC attenuation lengths.
- The after-pulse probability (see Sec. 4.2.6).
- A global scale factor in the PMT gain (see Sec. 4.2.6).

Optimising the simulation of the time response and light output means defining the set of values of the scintillation and optical parameter that gives the best accordance with calibration source data. The time response and light output cannot be tuned independently because almost all of the listed parameters influence the energy estimators. We have used an iterative and recursive approach in which the agreement between the simulated and measured time curves is searched with fixed light yield and k_B and then these parameters are optimised again.

Isotope	Type	Energy (keV)	activity (Bq)
^{57}Co	γ	122	3.45 ± 0.07
^{139}Ce	γ	165	3.12 ± 0.04
^{203}Hg	γ	279	2.78 ± 0.06
^{85}Sr	γ	514	-
^{54}Mn	γ	834	-
^{65}Zn	γ	1115	-
^{60}Co	γ	1173 - 1332	-
^{40}K	γ	1460	-
^{222}Rn	α β	0-3200	-
^{14}C	β	0-156	-
^{241}Am - ^9Be	neutrons	2223 (H) - 4946 (^{12}C)	-

Table 4.1: Calibrations sources. In the ^{85}Am - ^9Be source row, the quoted energy is the one of the capture γ -ray on the isotope in brackets.

4.3.1 The calibration data

Several radioactive sources have been deployed within the Inner Vessel (IV) by means of a carefully designed insertion system [134]. The sources were selected in order to study the detector response in the energy region between 122 keV and 7 MeV with α , β , γ and neutrons. Table 4.1 shows the main parameters of the sources used. The characterisation of the detector cover both the energy range for solar neutrino spectroscopy and the whole fiducial volume.

Despite of the relatively large detector mass, the interaction rate for solar neutrinos in Borexino is of the order of a few tens of counts/(day·100ton) or even less than one counts/(day·100ton), depending on the solar neutrino component (see Sec. 3.2 and Table 3.1). The low signal rate set very strong requirements on the background induced the radio-purity of all materials that have to be inserted in the detector itself. Particular care has been therefore devoted to the preparation and handling of the calibration sources and of the related insertion system as described in the PhD thesis [134] to ensure that the radio-purity reached by Borexino [25, 77, 78] is not spoilt by the calibration procedure.

In order to calibrate the detector without introducing unwanted contaminations, the source containers have been carefully designed. We have used a quartz sphere (one inch diameter) either filled by ^{222}Rn loaded scintillator identical to the Borexino or filled with γ emitters in aqueous solution. The quartz sphere were attached to a set of stainless steel bars that allowed to locate the source in almost any position within the IV (see the PhD thesis [134]).

A special procedure was developed to minimise the quenching of the scintillation light by oxygen. The comparison of the ^{210}Po peak due to source events with the one due to real $^{214}\text{BiPo}$ coincidence in the detector shows that the result was quite good and that the light quenching in the source was small.

The β and α events from the ^{222}Rn source have been used to study the accuracy of

the position reconstruction and the uniformity of the energy response as a function of the event position. The γ lines have provided the absolute energy scale along the whole region of interest.

In addition we have used a commercial ^{85}Am – ^9Be neutron source. The α decay of ^{241}Am produces a 59.5 keV x-ray with a 36% branching ratio. Because of this x-ray activity (about 180 kBq), too high for the data acquisition system, it was necessary to shield the source. To avoid any contact between lead and the scintillator, a special holder was fabricated: the body is white delrin, and the lead shielding is epoxied into the interior faces of the holder; stainless steel hardware and a Viton o-ring seal the holder to avoid any contact between the scintillator and the source itself.

The sources have been deployed along the vertical z axis of the inner vessel and in several position off axis. An optical system made by a led mounted on the source support and a series of camera allows to know the position of the source in the inner vessel with 2 cm accuracy. For more details about the sources, the deployment system and the location of the sources with the cameras see the PhD thesis [134].

4.3.2 Tuning of the time response

The time distribution of hits is involved in the reconstruction of the main features of the event: the clustering and the total number of hits in the event, the position reconstruction, the particle identification using pulse shape discrimination algorithms (see Sec. 3.4.2 and Sec. 3.5). In order to be able to simulated these high-level features, the time distribution of the hit PMTs (henceforth time distributions) must be simulated with at least 5% agreement with data, for each time bin and in the energy range used in the analysis. In particular, the mean and the peak of the time distribution should be reproduced with 1 ns accuracy, and the other momenta of the distribution should not disagree more then few nanosecond.

The parameters that influences the most the time distribution are: the scintillation parameters (τ_i , q_i), the PPO re-emission probability, the scaling factors for the PPO and PC attenuation lengths, the reflection probability of the SSS, concentrators and PMT cathode. The Scintillation light parameters (τ_i , q_i) are the one with the largest impact on the shape of the time distribution: they affect the profile from the first nanoseconds to tail of the distribution. PC and PPO scaling factors and attenuation lengths and PPO re-emission probability affects the rise of the time distribution and the width of its peak. They are also responsible for the uniformity of the energy response respect to the position of the event. The reflection probability of the source of the SSS, of the PMT concentrators and of PMT cathode affects the time distribution with a secondary structure of hits at 50-70 ns. For what concerns the simulation of the PMTS and the electronics (see Sec. 4.2.6), the parameters that affects the time distribution are the PMT transition time spread and the PMT afterpulse probability and its time distribution. Both of them have been measured and included in the simulation. The transition time spread affects the rise time of the distribution and the width of its peak, and it is responsible of a secondary bump at ~ 60 ns after the peak. The PMT afterpulse affects the time distribution with secondary hits from 140 ns to the end of the pulse.

Most of these parameters, with the exception of the τ_i and q_i for α events, have been fine-tuned using the following γ -ray source runs as reference: ^{85}Sr in 8 positions, ^{54}Mn , ^{65}Zn and ^{40}K at centre and at $z = \pm 3\text{m}$. The use of calibration data provides a set of advantages: calibration source runs ensure high statistics samples of pure and monochromatic and point-like events, allowing to study the dependence of the accuracy of the simulation of the time distribution with respect to the energy and position of the event. The ensemble of this source scans the relevant energy and position range for ^7Be ν analysis. The γ -ray sources have been employed to optimise the simulation of the time distribution of β events because the time distributions of β and γ events are very similar. In fact, γ -rays undergo Compton scattering on the electrons of the scintillator. Recoil electrons loose energy and produce scintillation light. Hence, the γ -ray is detected as superpositions of electron events of lower energy, close in space and time. Once the whole set of parameters have been tuned for β events, the α decay times and weights have been tuned using ^{214}Po events in ^{222}Rn sources.

The following iterative procedure has been followed. From a given calibration data run, the time distribution is built. The events coming from the calibration source are selected cutting events reconstructed outside a sphere of 1 m from the nominal source position. Only events with reconstructed energy around the nominal energy on the source are considered. Muons events and muon daughters are rejected using the external muon veto and the standard analysis cuts (see [105] and Sec. 5.5.1).

The very same calibration run is then simulated (see Sec. 4.2.1.4) with a given set of optical parameters. Great care was devoted to simulate the electronics configuration in the same configuration of the real run. In particular we have included the pattern the PMTs that were disabled during the run, the measured dark noise of the PMTs, based to the rate of random triggers during that run, the gain of each PMT, taken from to the electronics calibrations of the real run. The procedure of event selection described in the previous paragraph is performed on the simulated events. The time distributions of the selected simulated events are then compared to the corresponding distribution for real data events. For sources located at $z = \pm 3$ m from the centre of the detector, the time distributions are also compared using only the time distribution of hits in a subset of PMTs near or far from the source.

The optical parameters that leads to the best accordance between simulated and real time distributions are then selected. The comparison is done with the method of the least squares. Direct comparison using the eyes (that are the best tool of pattern recognition at present time) is also performed to select the final choice of configuration parameters.

A final overall check for β and α time distributions is done using the sample given by the $^{214}\text{BiPo}$ coincidences on normal runs (see Sec. 3.5). These events are distributed in the whole volume of the Inner Vessel. This allow to check the goodness of the simulation on the overall fiducial volume, instead of a point-like source. The inhomogeneity of the position of $^{214}\text{BiPo}$ events along the vertical axis is taken in account with the method of rejection.

4.3.3 Tuning of the energy response

The physics goals of the Borexino experiment (see Chapter 3) require to simulate the energy estimators with $\sim 1\%$ accuracy in the energy range 100 keV – 2 MeV relevant for the ${}^7\text{Be}$ ν analysis [25] and with a similar accuracy in the energy range 200 keV – 2.6 MeV used in the *pep* ν analysis (see Chapter 5).

The tuning of the energy response is performed defining the photon yield L_0 and the Birks quenching parameter k_B in the simulation that gives the best accordance with data. For a given energy estimator (see Sec. 4.2.7), the ratio between the position of the energy spectrum peaks of events with different energy is mostly related to the quenching factor k_B , while the absolute energy scale is determined by L_0 . Being none of the energy estimators described in exactly linearly related to the energy and to L_0 , then no rescaling of the simulation results is applied: we aim to reproduce the absolute values of the energy estimators with given L_0 and k_B .

The reproduction of the energy estimator npmts is related to the accuracy of the models of the energy loss, light generation and interaction in the media. The energy estimator nhits depends also on the accuracy of the electronics simulation (see Sec. 4.2.6), mostly because of the electronics dead time and the afterpulse. The charge (npe) energy estimator is also related to the accuracy of the simulation of the shape of the photomultiplier pulses and of the single photoelectron charge spectrum of each photomultiplier.

The tuning of the simulation of energy response is performed as follows. As a first step, we tune the photon yield L_0 and the Birks parameter k_B with calibration sources located in the centre of the detector (see Sec. 4.3.3.1). The tuning of the photon yield and the Birks parameter is performed mainly using the npmts and nhits energy estimator. The adjustment of the nhits and charge simulation, if needed, is obtained by tuning the parameters of the electronics code bx_elec (see Sec. 4.3.3.2). A comparison with ${}^{11}\text{C}$ spectrum (tagged with the TFC method, see Sec. 5.5.3) is performed in order to understand the agreement of the simulation the whole fiducial volume (FV). If needed, an effective L_0 for the simulation of the events in the FV is defined.

4.3.3.1 Tuning of the quenching for e^- and γ -rays

The calibration sources used for the tuning of the energy response in the centre of the detector are the γ emitter isotopes: ${}^{57}\text{Co}$, ${}^{139}\text{Ce}$, ${}^{203}\text{Hg}$, ${}^{85}\text{Sr}$, ${}^{54}\text{Mn}$, ${}^{65}\text{Zn}$, ${}^{60}\text{Co}$ and ${}^{40}\text{K}$. Such sources allow the tuning of the simulation of the energy response for e^\pm and γ events in the energy range between ~ 60 keV and ~ 2.4 MeV. Because of the quenching effect (see Sec. 3.4.1), the amount of light induced by a γ -ray is lower than the light emitted by an electron of the same energy.

The cuts to select the γ -rays emitted by the calibration source in the centre of the detector are the same described in Sec. 4.3.2. However, the energy of ${}^{57}\text{Co}$, ${}^{139}\text{Ce}$, and ${}^{203}\text{Hg}$ γ -rays lies below the high-rate ${}^{14}\text{C}$ decay end point, and the position cut is not sufficient to remove ${}^{14}\text{C}$ events. In order to obtain a clean spectrum of γ -ray events for these source runs, a subtraction of background events must be done. A bin per bin subtraction of the average energy spectrum of the two normal runs just before and after the calibration run is performed. This procedure allows to remove the ${}^{14}\text{C}$ and ${}^{210}\text{Po}$ decay contamination in the calibration source γ -ray event sample with high accuracy.

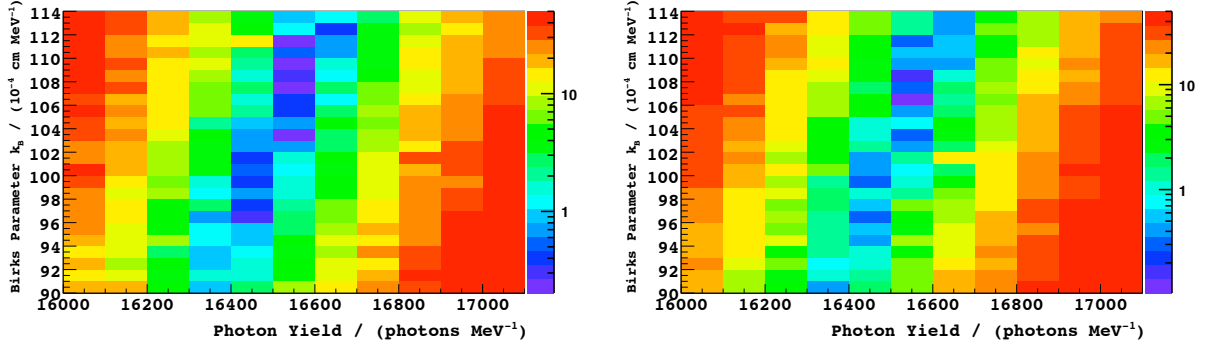


Figure 4.1: Distribution of the estimator of the goodness of the simulation of the energy response (Eq. 4.5) for γ -ray sources in the centre of the detector, as a function of the photon yield L_0 and Birks parameter k_B . **Left panel:** For the npmts energy estimator. **Right panel:** For the nhits energy estimator.

The very same calibration runs are then simulated (see Sec. 4.2.1.4) with a given (L_0, k_B) pair. The agreement between data and simulation is defined by the comparison of the reconstructed energy peak of each γ source. We fit the γ -peaks either with a Gaussian or a generalised gamma distribution [135] plus a 2nd-order polynomial (to model irreducible background) in order to find the mean value and the resolution of the energy estimator at the energy of the given γ -ray. We have defined an estimator of the goodness of the energy simulation as:

$$\frac{1}{N} \sum_{sources} \frac{(\mu^{data} - \mu^{MC})^2}{1 + e_{\mu^{data}}^2 + e_{\mu^{MC}}^2} \quad (4.5)$$

where μ is the mean value given by the fit (*i.e.* the peak position of the γ -peak in the energy spectrum) and e_{μ} is its error, and the sum is extended to the total number of considered calibration sources (N). The (L_0, k_B) pairs that give the best accordance are defined looking for the minimum value of 4.5 in the bidimensional parameter space of L_0 and k_B . The distribution of the estimator of the goodness of the simulation, for the last version of the Borexino simulation code, is shown in Fig. 4.1. Once a small subsample of good L_0 and k_B pairs are found, we perform χ^2 tests of the γ -ray energy spectra between data and simulation in order to define the (L_0, k_B) that gives the best accordance. The energy spectrum of the calibration γ -ray sources in the centre of the detector, for real and simulated calibration data is shown in Fig. 4.2.

The Birks quenching parameter k_B is then selected and fixed in the next step of the energy tuning, while the photon yield L_0 is allowed to be scaled by a small factor in order to correct volume effects, if needed.

4.3.3.2 Tuning of the electronics simulation parameters

The procedure outlined in Sec. 4.3.3.1 is performed on each energy estimator (npmts, nhits and charge, see Sec. 4.2.7). We tune the electronics simulation code (see Sec. 4.2.6)

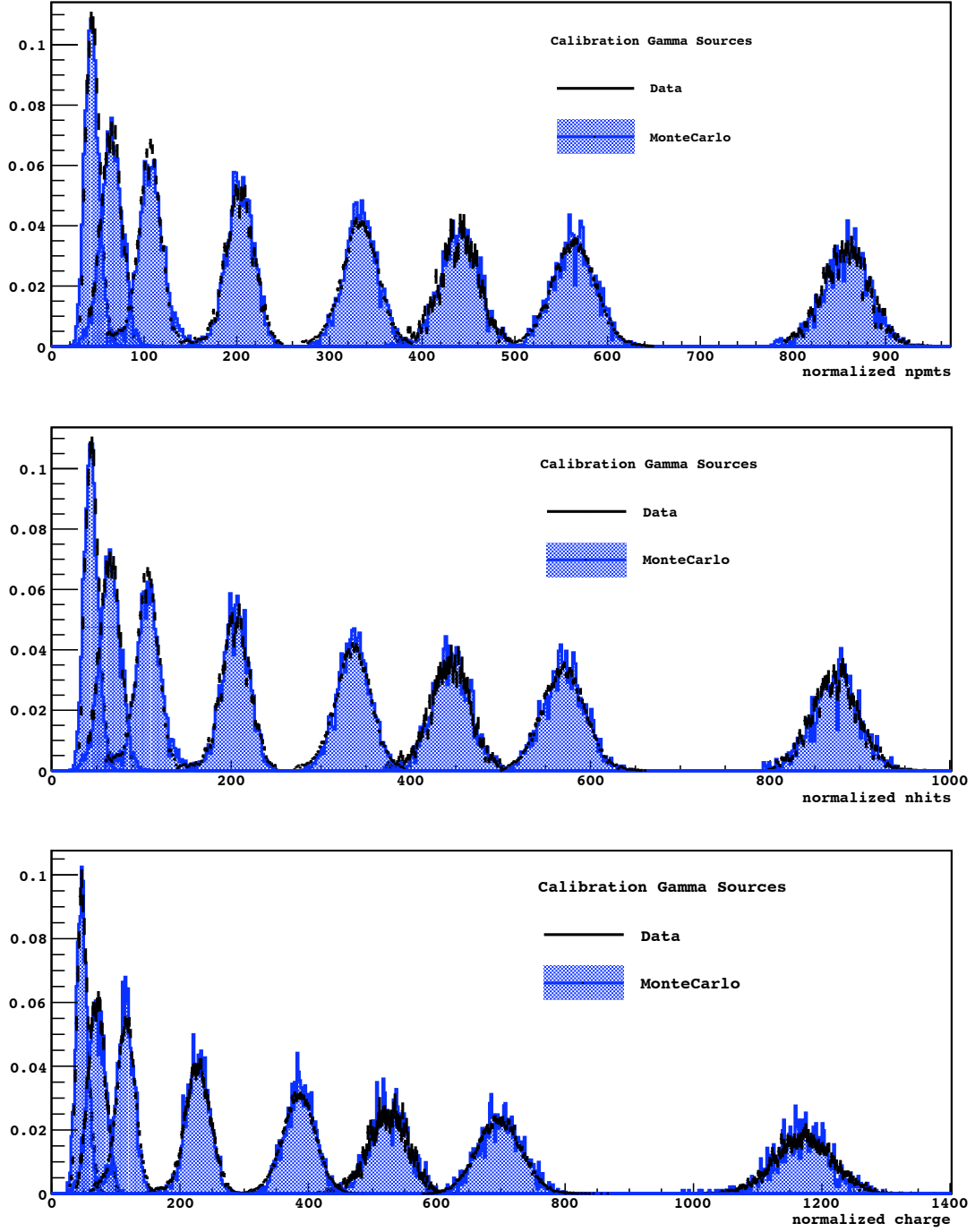


Figure 4.2: Energy spectrum of the calibration γ -ray sources in the centre of the detector, in real and simulated calibration data. From left to right the peaks represent the γ -decays of ^{57}Co , ^{139}Ce , ^{203}Hg , ^{85}Sr , ^{54}Mn , ^{65}Zn , ^{40}K and ^{60}Co (see Table 4.1 for the energy of the γ -rays). **Top panel:** The energy is evaluated with the npmts energy estimator. **Central panel:** The energy is evaluated with the nhits energy estimator. **Bottom panel:** The energy is evaluated with the charge energy estimator.

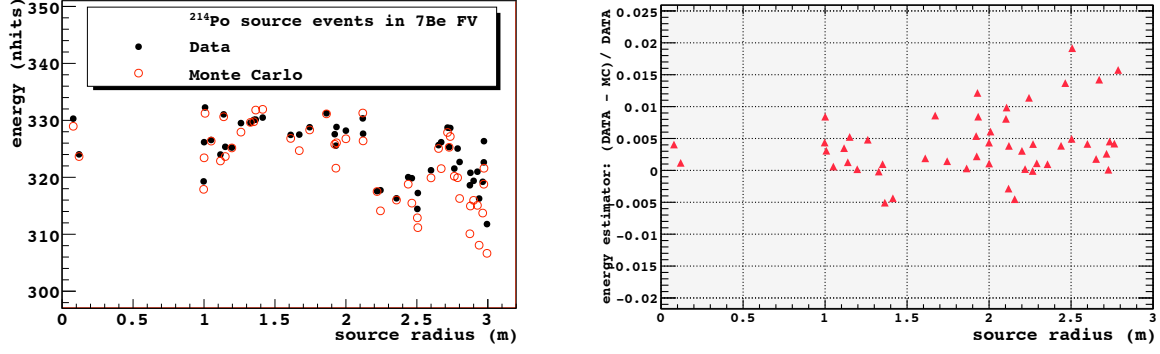


Figure 4.3: **Left panel:** Distribution of energy peaks of the ^{214}Po α decay as a function of the radial position of the events (in meters). ^{214}Po decay events have been obtained from calibration ^{222}Rn source runs. Black dots represent data, red circles represent the Monte Carlo simulation of the same calibration run. The Monte Carlo reproduces the trend. **Right panel:** This plot shows the relative difference of the ^{214}Po decay peaks in data and Monte Carlo in the Fiducial Volume used for the *pep* ν analysis (see Sec. 5.5.2) as a function of the radial position of the event. The relative difference is defined as $(\mu^{\text{data}} - \mu^{\text{MC}})/\mu^{\text{data}}$, where μ is the peak position of the α energy spectrum in the nhits energy estimator. The agreement is quite good: for most of the positions the relative difference is between -0.5% and +1.0%.

in order to ensure that the (L_0, k_B) pair that give the best agreement between data and simulations does not depend on the energy estimator.

The ratio between nhits and npmts is affected mainly by the afterpulse probability. The afterpulse probability is then tuned to get the nhits/npmts ratio in the simulation as the one in real data. Such tuning of the afterpulse probability also improving the simulation of the time distributions after ~ 140 ns since the start of the cluster (see Sec. 4.3.2).

The ratio between charge and nhits (or npmts) depends on the single photoelectron (spe) response of each PMT, that is mainly driven by the gain of the PMT. The spe parameters for each PMT of the detector are obtained from the real data on a run by run basis [96]. Those parameters are used as inputs in the simulation of the spe response in the Monte Carlo. However, a small global rescaling (at $\sim 1\%$ level) of the gain of the PMTs is often needed to tune the charge energy estimator, and in particular the charge/nhits ratio.

Once the afterpulse probability and the PMT gain scale factor are tuned, the best (L_0, k_B) pair does not depend on the choice of the energy estimator.

4.3.3.3 The energy response in the Fiducial Volume

Once the quenching Birks parameter has been tuned and the simulated spectra of the calibration γ -ray sources in the centre of the detector agrees with data, it is time to check the simulation of the energy response in the Fiducial Volume (FV). The light propagation in the Borexino detector is affected by many physical processes, such as

absorption (and re-emission) on PPO molecules, scattering on molecules, refraction and reflection at the interfaces between different media (such as PMT cathode and aluminium light guides), as described in Sec. 3.3 and Sec. 4.2. The parameters governing such processes have to be tuned in order to simulate correctly the light propagation and thus the dependence of the energy response on the position of the event.

Such part of the tuning is the hardest one. The number of parameters is very large and does not allow a wide scan in the full physical range of all the parameters simultaneously, like in the case of the (L_0, k_B) pair (see Sec. 4.3.3.1). Also, a small change in some of the parameters (such absorption mean free path, re-emission probability, or reflectivity at the SSS surface) has a huge impact on the time distributions (see Sec. 4.3.2) and the energy scale in the centre of the detector. The number of events to simulate is also very large, because in order to tune the trend of the detector response as function of the position, a large number of source runs at different positions need to be simulated. The irreducible asymmetries of the detector, like the anisotropy of the position of broken PMTs (which are mostly distributed in the south hemisphere of the Borexino detector) make the understanding and the tuning of the energy response as a function of the position even harder.

A physical quantity that is very useful in order to understand and tune the effect of the mentioned parameters is the ratio between “far” and “near” PMT hits with respect to the position of the source, because such ratio it is almost independent on the absolute energy scale. Also the ratio between hits on PMTs with and without light concentrators is a useful parameter.

The most useful calibration sources to understand the trend of the energy response as a function of position are the ^{222}Rn sources. Such calibration sources have been deployed in ~ 150 points at different position of the detector, and allow to select a pure sample of ^{214}Po α decay events based on the $^{214}\text{BiPo}$ fast coincidence and the Gatti parameter (see Sec. 3.4.2). The energy of the ^{214}Po events (using the nhits energy estimator) as a function of energy, for real and simulated calibration source runs, is shown in Fig. 4.3 (left). The agreement between data and simulation is quite good: for most of the positions in the FV used for the *pep* ν analysis (see Sec. 5.5.2) the relative difference is between -0.5% and +1.0% (Fig. 4.3 (right)). In order to correct the small residual difference between the light yield in data and simulation in the whole FV, a rescaling of the effective photon yield L_0 is performed.

Pure ^{11}C events selected with the TFC method (see Sec. 5.5.3) are a good sample of events for understanding the accuracy of the simulation of the energy response and for tuning the effective photon yield in the whole Fiducial Volume. The photon yield is rescaled to match the mean (or median) value of the TFC-tagged ^{11}C spectrum in the FV used in the analysis. This procedure is followed to define the effective photon yield for a particular Fiducial Volume.

4.4 Conclusions and outlook

The understanding of the Borexino detector response is achieved and implemented in a detailed full Monte Carlo simulation which now reproduces the time and energy response with accuracy of 1% or better for all quantities relevant for data analysis. Such

understanding and accuracy is mandatory in order to pursue the physics goals of the Borexino experiment, like the direct measurement of the rare signal from *pep* solar neutrinos, and the limits of the CNO solar neutrino flux.

Chapter 5

Measurement of the *pep* and CNO solar neutrino interaction rates in Borexino

5.1 Introduction

I report on this chapter the first measurement of the *pep* solar neutrino interaction rate and the best limits on the CNO solar neutrino interaction rate in Borexino. The rate of *pep* ν electron scattering interactions is determined to be 3.1 ± 0.6 (stat) ± 0.3 (syst) counts/(day \cdot 100ton). The upper limits on the CNO neutrino interaction rate at 68% (95%) C.L. are determined to be 4 (12) counts/(day \cdot 100ton). Assuming the *pep* neutrino flux predicted by the Standard Solar Model, we obtained a constraint on the CNO solar neutrino interaction rate of <7.9 counts/(day \cdot 100ton) (95% C.L.). Assuming the MSW-LMA solution to solar neutrino oscillations, these values correspond to solar neutrino fluxes of $(1.6 \pm 0.3) \times 10^8 \text{ cm}^{-2} \text{ s}^{-1}$ and $<7.7 \times 10^8 \text{ cm}^{-2} \text{ s}^{-1}$ (95% C.L.), respectively, in agreement with both the High and Low Metallicity Standard Solar Models. The absence of the solar neutrino signal is disfavoured at 99.97% C.L., while the absence of the *pep* neutrino signal is disfavoured at 98% C.L. These results represent the first direct evidence of the *pep* neutrino signal and the strongest constraint of the CNO solar neutrino flux to date.

The necessary sensitivity was achieved by adopting novel data analysis techniques for the rejection of cosmogenic ^{11}C , the dominant background in the 1–2 MeV region. As the signal to background ratio in the energy region of interest is orders of magnitude lower than for the ^7Be ν analysis [25], new data selection, pulse shape and analysis techniques have been developed, and much smaller backgrounds have been considered. In this chapter I describe in detail the analysis performed.

The chapter is organised as follows. In Section 5.2 I review the *pep* ν and CNO ν s signal in Borexino. In Section 5.3, all the relevant sources of physical backgrounds are discussed and estimates for their rates presented. Section 5.4 and 5.5 report on the data and event selection cuts implemented to obtain the final candidates for this analysis. Special care has been taken in the definition of the fiducial volume and in the description of the three-fold coincidence (TFC) veto.

As in the ^7Be ν analysis, the neutrino interaction rates are obtained from a fit to the distributions of the final candidates. Thus, in Section 5.6 I define the variables to

be used for the energy spectrum. In Section 5.7 I describe the procedure to obtain a single pulse shape variable to effectively discriminate between β^+ and β^- events that is implemented in the fit. In Section 5.8 I present the radial and energy distributions of the external γ -ray background, which are crucial components of the fit. The details of the fitting procedure are described in Section 5.9. The results of the analysis and the tests to validate the fitting strategy are presented in Section 5.10.

5.2 *pep* ν and CNO ν s signals

The energy spectra of solar neutrinos are shown in Fig. 2.1. The energy spectrum of electron recoils from $\nu - e$ elastic scattering interactions in Borexino is shown in Fig. 5.1 (left). The kinetic energies of electron recoils from *pep* and CNO neutrino interactions extend past the end-point of the ${}^7\text{Be}$ ν electron recoil spectrum and are within the range of energies that can be measured by Borexino. The interaction rates from *pep* and CNO ν s in Borexino are a few counts per day/100tons, ~ 10 times lower than those from ${}^7\text{Be}$ ν . The *pep* ν and CNO ν s signal and energy spectrum are described in Sec. 5.2.1 and Sec. 5.2.2 respectively.

5.2.1 *pep* ν signal

The *pep* ν is a mono-energetic solar neutrino with 1.44 MeV of energy. The *pep* reaction is part of the *pp* fusion chain, which is the main mechanism of energy production in the Sun. The features of the *pep* reaction and the production of *pep* neutrinos are described in Sec. 2.4.

The expected electron recoil energy spectrum from *pep* ν s in Borexino is shown in Fig. 5.1 (right). As with the mono-energetic ${}^7\text{Be}$ ν the spectrum from *pep* ν interactions is box-like, but with a higher end point and a considerably lower interaction rate (see Sec. 3.2, Table 3.1). The leading standard solar models (SSMs) predict an interaction rate of *pep* neutrinos in Borexino of 2.80 ± 0.04 (High Metallicity) and 2.86 ± 0.04 (Low Metallicity) cpd/100tons [60].

5.2.2 CNO ν s signal

The CNO-cycle is an alternate mechanism of energy production in the Sun, where ${}^{12}\text{C}$ serve as catalysts in the fusion of four protons into a ${}^4\text{He}$ nucleus. The features of the CNO reactions and the production of CNO neutrinos are discussed in Sec. 2.4.

The CNO cycle has two sub-cycles: the CN cycle and the sub-dominant NO cycle. In the CN cycle, ${}^{13}\text{N}$ ν and ${}^{15}\text{O}$ ν s are produced, with continuous spectra with end point energies at 1.19 MeV and 1.73 MeV respectively. As every cycle produces exactly one ${}^{13}\text{N}$ ν and one ${}^{15}\text{O}$ ν , their fluxes are very strongly correlated, with correlation coefficients of 0.991(0.984) in the GS98(AGS05) standard solar model [58].

In a minor branch of this reaction, which occurs with a relative frequency of $\sim 2\%$, the final reaction does not end with the production of ${}^{12}\text{C} + {}^4\text{He}$, but instead continues in the NO cycle. Here, an additional neutrino (${}^{17}\text{F}$ ν) is produced with a Q-value that is very close to that of the ${}^{15}\text{O}$ ν . The spectra from ${}^{17}\text{F}$ ν s and ${}^{15}\text{O}$ ν s are very similar

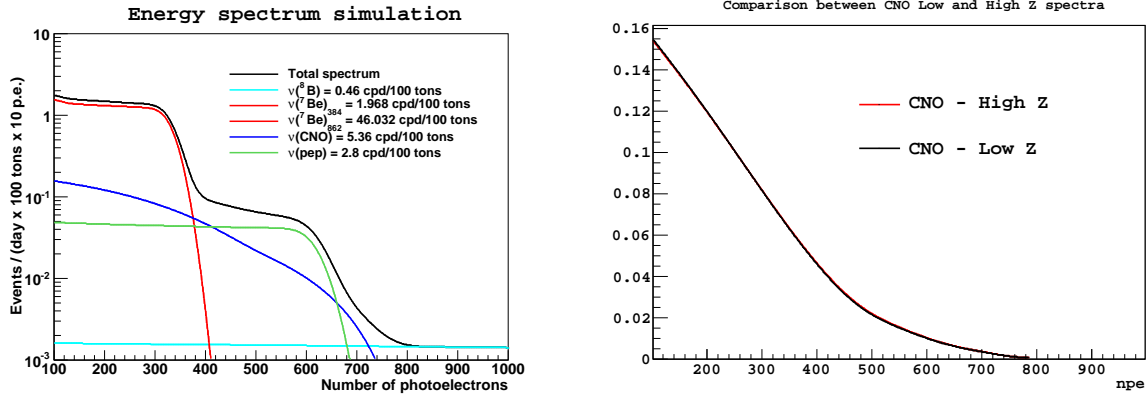


Figure 5.1: **Left panel:** The neutrino-induced electron recoil spectra expected in Borexino. The total rates are those predicted by the latest High Metallicity solar model [60]. The pep ν and CNO ν s recoil spectra with end-points in the region 1.2–1.5 MeV, whose measurement is the goal of this analysis, are shown. The already precisely measured ${}^7\text{Be}$ ν [25], whose count rate is ~ 10 times larger, is shown for comparison. **Right panel:** Normalized CNO electron recoil spectra (after considering Borexino’s energy response) assuming the central values for the CNO neutrino fluxes in the high and low metallicity solar models [60]. The maximum difference, which is $< 2.5\%$, occurs towards the higher-end of the spectrum.

and, consequently, the spectral shape of the electron recoils induced by the neutrinos from the CNO-cycle in Borexino are dependent on the ratio between ${}^{15}\text{O}$ ν + ${}^{17}\text{F}$ ν and ${}^{13}\text{N}$ ν fluxes at Earth, i.e.

$$F_{\text{CNO}} = \frac{\Phi_{\text{O}} + \Phi_{\text{F}}}{\Phi_{\text{N}}} \quad (5.1)$$

Due to the strong correlation between ${}^{15}\text{O}$ ν and ${}^{13}\text{N}$ ν (see Table 5.1), and the small relative value of Φ_{F} , this ratio is not expected to vary by more than a few percent within the standard solar models. Table 5.2 shows the maximum differences in the total electron recoil spectrum under different assumptions. The maximum differences occur past the end point of ${}^{13}\text{N}$ ν (1.19 MeV). The first entry in the table shows the differences between the latest high metallicity (High-Z (BPS11), a variant of GS98) and low metallicity (Low-Z, a variant of AGS05) models [60], where F_{CNO} is 0.772 for High-Z and 0.735 for Low-Z. The spectral differences can be seen in Fig. 5.1 (right) and they are always less than 2.5%. Additionally, as may be observed in Table 5.2, uncertainties in the mixing angle and neutrino mass-splitting in the context of the LMA-MSW scenario of neutrino oscillations causes differences in the spectral shape of less than $< 1\%$, smaller than those due to variations in F_{CNO} between solar models.

Considering this, we are justified in treating the electron recoil spectra from ${}^{13}\text{N}$ ν , ${}^{15}\text{O}$ ν and ${}^{17}\text{F}$ ν as a single CNO ν s spectrum whose shape is not sensitive to the different standard solar models or the details of neutrino oscillations, but whose absolute amplitude is affected by these. The High-Z model predicts a total CNO ν s interaction rate in Borexino of 5.4 ± 0.8 cpd/100 tons, while the Low-Z model predicts

Neutrino	Flux at the Sun / $10^8 \text{ cm}^{-2}\text{s}^{-1}$	End point / MeV	$\rho(^{13}\text{N } \nu, j)$	$\rho(^{15}\text{O } \nu, j)$	$\rho(^{17}\text{F } \nu, j)$
$^{13}\text{N } \nu$	2.96 (2.17)	1.19	1	0.991 (0.984)	0.172 (0.299)
$^{15}\text{O } \nu$	2.23 (1.56)	1.73	0.991 (0.984)	1	0.219 (0.338)
$^{17}\text{F } \nu$	0.055 (0.034)	1.74	0.172 (0.299)	0.219 (0.338)	1

Table 5.1: The second column in this table shows the central values for the predicted fluxes of the neutrinos from the CNO cycle by the latest High-Z (Low-Z) solar models. The third column shows the maximum neutrino energy for the three types, while the fourth, fifth and sixth columns show the correlation coefficients, $\rho(i, j)$, for the different decays, obtained from Tables 16 and 17 in [58]. Even though the total fluxes from neutrinos from the CNO cycle is $\sim 30\%$ smaller for the Low-Z model, the strong correlation between $^{13}\text{N } \nu$ and $^{15}\text{O } \nu$, and the small relative flux from $^{17}\text{F } \nu$, lead to relatively small changes in the electron recoil spectral shape (see Table 5.2).

Conditions	Fractional diff. in normalized e^- recoil npe spectrum from CNO ν s
High-Z vs. Low-Z	$< 2.5\%$
Central osc. pars. vs. $+1\sigma$ in Δm^2 and θ [2]	$< 0.25\%$
Central osc. pars. vs. -1σ in Δm^2 and θ [2]	$< 0.25\%$
With vs. without Earth matter effects	$< 0.1\%$
With vs. without radiative corrections	$< 1\%$

Table 5.2: This table shows the differences in the total electron recoil spectrum from CNO neutrinos observed in Borexino under different model assumptions. The first entry shows the largest difference, which occurs between the high and low metallicity solar models [60] (see Fig. 5.1-right). The following three entries show that changes in the parameters of the LMA-MSW model of neutrino oscillations have a much smaller effect in the spectral shape relative to the differences between the solar models. Overall, the small spectral differences in the electron recoil spectrum from the model assumptions introduces a negligible systematic effect in the estimation of the total CNO neutrino interaction rate in Borexino. For reference, the effect of radiative corrections in the recoil spectra is presented in the last entry.

$3.8^{+0.6}_{-0.5}$ cpd/100 tons.

5.3 Radioactive backgrounds

As discussed in Sec. 5.2, the interaction rates for *pep* ν and CNO ν s in Borexino are ~ 10 times lower than those from ${}^7\text{Be}$ ν , whose measurement has been the main goal of Borexino [25]. Because of this, special care needs to be taken to consider radioactive backgrounds with rates that are one or two orders of magnitude lower than those of relevance for the ${}^7\text{Be}$ ν analysis. Similarly to the ${}^7\text{Be}$ ν analysis, the *pep* ν and CNO ν s interaction rates are obtained through a fit to the signal and background distributions in different parameter spaces (see Sec. 5.9) and, therefore it is of great importance to make estimates of the possible radioactive contaminants in order to decide which should be considered for the fit. In Sec. 5.3.1, 5.3.2 and 5.3.3, the predicted rates for the different types of backgrounds are evaluated in the fiducial volume (see Sec. 5.5.2) and energy range of interest to decide which should be considered in this analysis.

5.3.1 Radiogenic internal backgrounds

The main radiogenic backgrounds for the ${}^7\text{Be}$ ν analysis [25] are also the dominant backgrounds for this analysis. ${}^{85}\text{Kr}$, which has been measured from the delayed coincidence analysis to be $30.4 \pm 5.3 \pm 1.3$ cpd/100tons [25] and ${}^{210}\text{Bi}$, whose value from the ${}^7\text{Be}$ analysis fit was $40.3 \pm 1.5 \pm 2.3$ cpd/100tons, are the largest radioactive backgrounds to be included in the fit. ${}^{210}\text{Po}$, which has the highest rate of any of the internal contaminants above the ${}^{14}\text{C}$ end-point (~ 2.1 cpd/ton [25]), is removed from the spectrum through the method of statistical subtraction, discussed in Sec. 5.5.4. The only remaining contribution from ${}^{210}\text{Po}$ to the final spectrum is the γ -ray producing decay (0.8 MeV γ + 4.5 MeV α), which has a relative intensity of 0.00121%.

Similarly to the ${}^7\text{Be}$ ν analysis, the ${}^{214}\text{Pb}$ decay rate can be estimated from the number of detected fast ${}^{214}\text{BiPo}$ coincidences in the analysis exposure [25, 96]. For the exposure considered in the ${}^7\text{Be}$ ν analysis, the ${}^{214}\text{Pb}$ rate was estimated to be ~ 1.7 cpd/100tons [25]. Since most of the events considered in the *pep* ν and ${}^7\text{Be}$ ν analysis comes from the same data set, the ${}^{214}\text{Pb}$ rate should not be very different between the two analysis. Yet, small differences are expected as some ${}^{214}\text{Pb}$ comes from radon gas emanated by the nylon vessel or introduced during operations, leading to a ${}^{214}\text{Pb}$ spatial distribution that its not uniform and, therefore, dependent on the fiducial volume considered. Residual ${}^{214}\text{Bi}$ is expected from the inefficiencies in the selection criteria for the fast coincidence tag (see Sec. 5.5.1). α -decays from ${}^{222}\text{Rn}$ and its daughter, ${}^{218}\text{Po}$, are removed from the spectrum and will not be considered in the fit.

The next major source of radiogenic background in the scintillator should be the β daughters from the long lived radioactive isotopes ${}^{238}\text{U}$, ${}^{232}\text{Th}$, ${}^{40}\text{K}$ and ${}^{235}\text{U}$. For ${}^{238}\text{U}$ and ${}^{232}\text{Th}$, we have estimates of their mass fractions in the scintillator of $(1.67 \pm 0.06) \times 10^{-17}$ and $(4.6 \pm 0.8) \times 10^{-18}$, respectively [25]. Of the ${}^{238}\text{U}$ daughters in the decay chain before ${}^{222}\text{Rn}$, only ${}^{234m}\text{Pa}$ (Q-value= 2.29 MeV) can have any contribution in our spectrum of β -like events. In the ${}^{232}\text{Th}$ chain, ${}^{228}\text{Ac}$, ${}^{212}\text{Pb}$ and ${}^{208}\text{Tl}$ could offer some

Isotope	Source	Residual rate cpd/100tons	Residual differential rate at 1.44 MeV / cpd/100tons/MeV
$^{210}\text{Po } \alpha + \gamma \text{ decay}$	^{210}Po	< 0.025	0
^{234m}Pa	^{238}U	1.78 ± 0.06	0.64 ± 0.02
^{214}Bi	$^{238}\text{U}, ^{226}\text{Ra}, ^{222}\text{Rn}$	0.045 ± 0.002	< 0.009
^{228}Ac	^{232}Th	0.16 ± 0.03	< 0.08
^{212}Pb	$^{232}\text{Th}, ^{220}\text{Rn}$	0.16 ± 0.03	0
^{208}Tl	$^{232}\text{Th}, ^{220}\text{Rn}$	0.06 ± 0.01	0
$^{212}\text{BiPo}$ pileup	$^{232}\text{Th}, ^{220}\text{Rn}$	< 0.05	< 0.02
^{235}U daughters	^{235}U	0.080 ± 0.003	0
$\bar{\nu}_e$ prompt β^+	geo + reactor	0.023 ± 0.005	0.009 ± 0.002
<i>pep</i> ν	Sun	2.80 ± 0.04	1.94 ± 0.03

Table 5.3: Expected rates of radiogenic backgrounds that were not included in the $^7\text{Be } \nu$ analysis. For the estimate of the $^{210}\text{Po } \alpha + \gamma$ rate we have assumed that the total ^{210}Po rate in our exposure will be smaller than in the ^7Be analysis, as in this analysis the first eight months of data after filling, during which the rate was highest, are excluded (see Sec. 5.4). To estimate the rate of ^{234m}Pa we have considered a ^{238}U mass-fraction in the scintillator of $(1.67 \pm 0.06) \times 10^{-17}$ [25] and assumed secular equilibrium. For estimating the residual ^{214}Bi , we have used the ^{214}Pb rate from the ^7Be analysis and considered an efficiency for identifying $^{214}\text{BiPo}$ coincidences, where the ^{214}Bi produces more than 100 npe, to be $> 98\%$. For ^{228}Ac , ^{212}Pb and ^{208}Tl we have assumed a ^{232}Th mass-fraction in the scintillator of $(4.6 \pm 0.8) \times 10^{-18}$ [25] and secular equilibrium. To estimate an upper limit on the fraction of $^{212}\text{BiPo}$ decays that end up as a single cluster in the final spectrum, we have made the conservative assumption that our discrimination for pileup has 100% efficiency for $\Delta t > 100$ ns and 0% for $\Delta t < 100$ ns. For the β daughters in the ^{235}U chain (none of which have a Q-value > 1.44 MeV) we have assumed the abundance of ^{235}U in the scintillator to be the same as the natural one (0.7%). To estimate the $\bar{\nu}_e$ background we have used results from the geo-neutrino analysis [100]. For comparison, the last entry in the table shows the expected *pep* interaction rate as predicted by the High Z solar model [60].

non-negligible contribution. The β -decay of ^{212}Bi is removed very effectively by the fast coincidence tag (see Sec. 5.5.1) due to its time correlation with ^{212}Po ($\tau = 299$ ns). Yet, as the time difference between the events is comparable to the characteristic decay time of the scintillator light signal, there is a possibility of $^{212}\text{BiPo}$ pileup. Still, even if the $^{212}\text{BiPo}$ is considered as a single cluster, selection cuts include discrimination on pulse-shape variables that try to identify pileup and non- β -like events (see Sec. 5.5.1), possibly excluding the cluster from the final spectrum.

The high levels of ^{40}K measured in PPO was identified as one of the most “troublesome” impurities in the design of Borexino [107]. Until this analysis, no limit has been circulated on the ^{40}K contamination, although its inclusion in the fit had no systematic effect on the results of the ^7Be analysis [25]. As the information regarding this contaminant is very limited and it may be present at levels relevant for the *pep* ν analysis, ^{40}K is included in the fit.

^{235}U has a natural abundance of 0.7% and, as the chemical properties of its daughters are very similar to those of ^{238}U , it is reasonable to expect their relative abundance in Borexino to be similar to the natural one. In any case, it is possible to place a limit on the ^{235}U contamination by searching for the double- α time coincidence of $^{219}\text{Rn}^{215}\text{Po}$ ($\tau = 1.8$ ms). An analysis to search for this coincidence has found a rate of 0.05 ± 0.04 cpd/100tons ($0.5\% \pm 0.4\%$ $^{235}\text{U}/\text{U}$), consistent with the natural abundance.

Another possible background for our analysis are the prompt events from geological and reactor $\bar{\nu}$. The Borexino Collaboration has already performed a measurement of these [100]. A summary for estimates of this and the other isotopes are presented in Table 5.3. The differential rate at the *pep* ν energy is also presented for comparison. We have decided to not exclude in the fit any species whose differential rate at 1.44 MeV is expected to be more than one twentieth (5%) of that from *pep* ν electron recoils. ^{234m}Pa is included as a free component in the fit (see Sec. 5.9). The species whose differential rate at 1.44 MeV is expected to be less than one twentieth (5%) of that from *pep* ν electron recoils are included in some of the trial fits. The impact of these species on the fit result have been evaluated as a systematic uncertainty (see Sec. 5.10.3).

5.3.2 Cosmogenic backgrounds

^{11}C is the dominant cosmogenic background in Borexino ($28.5 \pm 0.2 \pm 0.7$ cpd/100tons [25]) and the biggest challenge for the measurement of *pep* ν and CNO ν s. Its treatment requires attention and it is the subject of Sec. 5.5.3 and 5.7. Other cosmogenic backgrounds have already been evaluated in the context of the ^8B ν analysis [81]. Table 5.4 shows the expected residual rate of these cosmogenics, considering the 300 ms cut performed after every muon (see Sec. 5.5.1). The differential rate in the table shows that only ^6He has a value that is greater than 5% of that from *pep* ν and, therefore, it is included in the fit. An exemption must be made for ^{10}C . Even though its starting point (1.74 MeV) is past the *pep* ν energy, its count rate is relatively high (0.54 ± 0.04 cpd/100tons) and a large fraction of its spectrum falls within the fit region (< 3.2 MeV, see Sec. 5.9), leading to a non-negligible contribution in the higher-end of the fit. The 0.48 MeV γ -rays from ^7Be , on the other hand, is buried under the ^{85}Kr , ^{210}Bi and ^7Be ν recoil spectra (~ 150 cpd/100tons/MeV), therefore it should have a negligible effect on

Isotope	Q-value (E_γ) MeV	Residual rate cpd/100tons	Residual differential rate at 1.44 MeV cpd/100tons/MeV
n	(2.22)	< 0.005	0
^{12}B	13.4	$(7.1 \pm 0.2) \times 10^{-5}$	$(2.49 \pm 0.07) \times 10^{-6}$
^8He	10.6	0.004 ± 0.002	$(2.6 \pm 1.2) \times 10^{-4}$
^9C	16.5	0.020 ± 0.006	$(1.6 \pm 0.5) \times 10^{-3}$
^9Li	13.6	0.022 ± 0.002	$(1.4 \pm 0.1) \times 10^{-3}$
^8B	18.0	0.21 ± 0.05	0.017 ± 0.004
^6He	3.5	0.31 ± 0.04	0.15 ± 0.02
^8Li	16.0	0.31 ± 0.05	0.011 ± 0.002
^{11}Be	11.5	0.034 ± 0.006	$(3.2 \pm 0.5) \times 10^{-3}$
^{10}C	3.6	0.54 ± 0.04	0
^7Be	(0.48)	0.36 ± 0.05	0
<i>pep</i> ν	1.44 MeV	2.80 ± 0.04	1.94 ± 0.03

Table 5.4: Expected rates of cosmogenic backgrounds. The total rates were obtained from Table 1 in [81], except for n, ^6He and ^7Be , the last two which were extrapolated from simulation results performed by the KamLAND Collaboration [136], following the methodology from the ^8B ν analysis (see Eq. 3 in [81]). To obtain the residual rate we have considered the 300 ms veto applied after every muon (see Sec. 5.5.1). The ^7Be rate is that of the 0.48 MeV γ -ray, which has a relative intensity of 10.5% and is the only decay that deposits any visible energy in the detector. The contribution from cosmogenic neutrons produced directly by the muon is negligible given the short capture time (~ 0.26 ms) and their main contribution comes from the neutron-producing decays of ^9Li and ^8He that are missed by the fast coincidence veto (Sec. 5.5.1). The residual rates from ^{12}N and ^{13}B (not in the table) are expected to be smaller than those from ^{12}B as their lifetimes are shorter and their production yields smaller. Likewise, production yields of ^{15}O and ^{13}N are expected to be 20 times smaller than those from ^{11}Be [136]. The last entry shows the expected interaction rates for *pep* ν (High Z model) for comparison.

the spectral fit and can safely be excluded, even if its total count rate is comparable to that of ^{10}C and ^6He .

Cosmogenic backgrounds originating from outside the detector and from untagged muons should be smaller than those presented in Table 5.4. Untagged muons that pass all the standard and fiducialization cuts and make it to the final spectrum in the ^7Be ν analysis have an expected rate $< 3 \times 10^{-4}$ cpd/100tons (assuming an outer detector (OD) absolute efficiency of 99.2% [105] and independence between ID and OD muon flags). Except for neutrons, none of the other cosmogenic isotopes can travel very far away from the muon shower and, therefore, all of their decays in the FV will be preceded by the muon shower in the scintillator, for which the tagging efficiency is highest ($> 99.992\%$ [105]). There is the possibility though, that neutrons produced outside the inner vessel (IV) will deposit energy within the FV. Those that capture in the IV may be vetoed by the fast coincidence condition, as proton recoils from the thermalization will be visible near the capture position. Additionally, the residual rate for those produced in the buffer or the water tank (WT) will be highly suppressed due to the possibility to tag the parent muon with Borexino's muon veto [105]. Furthermore, any surviving proton recoil signal would be subtracted from the final spectrum due to their α -like pulse shape. In the context of the geo-neutrino analysis, the number of neutrons from the rock and the WT tank that mimic $\bar{\nu}_e$ signals was found to be $< 1.4 \times 10^{-4}$ cpd/100tons [100]. The corresponding background (i.e. proton recoils from fast neutrons or from untagged muons that do not cross the IV, where the neutron does not capture in the scintillator and the reconstructed position of the recoils is within a reduced fiducial volume) is not expected to be relevant for this analysis.

5.3.3 External γ -ray backgrounds

External γ -ray backgrounds from natural radioactivity are a great challenge for low background detectors. The most effective method to decrease these backgrounds is through the selection of a fiducial volume (FV). The considerations taken in the choice of the fiducial volume for this analysis are described in detail in Sec. 5.5.2. A compromise has to be made between fiducialization and exposure, leading to a fiducial volume where the contribution from external background cannot be neglected. The approach taken to deal with the remaining external background is a simultaneous fit to the radial distribution of events within the FV and their energy spectra (see Sec. 5.9.4). For this approach to succeed it is mandatory to determine which external background species contribute significantly to the final set of events and include their corresponding spatial and energy distributions in the fit.

The expected count rates for γ -rays of different isotopes from different external sources are shown in Table 5.5. The leading backgrounds are from the 2.61 MeV γ -ray from ^{208}Tl and the higher energy γ -rays from ^{214}Bi , which come from ^{238}U and ^{232}Th contaminants in the PMTs and Light Cones installed on the Stainless Steel Sphere (SSS). Their energy spectra in the FV is highest towards the full-energy peak of the γ -rays, with a tail that extends to lower energies due to γ -rays which deposited only a fraction of their energy in the FV (see Sec. 5.8 and Fig. 5.14). The contribution from decays of ^{238}U and ^{232}Th daughters in the nylon vessels and buffer fluid, as well as also

Source	Expected in FV cpd	Expected in FV and $0.25 \text{ MeV} < E < 1.30 \text{ MeV}$ / cpd
^{208}Tl from PMTs	~ 5.7	~ 0.2 [137]
^{214}Bi from PMTs	~ 6.6	~ 0.9 [137]
^{40}K from PMTs	~ 0.2	~ 0.2 [137]
Light Cones and SSS	NA	$0.6 - 1.8$ [112, 137]
Nylon vessels	NA	< 0.05 [112]
End regions	NA	< 0.06 [112]
Buffer	NA	< 0.02 [138]
<i>pep</i> ν	2.00 ± 0.03	1.46 ± 0.02

Table 5.5: Expected rates of external γ -ray backgrounds in the FV considered in this analysis. The estimates for ^{208}Tl , ^{214}Bi and ^{40}K from the PMTs were made using the full Borexino Monte Carlo simulation code (see Chapter 4), starting from the measured contaminations of the PMTs [137]. The lower value for the rates from the SSS and Light Cones were scaled to the reduced FV from previous estimates [112], assuming a γ -ray absorption length of 25 cm. The upper value considers the discrepancy between the PMT estimates in [112] and those given in the first three entries of this table. Likewise, the expectations for the background from the nylon vessels and end regions have been scaled to the FV, also considering the vertical cuts (Sec. 5.5.2). For the case of the nylon vessel, we have checked, using the full Borexino Monte Carlo simulation code, that the estimate of the ^{208}Tl background is consistent with the limit [138]. The upper limit for the background originating in the buffer fluid has been estimated with Monte Carlo simulations, assuming contaminations of ^{238}U and ^{232}Th in the buffer that are 100 times greater than those in the scintillator [138]. For comparison, the last entry in the table shows the expected rates of electron recoils from *pep* ν (High Z model).

Period	Start Week	End Week	Run Start	Run End	Livetime (days)
2	13 Jan 2008	01 Jun 2008	6898	7937	127.292
3	08 Jun 2008	05 Oct 2008	7938	8791	99.082
4	05 Oct 2008	11 Jan 2009	8910	9451	73.728
5	08 Feb 2009	14 Jun 2009	9713	10297	84.041
5a	28 Jun 2009	12 Jul 2009	10497	10545	9.017
6	26 Jul 2009	25 Oct 2009	10750	11517	74.005
7	01 Nov 2009	24 Jan 2010	11518	12400	72.648
8	14 Feb 2010	2 May 2010	12489	12940	68.463
TOTAL	13 Jan 2008	2 May 2010	6898	12940	608.276

Table 5.6: Division of data into different periods. Livetime in last column is before any analysis cuts.

^{40}K and ^{60}Co in the end regions (above and below the vessels), are lower by at least an order of magnitude and are expected to contribute to less than 5% in the energy region of electron recoils from *pep* ν . The external background contributions from ^{208}Tl , ^{214}Bi and ^{40}K originating from a uniform spherical distribution at the SSS (see Sec.5.8) are included in the fit.

5.4 Data selection

The data taken into account encompasses Borexino runs from periods 2 to 8 (see Table 5.6). The corresponding total live time is 608.276 days and the exposure in the Fiducial Volume used in this analysis is 43370 ton \times day before any cut.

5.5 Event Selection

In this section is described the event selection cuts implemented in order to create an energy spectrum for analysis. The initial set of cuts applied for selection of events in this analysis are the “Standard Cuts” as in the document elaborated by the ^7Be Cuts Committee [139] (see Sec. 5.5.1), except for the fiducial volume definition, which is described in detail in Sec. 5.5.2. Further suppression of ^{11}C background is performed via the three-fold coincidence method (see Sec. 5.5.3). Additional pulse shape discrimination methods has been used to remove α -like events (see Sec. 5.5.4).

5.5.1 Selection of point-like scintillation events

An initial set of standard cuts are performed to clean the analysis data sample from muon and short-lived muon daughter events, fast chains of correlated background, events with mis-reconstructed position or energy and electronic noise. Listed below are the standard cuts used to generate the starting energy spectrum:

- Remove muon cosmogenic and post-muon (300 ms) events.

- Remove zero cluster events.
- Remove sequence of fast coincidences ($\Delta t < 2$ ms and $\Delta s < 1.5$ m).
- Remove service triggers.
- Keep only events with a single cluster.
- Keep only events with cluster start time in the right position in the gate window.
- Remove events whose distribution of PMT hits is not uniform in space.
- Remove events outside the Fiducial Volume (FV).
- Remove electronic noise events.

The exact definition of these cuts is described in Sec. 2.3 of the Borexino internal note [139]. Except for the last two cuts therein (15 and 16), all other cuts are implemented identically. These cuts remove less than $< 0.3\%$ of “good” events (details the PhD thesis [119]). The most relevant difference in the event selection with respect to the ${}^7\text{Be}$ ν analysis is a different fiducial volume definition, which is described in detail in Sec. 5.5.2. The dead time introduced by these cuts in the context of the ${}^7\text{Be}$ ν analysis has been evaluated in Sec. 2.5 of [119]. The largest loss of live time comes from the application of the 300 ms cut after muons, which has been measured to be 1.8% and has been accounted for this analysis, decreasing the live time of the dataset to 598.14 days. The dead time due to the other cuts is $< 1\%$, which is small compared to the systematic uncertainties from the energy calibration and fit methods (Sec. 5.10.3), and can be neglected. Finally, the fast coincidence rate of events tagged as ${}^{214}\text{BiPo}$ decays in the FV is used to estimate the ${}^{214}\text{Pb}$ contamination in the final set of events and fix its rate in the fit.

5.5.2 Fiducial volume definition

The fiducial volume selected for this analysis was chosen so as to maximise the target scintillator mass while minimising the effect of external background and variations in the light collection efficiency.

5.5.2.1 External Background

As discussed in Sec. 5.3.3, there are two main sources of external background:

- background from the Stainless Steel Sphere (SSS), photomultiplier tubes, light cones and other material connected to the SSS;
- background from the end-cap regions of the inner and outer nylon vessels.

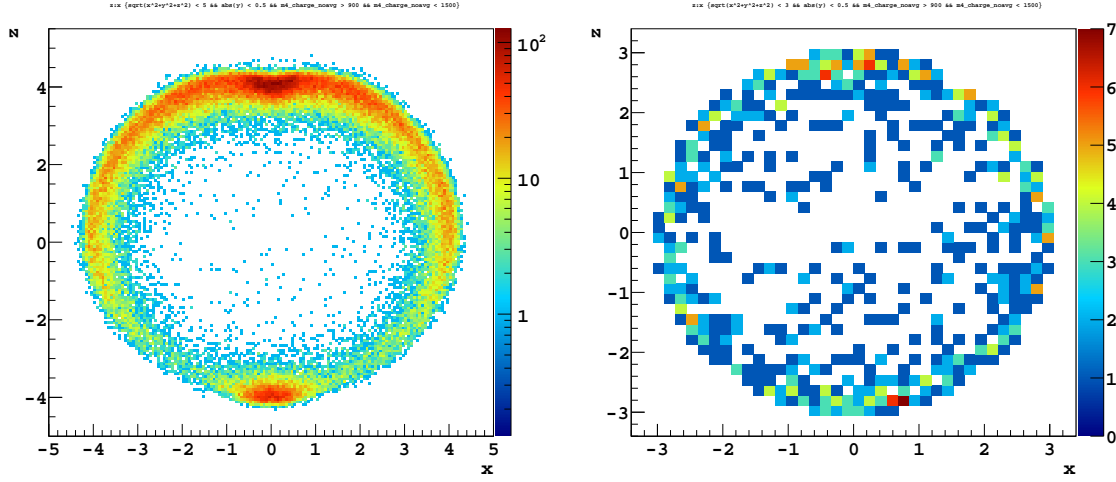


Figure 5.2: Spatial distribution of events with reconstructed position $-1 \text{ m} < y < 1 \text{ m}$ in the 900 - 1500 npe energy region, which is dominated by external γ -rays from ^{208}Tl and ^{214}Bi . The positions are expressed in meters. **Left panel:** Events within the inner vessel. **Right panel:** For $r < 3 \text{ m}$.

To study the spatial distribution of γ -ray events from the SSS and other components at that radius, we plotted the reconstructed position of all events with charge between 900 and 1500 number of photoelectrons (npe). This energy region is dominated by ^{208}Tl and ^{214}Bi γ -ray interactions, with a smaller contribution ($\sim 25\%$) from ^{10}C and ^{11}C decays (see Fig. 5.16). The position of all events reconstructed within the Inner Vessel (IV), in a 1 m thick slice ($-1 \text{ m} < y < 1 \text{ m}$), is shown in Fig. 5.2. As can be seen, the number of events decreases as one moves radially away from the SSS towards the centre of the IV. The hot spots along the z -axis, at the top and bottom of the IV are due to the end-cap regions and will be discussed in detail below. A larger number of events are seen in the top hemisphere, due to the fact that the deformed nylon vessel is closer to the SSS at the top than at the bottom. If the events are restricted to those reconstructed within 3 m, the same radial cut used for the ^7Be ν analysis [25], one can see (Fig. 5.2, right panel) that the z -dependence is no longer evident, and the background seems to increase uniformly with radius. We have found, by testing different fiducial volumes, that the threefold coincidence cuts are most efficient at removing ^{11}C within a radius of 2.8 m. Therefore, the fiducial volume has been chosen to lie within a sphere of 2.8 m.

Due to their proximity to the scintillator, there is a large rate of background events originating from the end-cap regions of the inner and outer nylon vessel (see Fig. 5.2). The energy spectrum of the background from the end-cap regions is difficult to model due to the presence of multiple γ emissions and, like in the ^7Be analysis [25], a fiducial volume cut along the z -axis was made to exclude events from those regions. The background from the end-caps is most evident in the energy region between the ^{14}C tail and the ^{210}Po peak (120 - 145 npe). Fig. 5.3 shows the distribution of events in the entire IV and within 3 m. One can see that the top end-caps appear to be more active than at the bottom, and that the events penetrate well within a 2.8 m radius. The tail

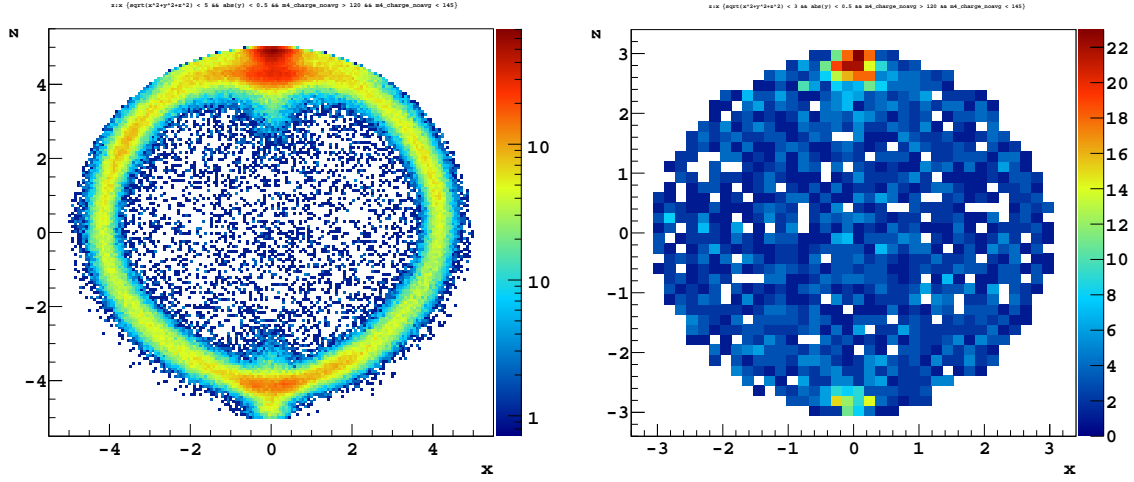


Figure 5.3: Spatial distribution of events with reconstructed position $-1 \text{ m} < y < 1 \text{ m}$ in the energy region between the ^{14}C tail and the ^{210}Po peak (120 - 145 npe), where the effect of the background from the end caps is most evident. The positions are expressed in meters. **Left panel:** Events within the inner vessel. **Right panel:** For $r < 3 \text{ m}$.

of events just under and above the top and bottom end-caps respectively are thought to be mis-reconstructed background events from the end-caps. A large fraction of the light emitted by these events is occulted by the mechanical structure of the end-cap and could cause events to be reconstructed radially inward. In order to safely exclude these events from the end-cap region, the fiducial volume must lie within $2.2 \text{ m} > z > -2.4 \text{ m}$.

5.5.2.2 Light Collection Uniformity

The energy resolution, critical to obtaining a good spectral fit, depends strongly on the uniformity of the light collection within the fiducial volume. If one define the position-dependent light yield, relative to the value at the centre of the detector, as $LY(\vec{r})$, then the variance of the energy response function for a monoenergetic event with mean charge value Q is given by:

$$\sigma^2(Q) = k \cdot Q + \frac{\text{var}_{FV}(LY(\vec{r}))}{\text{mean}_{FV}^2(LY(\vec{r}))} \cdot Q^2, \quad (5.2)$$

where the first term represents the intrinsic statistical variation of the scintillation process and $\text{mean}_{FV}(LY(\vec{r}))$ and $\text{var}_{FV}(LY(\vec{r}))$ are the mean and variance of the light yield over the fiducial volume. In order to obtain a precise spectral fit, we require that the second term in Eq. 5.2 be less than 10% of the first over the energy range $< 800 \text{ npe}$. One can evaluate the uniformity of the light collection by studying the peak position of the ^{214}Po source at different locations within the detector. By interpolating between the source positions, we obtain a map of the light collection throughout the IV, as shown in Figure 5.4. It can be seen that the light collection is fairly uniform in the top hemisphere, but decreases as one moves downward due to the larger number of dead photomultiplier tubes at the bottom. With the radial cut set at 2.8 m by the external

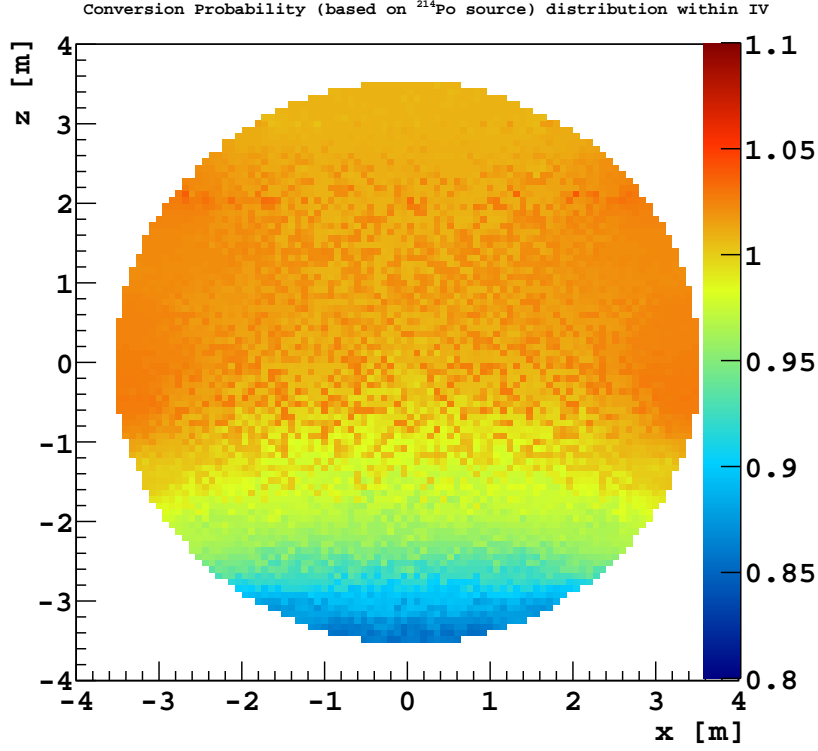


Figure 5.4: Light collection efficiency within 3.5 m based on ^{214}Po calibration source data.

background from the SSS, and the upper z cut set at 2.2 m due to background from the top end-caps, we varied the lower z cut to maximise the volume while maintaining the relative variation in light collection in uniformity. The optimal value for the lower z cut was found to be -1.8 m.

5.5.2.3 Fiducial Volume Definition

Combining the above restrictions, we define the fiducial volume cut for this analysis as $r < 2.8$ m and $2.2 \text{ m} > z > -1.8$ m. The radial limit is determined by the external background from the SSS sphere and the effectiveness of the three-fold coincidence cuts, the upper z cut is constrained by the background from the top end-cap regions, and the lower z cut by the restriction on the light collection uniformity. The volume of scintillator contained within this region is 81.26 m^3 which corresponds to a fiducial mass of 71.30 tons.

5.5.3 Three-fold coincidence veto

The main background for the detection of $\text{pep } \nu$ in Borexino is ^{11}C . The ^{11}C nuclides are produced by cosmogenic muons through a reaction resulting in the emission of free neutrons in $\sim 95\%$ of the cases [123]:

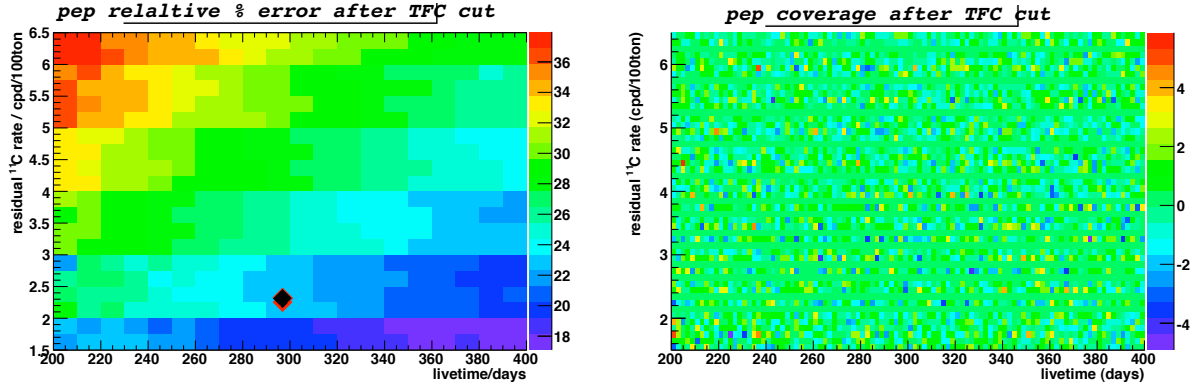


Figure 5.5: **Left panel:** Simulation-based prediction of the sensitivity for the *pep* ν interaction rate measurement as a function of the residual ^{11}C rate and effective exposure. The z -axis (color) is the error on the *pep* ν interaction rate returned by the fit. The black diamond corresponds to the TFC-subtracted spectrum used in this analysis (Fig. 5.6). **Right panel:** In this test the z -axis (color) is the bias estimator: (*pep* fitted rate - simulated *pep* rate) / *pep* rate uncertainty. No significant bias in the fitted *pep* ν interaction rate is expected from the loss of exposure. The fits are χ^2 -fits performed to the TFC-subtracted nhits spectrum with 5 nhits binning.

$$\mu (+ \text{secondaries}) + ^{12}\text{C} \rightarrow \mu (+ \text{secondaries}) + ^{11}\text{C} + n \quad (5.3)$$

^{11}C then decays with a mean life $\tau=29.4$ min via positron emission:

$$^{11}\text{C} \rightarrow ^{11}\text{B} + e^+ + \nu_e \quad (5.4)$$

where the total energy released in the detector is between 1.02 and 1.98 MeV (β^+ with Q-value of 0.96 MeV + 2×0.511 MeV γ -rays from e^+ annihilation) and lies in the energy region of interest for the detection of electrons recoils from *pep* ν .

The ^{11}C rate in Borexino is $28.5 \pm 0.2 \pm 0.7$ cpd/100tons [25], 10 times greater than the interaction rate of *pep* ν . Fortunately, it is possible to reject most of ^{11}C decays via a threefold coincidence (TFC) between the ^{11}C decay, the parent muon, and the signal from capture of the free neutron, as suggested by Deutsch in [140] and first implemented in [141].

There are ~ 1650 muons per day crossing Borexino's inner vessel (IV), which are tagged with an efficiency of 99.992% [105]. Of these muons, ~ 70 per day produce at least one neutron, with a mean multiplicity of ~ 3.6 neutrons per muon. The neutrons are thermalized and captured by hydrogen in the scintillator with a characteristic capture time of ~ 0.26 ms and the emission of a 2.22 MeV γ -ray. The reconstruction of the position of the capture γ -rays and of the track of the parent muon are crucial for the success of the three-fold coincidence technique. Multiple muon tracking algorithms have been developed by the Borexino Collaboration, their description and performance, together with the details of cosmogenic neutron detection, are discussed in [105].

The threefold coincidence algorithm vetoes space-time regions of the detector after muon and neutron coincidences in order to exclude the subsequent ^{11}C decays. The guiding principle for the determination of the most appropriate parameters is the search for the best compromise between ^{11}C rejection and preservation of residual exposure after the veto cuts. We have applied different veto configurations on the data, resulting in different residual ^{11}C rates and effective residual exposures. From an analysis on simulated data samples (Fig. 5.5), we estimated which configuration leads to the smallest expected uncertainty in the *pep* ν interaction rate.

The evaluation of the effective residual exposure after all veto cuts, many of which overlap in time and space, has been performed using two independent ways. In the first way, we assumed that ^{210}Po , which rate is high in Borexino and which events can be easily selected by means of pulse-shape and energy cuts, is uncorrelated with the TFC cuts and, therefore, the number of counts that survive the vetoes should be proportional to the residual exposure. In the second way, we developed a simulation feeding events uniformly in space and time to the veto cuts. The residual exposure is computed from the fraction of the simulated events that survive the vetoes. The residual exposures calculated by these two ways agrees to much better than 1%. An initial evaluation of the residual ^{11}C after the application of the TFC is done by checking the fraction of events that survive the cuts in an energy interval where mostly ^{11}C is expected, namely between 530 and 610 nhits. A small component of external background contributes to counts in this energy region and cannot be easily estimated, therefore ^{11}C suppression can actually be better than quoted.

The TFC procedure can be summarised as follows:

- A 2 hours blackout is applied at the beginning of each DST, rejecting any event in the entire detector. This is needed since the current processing of DSTs is done in parallel, and no information regarding muon and neutron coincidences is carried over between DSTs.
- Additional blackouts have been applied at the beginning of each run, since muon and neutron coincidences can be lost in the interval between runs. The veto time in minutes is obtained by $10 + 60 (1 - \exp(-3\Delta t/\tau))$, where Δt is the dead-time interval between subsequent runs in minutes.
- For high multiplicity events a blackout of 2 hours is applied.
- When the reconstructed neutron position is not reliable, due to DAQ saturation and/or to a large fraction of noise hits, we apply a cylindrical veto along the parent muon track with a radius of 80 cm for a time span of 2 hours.
- If neutron clusters in a muon gate are found more than $2\ \mu\text{s}$ after the muon, then the cylindrical veto along the muon track described above is applied.
- A cylindrical veto is also applied around muon tracks in events with nhits > 1000 after which at least one neutron is found.
- If a neutron is found and its position is considered reliable, we exclude any event less than 1 m away from it for 2 hours. Moreover, the neutron projection on the

parent muon track is calculated and another 2 hours, 1 m spherical veto is applied around this position.

The application of the algorithm on the selected data results in $> 89.4\%$ ^{11}C rejection with a residual exposure of 48.5%. Fig. 5.6 shows the starting and the final spectrum following the stage of ^{11}C reduction performed with the three-fold coincidence veto. The resulting exposure of the TFC-subtracted spectrum is 20409 days \times tons, while for the spectrum of the TFC-tagged events it is 23522 days \times tons.

It is important to remark that overall acceptance and leakage of the TFC cuts are not expected to introduce any bias in the final result (see Sec. 5.10), as long as they do not cause a spectral distortion in the energy spectrum. By the way the TFC veto is defined, its overall acceptance and leakage should be completely uncorrelated from the visible energy of the event. An increase in the efficiency of the TFC would primary result in a final spectrum with a reduced ^{11}C component. Vice versa, should the neutron identification fail in a fraction of the events, this would cause an increase in the ^{11}C component or a reduction of the overall unvetoes exposure. In both cases no distortion of the energy spectrum, which could potentially result in a bias in the final result, is expected.

The TFC veto can also be used to tag high-purity sample of ^{11}C events. These samples has been used for several purposes, like understanding the dependence of the reconstructed energy of the event with respect the position and tune the light yield of the Monte Carlo simulation, studying the pulse shape of the ^{11}C events in order to identify the o-Ps formation (see Sec. 5.7.2) and develop pulse shape variables to discriminate between β^+ and β^- events (see Sec. 5.7.3).

5.5.4 Statistical subtraction of α -like events

α -like events are removed from the final energy spectrum with the method of statistical subtraction. For each energy bin, the distribution of the Gatti variable (see Sec. 3.4.2) is fitted using two reference distributions, one representing the β population, the second one, the α population. For each energy bin we fit and separate the two components, thus computing the relative amount of α and β events. In this way, the contributions from ^{210}Po and other α decays are statistically removed from the energy spectrum. The detailed description of the method, its implementation, efficiency, systematic effects, biases, and other related issues are discussed in detail in the PhD thesis [118] and [119]. Fig. 5.7 shows the final spectrum before and after this procedure.

5.6 Energy variables

Within the Borexino analysis framework (MOE-Echidna), several energy variables are available, each with a slightly different method of estimating the energy of a given event. The definition of the energy variables used in this analysis are given below. Additional information on the energy variables, their implementation, biases, simulation, analytical computation, and other related issues can be found in the PhD thesis [118] and [119].

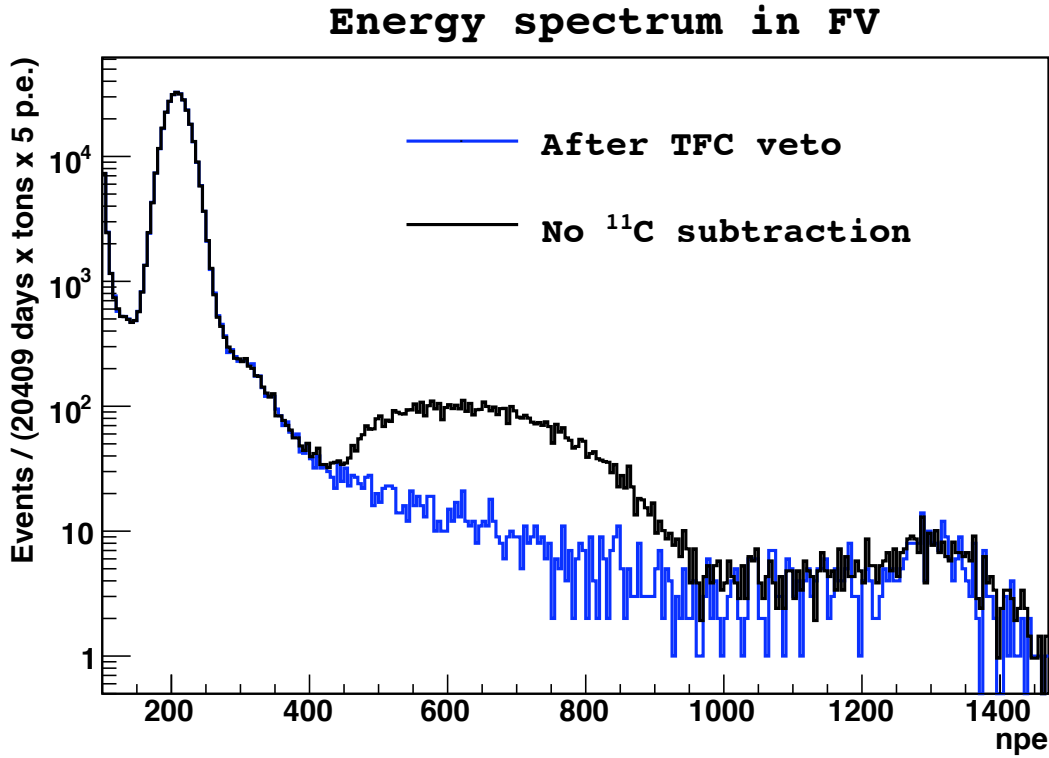


Figure 5.6: Normalized Borexino energy spectrum before and after application of techniques for ^{11}C removal. The black line shows the untreated spectrum, with ~ 28 cpd/100 tons of ^{11}C . The blue line shows the resulting spectrum after applying the three-fold coincidence veto described in Sec. 5.5.3, which decreases the ^{11}C rate to ~ 2.5 cpd/100 tons with a 51.5% loss of exposure.

5.6.1 Echidna nhits

This is the number of PMT hits in the long, fixed length (1500 ns), cluster window. After each PMT hit, there is a hardware dead time of 140 ns in the hit channel. An additional software dead time of 40 ns is applied, in order to not include spurious hits due to re-triggering. The total number of hits is then scaled by $2000/(\text{No. of PMTs with valid timing readout})$.

5.6.2 MOE npe_noavg_corrected

This is the total, summed photoelectron charge of every “valid-charge” hit, including those from re-triggered channels, within the variable-length MOE cluster. Single channel dead times are the same as those for Echidna nhits. The expected number of dark noise hits in the cluster is subtracted. The total charge is then scaled by $2000/(\text{No. of PMTs with valid charge readout})$.

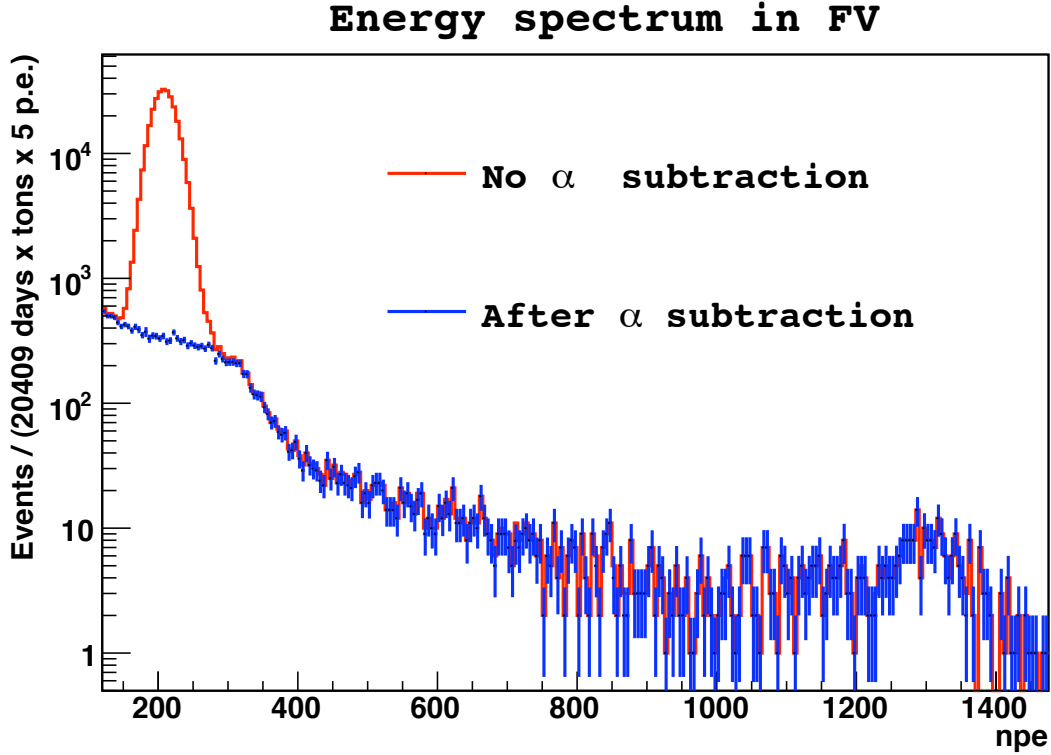


Figure 5.7: Normalized Borexino energy spectrum before and after statistical subtraction of α -like events. The red line shows the energy spectrum after applying the three-fold coincidence veto described in Sec. 5.5.3 and before α subtraction. The blue line shows the resulting spectrum after applying the α statistical subtraction technique referred in Sec. 5.5.4.

5.7 β^+/β^- pulse-shape discrimination

The ^{11}C surviving the TFC veto is still a significant background for the pep ν and CNO ν s interaction rate measurement. We developed and adopted novel data analysis techniques, exploiting the pulse shape differences between e^- and e^+ interactions in organic liquid scintillators, in order to discriminate ^{11}C β^+ decays from neutrino-induced e^- recoils and β^- decays.

5.7.1 Principles of β^+/β^- pulse-shape discrimination in liquid scintillators

The profile of the reconstructed emission times for scintillation photons produced by a positron that deposits its energy in the target should be different than those from an electron. After the positron deposits its kinetic energy, it annihilates with electrons in the scintillator emitting two back-to-back γ -rays. The time lag in the physical process of positron annihilation, as well as the fact that the energy is deposited by multiple particles, leads to differences in the reconstructed emission time of the detected photons

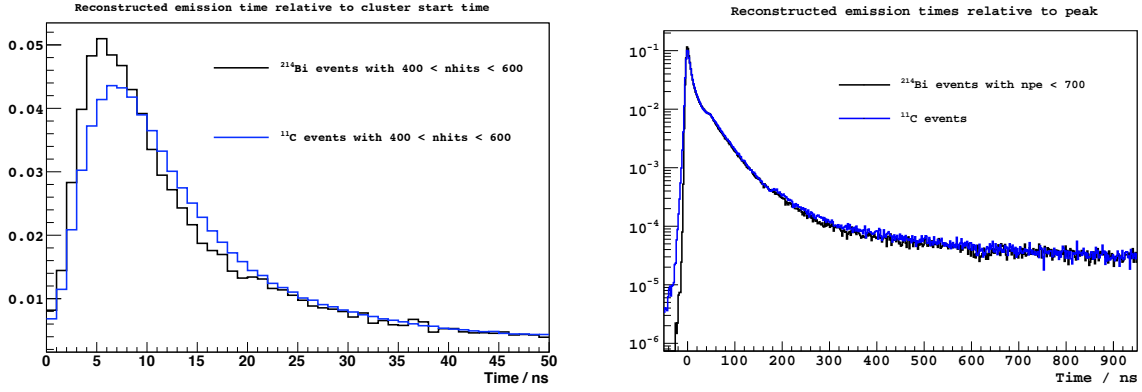


Figure 5.8: **Left panel:** Reconstructed photon emission times relative to the start time of the event for β^- events (^{214}Bi events identified from a $^{214}\text{BiPo}$ fast coincidence search) and ^{11}C events (tagged by the TFC veto) with $425 < \text{nhits} < 475$. **Right panel:** Reconstructed photon emission times for β^- events (^{214}Bi events identified from a $^{214}\text{BiPo}$ fast coincidence search) with $100 < \text{npe} < 700$ and ^{11}C events (tagged via the TFC veto) with $450 < \text{npe} < 850$. In this case, the peaks of the two distributions are aligned on the horizontal axis.

(henceforth pulse shape).

Prior to annihilation, an electron-positron pair may form an ortho-positronium (o-Ps) state, with a mean life of a few ns [121]. The finite life time of the ortho-positronium state delays the annihilation, the further energy deposit of the annihilation γ -rays, and the corresponding scintillation emission. The decay of the ortho-positronium in two γ , forbidden in vacuum, is possible in the scintillator due to the *peak off* effect: positrons, in the ortho-positronium state, are mainly captured by surrounding electrons in scintillator. The decay of the ortho-positronium is ruled by an exponential law depending on the ortho-positronium mean life. The mean time of ortho-positronium in PC+PPO mixture was measured in [121] and is ~ 3 ns while the ortho-positronium formation probability was found to be $\sim 50\%$. This mean time is comparable to the faster scintillation time constant (~ 3 ns) and therefore has a significant impact on the light pulse shape which is used to identify β^+ radioactive backgrounds. Additional distortions in the pulse shape are expected from the diffuse geometry of events resulting from the positronium decay, due to the non-null free mean path of the ensuing γ -rays.

5.7.2 β^+/β^- time profiles in Borexino

Fig. 5.8 (left) shows the distributions of the emission times (PMT hit times, once subtracted the time of flight from the reconstructed position) relative to the reconstructed time of the event for β^- events (^{214}Bi events identified from a $^{214}\text{BiPo}$ fast coincidence search) and ^{11}C events (tagged via the TFC technique) with energy $425 < \text{nhits} < 475$. Fig. 5.8 (right) also shows the reconstructed emission times relative to the peak for β^- events (^{214}Bi events identified from a $^{214}\text{BiPo}$ fast coincidence search) with $100 < \text{npe} < 700$ and ^{11}C events (tagged via the TFC technique) with energy $450 < \text{npe} < 850$; Differences

may be observed in both the peak time and the rise and decay times of the distributions.

We believe that these differences are mostly due to the delay induced by the o-Ps lifetime: when the β^+ undergoes o-Ps formation, the scintillation light produced by the two annihilation γ -rays is delayed with respect to the prompt scintillation light produced by the kinetic energy loss of the β^+ . The ratio R between the annihilation energy and the kinetic energy T of the β^+ is not constant with respect to the energy of the β^+ :

$$R = \frac{2m_e c^2}{T} \quad , \quad (5.5)$$

where $m_e c^2$ is the rest energy of electrons and positrons, and therefore $2m_e c^2$ is the energy of the 2 annihilation γ -rays. The fraction of the delayed hits induced by the o-Ps decay, respect to the total number of hits, is then lower when the kinetic energy of the β^+ is higher. The difference between β^+ and β^- reconstructed emission time, as well as the discrimination power of any pulse-shape based method, is then energy-dependent, and it is lower as the energy of the β^+ event increases.

In order to detect and quantify this effect in Borexino data, as well as to develop pulse shape variables to discriminate β^+ and β^- events, we have developed a special Monte Carlo event generator to simulate o-Ps formation and yield the corrected pulse shape (see Sec. 4.2.1.3). According to the input formation probability and lifetime, the code generates positron annihilations and positronium decays. The delay of the γ -rays follows an exponential law depending on the o-Ps mean life.

An evidence that the o-Ps is generated in a fraction of β^+ events in the Borexino data sample comes from the comparison of the pulse shape of the reconstructed photon emission times, in a pure sample of β^+ events, with respect to simulations of o-Ps pulse shape. The sample of β^+ events is provided thanks to the TFC veto, that allows high-purity sample of ^{11}C decays. We have compared the pulse shape of these events in data with the pulse shape of simulated ^{11}C decays with different o-Ps mean life and formation probability. This comparison rejected the hypothesis of no o-Ps formation in the data, and evidenced o-Ps formation with mean life and probability in agreement with the laboratory measurement in [121]. The comparison between the reconstructed emission times for ^{11}C events between real data and a simulated data sample is shown in Fig. 5.9.

5.7.3 Boosted-decision-tree analysis

We have developed a method of particle identification, based on pulse-shape discrimination, for ^{11}C events. The method utilises the Boosted Decision Tree (BDT) algorithm of the Toolkit for MultiVariate Analysis (TMVA) [142], included in the standard ROOT distribution [143]. This technique requires carefully chosen training sets of data for signal and background to build a weighted (boosted) decision tree, which optimises the cuts on a user-defined set of variables, for best identifying the signal against the background. The trained method returns a number for each event. Test event sets define a distribution of such number which the user can then use to discriminate between signal and background.

To train the BDT, we selected as the signal sample the low energy $^{214}\text{BiPo}$ events ($450 < \text{npe} < 900$), which are a relatively clean β^- sample ($\sim 95\%$ of events in 450–700

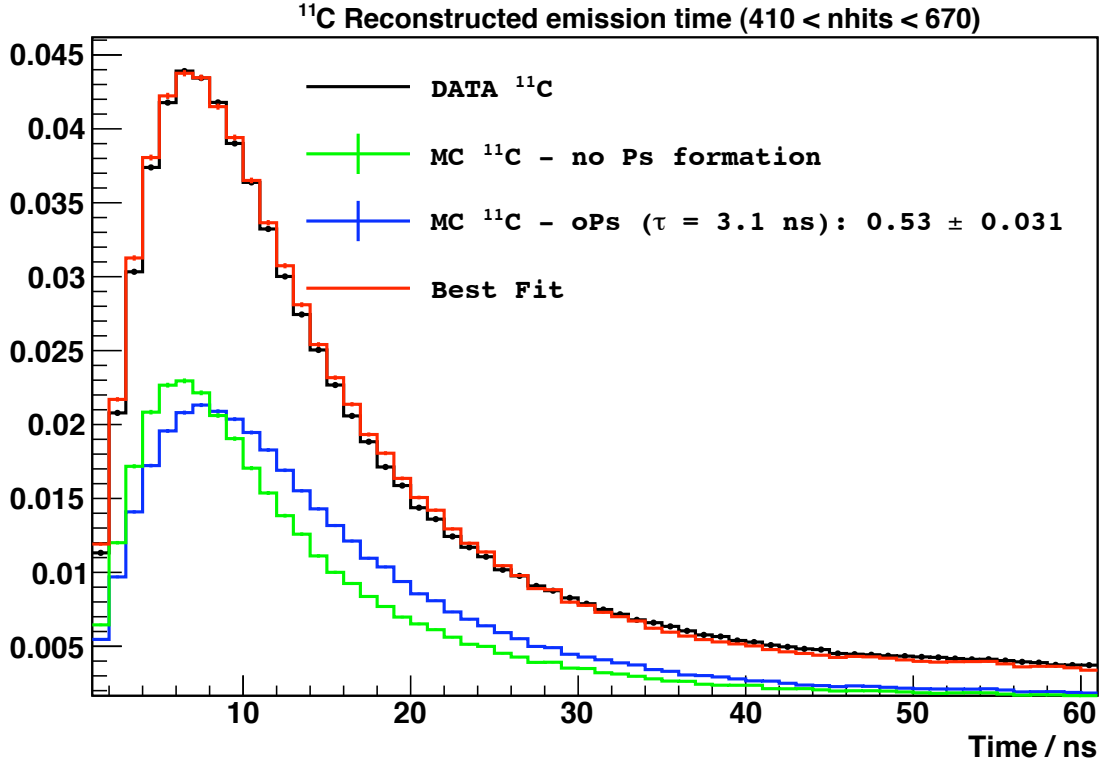


Figure 5.9: Reconstructed photon emission times for ^{11}C decays in Borexino data (black line). The ^{11}C events are tagged with the TFC veto. The data pulse shape is fitted with the sum of two Monte Carlo simulated pulse shapes of ^{11}C decays (red line), one with 100% o-Ps formation (blue line) and one without o-Ps formation (green line). In this particular trial the o-Ps mean life is 3.1 ns. The weight of the pulse shape with o-Ps formation represents the o-Ps probability formation, which is a free parameter in the fit. The fitted o-Ps formation probability (53%) and the mean life (~ 3 ns) of this trial is in agreement with the laboratory measurement in [121].

npe range are pure β^- decays, while $\sim 60\%$ of those in the range 700–900 have some γ -ray contribution). We selected as the background sample those events tagged by the three-fold coincidence with energy $450 < \text{npe} < 900$, which should be an almost pure ($> 98\%$) ^{11}C sample. All of the events considered have reconstructed positions with $r < 3 \text{ m}$ and $2.2 \text{ m} > z > -1.8 \text{ m}$, which are the z -cuts used to define the FV (Sec. 5.5.2). The training and test samples are the same size, with 1400 signal (β^-) events and 3175 background (β^+) events. The cluster variables considered by the BDT analysis are:

- The Gatti parameter (see Sec. 3.4.2) computed using as reference the ^{214}Bi and ^{11}C time profiles from real data, with reconstructed emission time relative to the peak.
- The Gatti parameter computed using as reference the ^{214}Bi and ^{11}C time profiles from real data, with reconstructed emission time relative to the cluster start.
- The Gatti parameter computed using as reference the ^{214}Bi and o-Ps (Monte

Carlo-generated) time profiles, with reconstructed emission time relative to the cluster start.

- The Gatti parameter computed using as reference the Monte Carlo-generated ^{11}C time profiles with and without o-Pos formation, with reconstructed emission time relative to the cluster start.
- The Gatti parameter computed using as reference the ^{214}Bi and ^{214}Po time profiles from data.
- The Kolmogorov-Smirnov probabilities between the emission time distribution of the event and the ^{214}Bi or ^{214}Po reference time profiles.
- The reconstructed emission time, relative to the peak of the time distribution, of the earliest hit in the cluster.
- The peak of the emission time distribution relative to the reconstructed time of the event.
- The first four moments of the emission time distribution (i.e. mean, rms, skewness and kurtosis) for hits up to $1.1\ \mu\text{s}$ after the cluster start.
- Ten tail-to-total (see Sec. 3.4.2) variables that are the fraction of the hits in the cluster after particular times (35, 70, 105, 140, 175, 210, 245, 280, 315 and 350 ns) relative to the peak of the distribution.
- The first four Legendre polynomials, averaged over all combinations, of the angle between any two hit PMTs relative to the reconstructed position of the event.
- The uncertainties in the reconstructed position along an axis (x, y, z , as returned by the fitter) divided by the mean of the other two uncertainties.
- The ratio (for all axes) of the reconstructed position of the event obtained from the time-of-flight subtraction algorithm to the charge-weighted average of the PMT positions in the event.

The final output variable of the BDT algorithm (the PS-BDT parameter) and the corresponding distribution of the test samples is shown in Fig. 5.10.

As the training and test samples are statistically independent, the probability distribution functions (PDFs) from which the PS-BDT parameter distributions for the test samples are drawn should be the same as those for the final candidates, as long as they belong to the same population of events. The probability of the ^{11}C decay to be selected by a TFC veto should be independent on the details of the decay, including the energy of the positron emitted and the probability that it forms ortho-positronium, and, therefore, the test sample for the β^+ should have the same distribution in energy and all variables included in the computation of the PS-BDT parameter as the ^{11}C decays in the final data sample. The efficiency in the TFC tagging has been observed to be spatially uniform up to 2.8 m from the centre of the detector (Sec. 5.5.3). For the training candidate sample of the PS-BDT parameter we have included events up

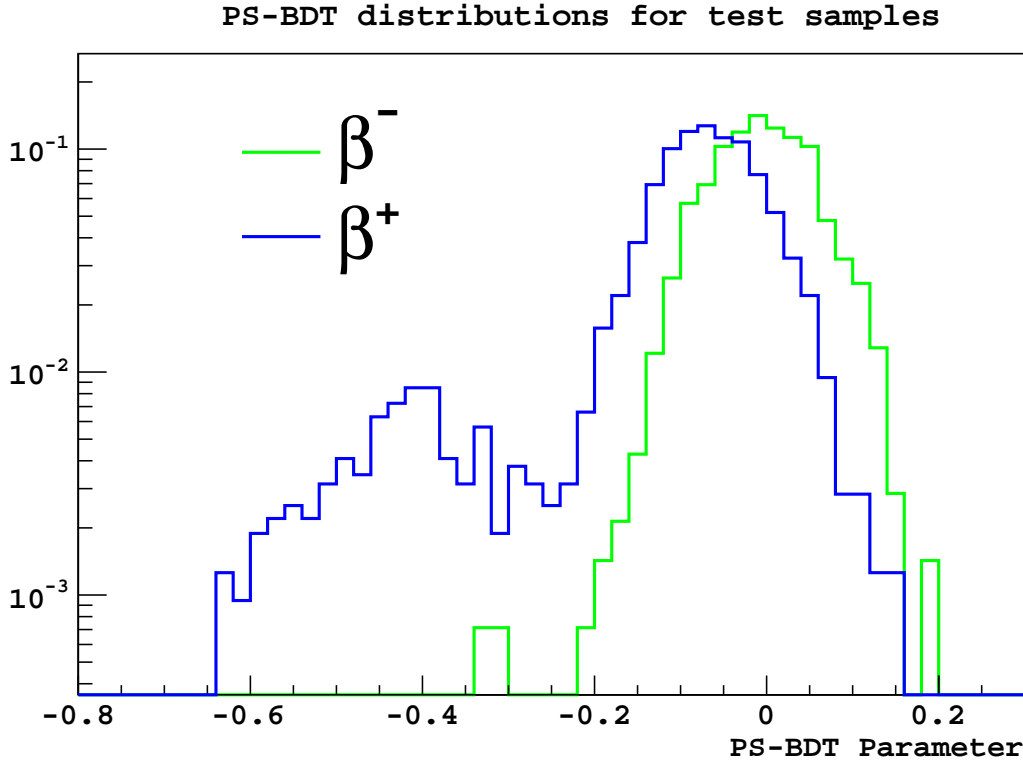


Figure 5.10: Distributions of the PS-BDT parameter for the test samples of β^- (green line) and β^+ (blue line) events. β^- are low energy (< 900 npe) ^{214}Bi events selected from fast $^{214}\text{BiPo}$ coincidences. β^+ events are ^{11}C events tagged via the TFC technique described in Sec. 5.5.3. The training was performed using ROOT's Toolkit for MultiVariate Analysis and the pulse shape cluster variables listed in Sec. 5.7.3.

to 3 m but, as we observed no noticeable dependence of the PS-BDT parameter on reconstructed radial position and, we do not expect any differences between the test sample distribution and that of the ^{11}C decays in the final candidates sample.

The differences between the test sample and the β^- events in the final candidates are larger. Not only is the test sample itself composed of some events that have some γ -ray contribution, but in the final candidates there should also be some external γ -rays. The profile is similar in both cases, with γ -ray contributions increasing towards higher energies, yet the relative composition as a function of energy has not been shown to be identical. We have argued that the largest difference between the pulse shape of β^+ and β^- events is due to the delayed γ -rays from the formation of ortho-positronium, but we have also acknowledged that the diffuse nature of the energy deposits in the β^+ decay, which may be similar to those from single γ -rays, could also lead to pulse-shape differences (Sec. 5.7.1). As mentioned earlier, the γ -ray contribution to the ^{214}Bi sample starts at ~ 700 npe and therefore, if the increase in the γ -ray content has an effect in the PS-BDT parameter, we may see a change in the distribution after this point. Fig. 5.11 (right) shows the energy dependence of the mean value of the PS-BDT parameter for both ^{11}C and ^{214}Bi test samples. As may be observed, there is indeed an increase in

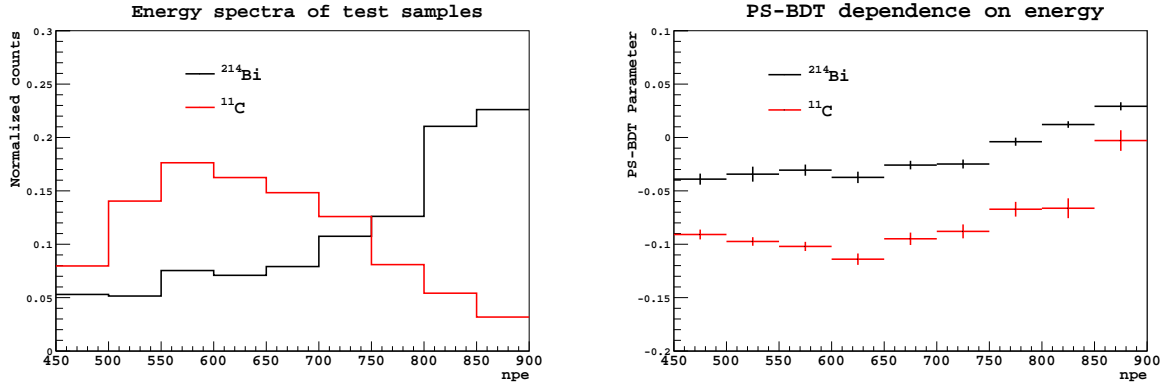


Figure 5.11: **Left panel:** Energy spectrum for the events in the ^{11}C (β^+) and low energy ^{214}Bi (β^-) test samples. **Right panel:** Mean value for the PS-BDT distribution in the corresponding npe bin. For both test samples, the PS-BDT value increases at higher energies. The energy dependence of the parameter will not lead to any differences between the PS-BDT distributions of a test sub-sample and the corresponding events in the final candidates sample, as long as the energy spectrum does not differ considerably in the energy range of the events in the distribution.

the PS-BDT mean at higher energies, but this effect is present in both test samples, which suggests that it is due to an overall dependence of the PS-BDT parameter on the energy and not necessarily correlated with the increase in the γ -ray contribution in the ^{214}Bi sample. The energy dependence itself should not be a problem for our analysis, as long as the energy bins for the PS-BDT distributions that we consider are small enough such that neither the PS-BDT mean values nor the energy spectra for the test and final samples differ considerably throughout them. In Sec. 5.10.3.6 we perform an evaluation of the systematic uncertainty induced by these issues.

Additionally, the spatial distribution of the events in the ^{214}Bi sample is not the same as the β^- events in the final candidates. The ^{214}Bi events selected are decay products of ^{222}Rn , which has been mostly introduced into the detector during operations (from the top) or has been emanated by the nylon vessels, leading to a non-uniform spatial distribution. Furthermore, some of the events in the final candidates considered β^- are external γ -rays, whose position is preferentially reconstructed towards the edge of the FV. Fig. 5.12 (right) show the relationship between the ^{214}Bi PS-BDT parameter and the reconstructed z event coordinate. Fits to the mean values of the PS-BDT distributions as a function of both r and z are consistent with the PS-BDT parameter being independent on position (p-values of 0.5 when fit to a constant), suggesting that no considerable differences are introduced in the PS-BDT distributions due to the differences in the spatial distribution of the test and final candidates samples.

5.8 Radial and energy distributions of external γ -ray background

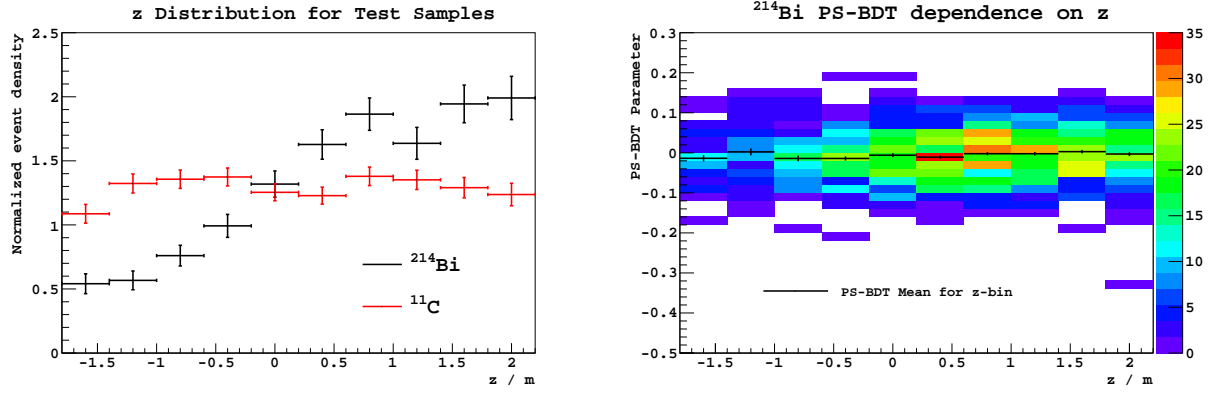


Figure 5.12: **Left panel:** Spatial density for the events in the test samples as a function of z . TFC-tagged ^{11}C events (β^+ test sample) have a uniform distribution, while the low energy ^{214}Bi events (β^- test sample) are found preferentially in the top of the detector. **Right panel:** Relationship between the PS-BDT parameter and the reconstructed z position for the events in the low energy ^{214}Bi test sample. The color scale represents the number of events that fall within the two-dimensional histogram bin. The black markers show the mean value of the PS-BDT parameter for the events in the corresponding z -bin. No z dependence of the PS-BDT parameter is observed.

5.8 Radial and energy distributions of external γ -ray background

As described in [137] and reported in Sec. 5.3, the SSS, the PMTs and the light concentrators are contaminated with considerable amounts of ^{232}Th , ^{238}U and ^{40}K . Mainly the long-ranged γ -rays from the daughter nuclides ^{208}Tl (2.61 MeV) and ^{214}Bi (up to 3.27 MeV) contribute to the external background observed in the inner part of the detector. External source calibration of the detector and the development of a special Monte Carlo simulation procedure for the background coming from the PMTs were necessary to generate and validate radial and energy distributions of the γ -ray background required for this analysis.

The external calibration was performed using a ~ 5 MBq custom-made ^{228}Th source [124, 125]. ^{228}Th was selected due to its long half-life ($\tau_{1/2} = 1.9$ years) and the fact that one of its daughter nuclides, ^{208}Tl , emits the characteristic 2.61 MeV γ -rays dominating the external background observed in Borexino. During the first external calibration campaign, the ^{228}Th source was deployed in two positions close to the SSS, one in the top and one in the bottom hemisphere of the detector.

Taking into account the attenuation length of about 23 cm estimated from the calibration data, the rate of external γ -rays is strongly reduced by a factor of 10^7 within a radius of 3 m. The spectral analysis requires the simulation of a sample of $\sim 10^4$ γ -rays in the FV, thus approximately 10^{12} primary events had to be generated. In order to speed up the time-consuming simulation, several actions have been taken:

- Primary events are simulated on a sphere of 6.5 m radius (corresponding to the PMT photocathode surface).

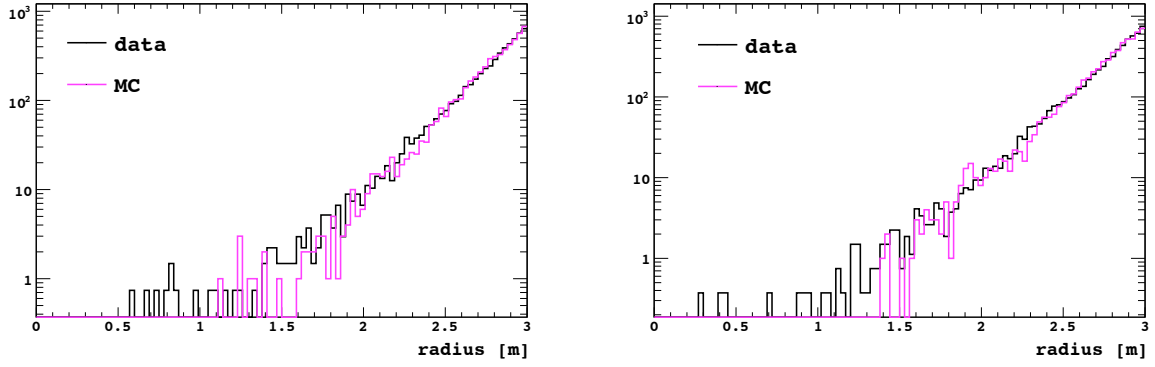


Figure 5.13: Comparison between the reconstructed position of events with energy > 400 nhits from the calibration data (black line) and the 2.61 MeV simulated external γ -rays (pink line), surviving within 3 m from the centre of the detector, for the source positions in the top (left panel) and bottom (right panel) hemispheres. The χ^2/ndf between the two histograms (Monte Carlo and data) is $\sim 0.8\text{--}0.9$.

- Only those γ -rays directed towards the IV (emission angle limits: $-33^\circ < \theta < 33^\circ$) are simulated.
- As a first step, the optical processes (such as scintillation and Cherenkov light generation) are deactivated and all information concerning the energy deposition, the vertex position and the direction of the particle are written to a binary file.
- If, for a simulated event, the sum of the energy deposited exceeds 200 keV and lies within 3.2 m from the centre of the detector, an electron is generated for each γ -ray energy deposit. Then, the electron is propagated with the corresponding starting energy, position and direction and all optical processes are simulated.

This way, the CPU time required for the simulation of the first step for a single events is $\sim 5 \times 10^{-5}$ s and for the second step $\sim 9 \times 10^{-6}$ s. Finally, the detector electronics simulation is performed and its output, whose format is the same as the raw data, is processed with the full reconstruction software (see Chapter 4).

In order to validate the external background simulations, a simulation of the point-like external γ -ray source has been performed and compared with the calibration data. As shown in Fig. 5.13 and 5.14, the energy and reconstructed position of the simulated events in both the top and bottom hemispheres are in agreement with data at the 99.5% level.

5.9 Fitting procedure

The fitting procedure performed in this analysis is described in this session. The rates (or limits) for neutrino and background components are obtained with a binned multivariate likelihood fit. Information from the energy spectrum (Sec.5.5, Sec.5.9.2), pulse-shape BDT parameter (Sec.5.7, Sec.5.9.3), and radial distribution of the events (Sec. 5.8,

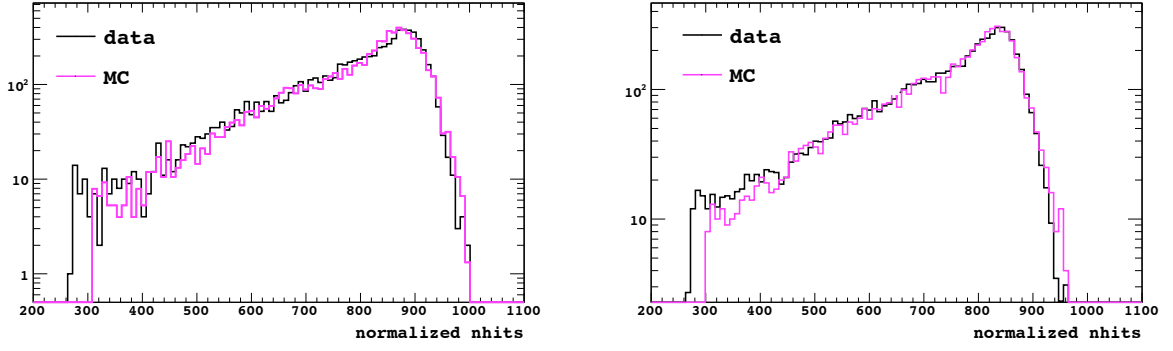


Figure 5.14: Comparison between the reconstructed nhits for events from the calibration data (black line) and the 2.61 MeV simulated external γ -rays (pink line), surviving within 3 m from the centre of the detector, for the source positions in the top (left panel) and bottom (right panel) hemispheres. The χ^2/ndf between the two histograms (Monte Carlo and data) is ~ 1.2 .

Sec. 5.9.4) are included in the likelihood (Sec. 5.9.1) to maximise. The ^{11}C subtracted energy spectrum (Sec 5.5.3) and its complementary (TFC-vetoed) spectrum are fitted simultaneously. The fit method has been validated using data-like samples of known input composition (Sec. 5.10.2).

5.9.1 Multi-dimensional fitting strategy

The method of maximum likelihood (see Sec. 33.1.2 in [2]) is used in the *pep* ν analysis to fit the data. The likelihood was chosen as test statistic for two reasons:

- the small number of entries in some of the high energy bins of our final energy spectrum;
- the possibility to extend the likelihood in a multi-dimensional approach, in order to include the β^+ / β^- pulse-shape BDT parameter (Sec. 5.7) and the radial distribution of the events (Sec. 5.8) in the likelihood to maximise.

For a one-dimensional fit, one would compute the Poisson likelihood, L , of a hypothesis (i.e. the likelihood that the data fits a test spectrum with a set of parameters $\vec{\theta}$) as

$$L(\vec{\theta}) = \prod_{i=1}^n \frac{\lambda_i(\vec{\theta})^{k_i} e^{-\lambda_i(\vec{\theta})}}{k_i!} \quad (5.6)$$

where the product is over all bins and n is the total number of bins. $\lambda_i(\vec{\theta})$ is the expected number of entries in the i th bin given the fit parameters ($\vec{\theta}$) and k_i is the number of entries in the bin. As an example, k_i could be the number of entries in a particular energy bin, and $\lambda(\vec{\theta})$ the expected number of entries in that bin given the rates of each species described by the array of parameter θ .

For the *pep* ν analysis, in order to constrain the impact of the background due to ^{11}C decays and the external γ -rays, the likelihood is extended to other variables, namely, the pulse-shape BDT parameter (Sec. 5.7) and the radial distribution (Sec. 5.8) of the events. The probability density functions (PDFs) of some of these variables are produced from data (e.g. the pulse-shape PDF for β^- is taken from tagged $^{214}\text{BiPo}$ events) and we do not have neither very high statistics, nor an analytical model to produce precise multi-dimensional PDFs. Therefore, the events are projected and integrated over an energy range larger than the energy spectrum binning, into one-dimensional histograms of the other variables, and the corresponding likelihood is computed. In this case though, a correlation between the number of counts in the different histograms is introduced, as events that are in the energy spectrum will also be entries in the projections. To handle this issue, the PDFs of the hypothesis are normalized to the total number of entries in the projected data histograms. Consequently, the likelihood computed for the projections is defined as:

$$L_p(\vec{\theta}) = \prod_{j=1}^m \frac{a \lambda_j(\vec{\theta})^{k_j} e^{-a \lambda_j(\vec{\theta})}}{k_j!} \quad (5.7)$$

$$N = a \sum_{j=1}^m \lambda_j(\vec{\theta}) \quad (5.8)$$

where N is the total number of entries in the projected histogram and a is a scaling factor set to satisfy Eq. 5.8. Here $\lambda_j(\vec{\theta})$ represents the expected bin content of the projected histogram in the corresponding other variable, and k_j is the actual number of entries in that bin. The scaling does not affect the values of $\lambda(\vec{\theta})$ at the maximum likelihood but the uncertainties given by likelihood ratio tests may not be underestimated, as it is the case when the scaling is not done. Even though we have not demonstrated that this procedure is mathematically sound, in Sec. 5.10.2 we perform MonteCarlo tests with data-like samples to show that the statistical interpretation of likelihood ratio tests holds for the computed total likelihood.

The total likelihood to maximise is then

$$L_T(\vec{\theta}) = \prod_{i=1}^{m_E} L(\vec{\theta}) \times \prod_{j=1}^{m_p} L_p(\vec{\theta}) \quad (5.9)$$

where $L(\vec{\theta})$ and $L_p(\vec{\theta})$ are defined in Eq. 5.6 and 5.7, respectively. The first product is over the m_E independent energy spectra (e.g. those of the TFC-tagged and TFC-subtracted events, see Sec. 5.9.2) and the second is the product over all m_p projections to other dimensions (e.g. radial distribution and PS-BDT parameter space) of regions of one of the energy spectra. This definition has been implemented into the fitting code, which pass $-\ln L_T(\vec{\theta})$ to MINUIT as the test statistic to be minimised.

As we are using PDFs from data with limited statistics for the fit to the PS-BDT parameter space, we have had to introduce a correction to handle the possibility of there being an event in a bin for which there are no events in the corresponding fitting PDF, not because the true λ_i is zero, but because of the limited statistics. This effect is reduced greatly since a “smoothing” is applied to the fitting PDFs (Sec. 5.9.3), increasing

the statistics significantly and filling up empty bins. The detailed explanation of the modification will be omitted here as it comes from a redefinition of the likelihood for which its total value is almost identical to the one obtained from Eq. 5.9, except for the case where $\lambda_i = 0$ and $k_i > 0$. In such case, the likelihood for the bin becomes

$$L_i = \left(\frac{N}{N_{PDF} + n} \right)^{k_i} \quad (5.10)$$

where n is the number of bins in the histogram and N and N_{PDF} are the entries in the projected histogram and the fitting PDF, respectively. The probability computed by this method, albeit small as generally $N_{PDF} \gg N$, is non-zero and, therefore, can be handled appropriately by the fitter.

For this analysis, we have not made any particular corrections to the likelihood for the bins over which the bin contents (and their corresponding uncertainties) have been changed by the statistical α subtraction procedure (Sec. 5.5.4). Generally, the uncertainties remain unchanged except for the region of the ^{210}Po peak (150–250 npe). For example, in the case of the npe spectrum, out of 146 bins, only 18 had an increase in uncertainty $> 5\%$ and only 5 had an increase $> 15\%$. Not considering this increase in the uncertainty will not affect the best fit value (i.e. the values of $\lambda(\vec{\theta})$ for which the maximum likelihood is found), but may have a small effect in the uncertainty returned by the fit for species determined by this region of the spectrum, namely ^7Be , ^{85}Kr and ^{210}Bi .

5.9.2 Fit to the energy spectra

5.9.2.1 Subtracted and complementary energy spectrum fit

We have applied a binned likelihood fit to the energy spectra obtained from the event selection outlined in Sec. 5.5. Both the TFC-subtracted spectrum and its complementary spectrum are fitted simultaneously, keeping the rates of most species as common parameters (see Table 5.7). The only species whose rates are different parameters in the two spectra are ^{11}C , ^{10}C and ^6He . The ^{11}C rate is indeed suppressed by the TFC, as it is correlated with neutron production (Sec. 5.5.3). ^{10}C and ^6He are also cosmogenic in nature and their production may also be correlated with neutrons, therefore their rates are kept independent in the two spectra.

5.9.2.2 Input energy spectra

In order to check for consistency within our assumptions and to get an evaluation of the systematics involved with the energy detector response function, we use two different energy variables to fit the energy spectrum. The energy variables used are nhits and m4charge_noavg (npe), whose descriptions are in Sec. 5.6. The energy spectrum PDFs used to fit the nhits and m4charge_noavg (npe) spectra have been produced with independent methods: the PDFs for nhits have been obtained with the full Monte Carlo simulation of the Borexino detector (see Chapter 4), while the PDFs for m4charge_noavg (npe) are based on an analytical model of the detector response.

Species	Rate free or fixed	Common	In PS-BDT fit	In radial dist. fit
<i>pep</i> ν	free	Yes	β^-	Bulk
CNO ν s	free	Yes	β^-	Bulk*
^7Be ν	free	Yes	β^-^*	Bulk*
<i>pp</i>	fixed (133 cpd/100t)	Yes	β^-^*	Bulk*
^8B ν	fixed (0.46 cpd/100t)	Yes	β^-	Bulk
^{214}Pb	fixed (1.95 cpd/100t)	Yes	β^-	Bulk*
^{210}Bi	free	Yes	β^-	Bulk*
^{10}C	free	No	β^+	Bulk
^{11}C	free	No	β^+	Bulk
Ext. ^{214}Bi	free	Yes	β^-	External
Ext. ^{40}K	free	Yes	β^-	External
Ext. ^{208}Tl	free	Yes	β^-	External
^6He	free	No	β^-	Bulk
^{40}K	free	Yes	β^-	Bulk
^{85}Kr	free	Yes	β^-^*	Bulk*
^{234m}Pa	free	Yes	β^-	Bulk

Table 5.7: Background and neutrino species considered in the fit. The *pp* ν and ^8B ν interaction rates have been fixed to the central values from the High-Z solar model [60]. The value for ^{214}Pb was estimated to be 1.95 ± 0.07 cpd/100tons from the $^{214}\text{BiPo}$ rate obtained from the fast coincidence search in the analysis exposure. The third column refers to whether the rates for a species in both the TFC-subtracted and TFC-tagged spectra are a single parameter. The last two columns show if the species is considered signal or background in the simultaneous fits to the pulse shape BDT parameter (Sec. 5.9.3) and the radial distribution of the events in the FV (Sec. 5.9.4). The asterisk (*) denotes species that, due to the energy range considered for the fits in the PS-BDT or radial position dimensions, are effectively excluded from the corresponding fit.

The PDFs for nhits spectrum are obtained using a Monte Carlo ab initio simulation of all the process in the detector, including particle energy loss, scintillation and Cherenkov photon generation, optical photon propagation and detection, and the response of the electronics, as described in Chapter 4. The electronic simulation code reproduces as close as possible the real behaviour of the detector, following the pattern of working PMTs both in time and in charge, the number of PMTs disabled during each run, the real gain of each PMT, and the dark noise (see Sec. 4.2.6). The resulting spectrum automatically incorporates the simulated energy response of the detector. The simulated raw data are then processed with the same tools used to decode and reconstruct the real data. The Standard Cuts (Sec. 5.5.1) are then applied to the simulated data. More information on the Monte Carlo simulation of Borexino can be found in Chapter 4 and the PhD thesis [118].

The PDFs for the m4charge_noavg (npe) are produced by the fitter starting with the β energy spectrum (or γ -ray energy). The relationship between the energy of a β or γ -ray and its mean value in the m4charge_noavg (npe) scale was calibrated in the context of the ${}^7\text{Be}$ ν analysis [25]. After the energy spectrum has been translated to m4charge_noavg (npe), the detector response is applied. Details of this procedure can be found in the PhD thesis [119]. For the energy spectra of the external background species, we rely on the visible energy spectrum from g4bx (Sec. 5.8) and convert it to a β -equivalent energy spectrum using our analytical model for the scintillator energy response, so that it can be treated by the fitter as a continuous β spectrum. As the spectra are computed by the fitter itself, some of the energy response parameters may be left free in the fit. These include the absolute detector light yield, the relative light yield for external background species, the starting point of the ${}^{11}\text{C}$ spectrum (the spectral feature that is most sensitive to non-linear quenching effects in the scintillator) and the resolution parameters for the modified Gaussian used in the modelling of the detector response.

5.9.2.3 Energy calibration

The energy calibration of the nhits and m4charge_noavg (npe) PDFs are based on the detector calibration campaign (in particular, the γ -ray sources ${}^{203}\text{Hg}$, ${}^{85}\text{Sr}$, ${}^{54}\text{Mn}$, ${}^{65}\text{Zn}$, ${}^{40}\text{K}$, ${}^{60}\text{Co}$), which provide a clean sample of data that has been used to:

- Check the accuracy of the results from the Monte Carlo code, and tune the values of some unknown parameters (in particular, to find the best value for the photon yield and the Birk's quenching factor);
- Fit to the parameters in the quenching and electronics analytical models used to translate the β energy to detected m4charge_noavg (npe).

Additionally, for the Monte Carlo, the photon yield has then been rescaled by +0.8% to match the central value of the TFC-tagged ${}^{11}\text{C}$ spectrum in the FV used in this analysis. The absolute light yield for the Monte Carlo nhits spectrum is ~ 430 nhits/MeV. More information on the calibration Monte Carlo simulation of Borexino can be found in Sec. 4.3.3 and in the PhD thesis [118].

Background	Source (npe spectrum)	Source (nhits spectrum)
^{85}Kr	Table of Isotopes	GeNeb
^{210}Bi	[144]	SCS, [144]
^{11}C	Table of Isotopes	RDM
^{10}C	Table of Isotopes	RDM
^{214}Pb	Table of Isotopes	RDM
Ext. ^{208}Tl	g4bx-RDM	g4bx-RDM
Ext. ^{214}Bi	g4bx-RDM	g4bx-RDM
Ext. ^{40}K	g4bx - Table of Isotopes	g4bx - Table of Isotopes
^{40}K	3 rd Forbidden correction	GeNeb
^{234m}Pa	Table of isotopes	GeNeb
^6He	Table of isotopes	RDM

Table 5.8: Input energy spectrum for backgrounds. See Sec. 5.9.2.2 for the procedure to generate the fitting PDFs from these spectra. More details on the GeNeb, RDM and SCS generators can be found in Sec. 4.2.1.2 and in the Borexino internal note [130]. Detailed references for the input energy spectra and shape factors used to create the npe spectra can be found in the PhD thesis [119]. More details on the external background generation can be found in Sec. 5.8.

The precise energy calibration of the `m4charge_noavg` (npe) variable has been performed for the ^7Be ν analysis [25]. The details may be found in the PhD thesis [119]. The systematic uncertainties in the fit results due to energy scale calibration are discussed in Sec. 5.10.3.

5.9.2.4 Neutrino energy spectra

The neutrino energy spectra are calculated using the oscillation parameters $\Delta m^2 = 7.59 \times 10^{-5} \text{ eV}^2$ and $\sin^2(2\theta) = 0.87$ [2]. The electron neutrino survival probability (P_{ee}) is calculated in the framework of the LMA-MSW oscillations (see Sec. 2.7). The Sun matter effects for the nhits spectra are computed according to [128]. For the npe spectrum, radiative corrections in the neutrino-electron elastic scattering are considered [104]. Inclusion of these corrections and Earth matter effects, as well as changing the oscillation parameters (within their uncertainties), leads to negligible differences in the energy spectra (see Sec. 5.2). The CNO ν s are treated as a single spectrum, as discussed in Sec. 5.2.

5.9.2.5 Background energy spectra

An estimate of all the relevant backgrounds is discussed in Sec. 5.3. Table 5.8 lists the background energy spectra included in the fit.

Parameter	npe variable	nhits variable
Bin width	10 npe	5 nhits
Fit range	160–1600 npe	145–950 nhits
Resolution	fixed	fixed
Light Yield	fixed - 500.28 pe/MeV	fixed - 430 nhits/MeV
Quenching model	fixed	fixed

Table 5.9: Configuration of the energy fit. The resolution, ^{11}C starting point and relative light yield for external background species in the npe fit were obtained from a fit to the spectrum of TFC-tagged events without any statistical α subtraction, for details see Sec. 5.9.2.3. The absolute light yield for the npe fit has been fixed to the best-fit value when the full fit is performed with the light yield parameter free (500.28 pe/MeV). The nhits spectrum automatically incorporates the simulated energy response of the detector. The absolute light yield from the nhits spectrum is ~ 430 nhits/MeV.

5.9.2.6 Configuration of the energy fit

Table 5.9 shows the standard configuration of parameters for the energy fit. To facilitate the comparison between the nhits and npe fit results and uncertainties, the absolute light yield in the npe fit is fixed to the best-fit central value obtained when the light yield is left free, 500.28 pe/MeV, and its associated uncertainty is treated separately (Sec. 5.10.3.3). The stability of the fit under small variations in the configuration, and the related systematic uncertainty are discussed in Sec. 5.10.3.

5.9.3 Fit to the β^+/β^- pulse-shape parameter.

Table 5.10 shows the standard configuration of parameter for the multivariate β^+/β^- PS-BDT fit. The bin width corresponds to the size of the region over which the TFC-subtracted energy spectrum is projected into the PS-BDT dimension. In either case, there are five one-dimensional projections to be fit. Two PDFs are used, one corresponding to the signal (β^-) and another corresponding to the background (β^+). The PDFs are constructed for every energy region from the test samples shown in Fig. 5.7.3. This construction includes a kernel “smoothing”, which is applied by simulating, for every event in the original test sample, 200 events distributed with a Gaussian whose mean is the value of the original event and whose sigma is the bin width of the PDF histogram. To obtain the amplitude for each PDF in a particular energy region, before the normalization discussed in Sec. 5.9.1, the energy spectra for the signal and background species are integrated over that region. In this case, the background (β^+) species are ^{11}C and ^{10}C , while all other species are considered signal (β^-) (see Table 5.7). The stability of the fit under variations in the configuration and the related systematic uncertainty is discussed in Sec. 5.10.3.

Parameter	npe variable	nhits variable
Bin width	90 npe	50 nhits
Energy range	450-900 npe	400-650 nhits
Smoothing	200	200

Table 5.10: Configuration of the β^+/β^- pulse shape fit. The energy range considered for the fit is set by the energy range of the ^{11}C spectrum, as the β^+ PDF is made from the TFC-tagged subsample of it.

Parameter	npe variable	nhits variable
Bin width	50 npe	25 nhits
Energy range	600-1400 npe	500-900 nhits
Smoothing	0	0

Table 5.11: Configuration of the radial distribution fit. The lower bound for the energy range is set by the decision to exclude ^{210}Bi from the fit, as its spatial distribution is probably not uniform. The upper bound is set by the statistics of the simulation, as the highest energy γ -ray simulated was the 2.61 MeV γ -ray from ^{208}Tl , whose statistics decrease rapidly for energies greater than the full energy peak.

5.9.4 Fit to the reconstructed radial position

Table 5.11 shows the standard parameter configuration for the multivariate radial distribution fit. Here the procedure is very similar to the one described in Sec 5.9.3, except that the background species are the external contributions from ^{208}Tl , ^{214}Bi and ^{40}K , while all other species are considered signal (bulk events) (see Table 5.7). The PDFs used are also energy dependent, corresponding to the particular energy regions, but are generated from Monte Carlo (Sec. 5.8) and, as the statistics are sufficient, no smoothing is performed. We have chosen the lowest energy for the events to be considered for the fit based on the end-point of the ^{210}Bi spectrum. The rate from this species has been increasing since the start of Borexino (see the PhD thesis [119]) and, as it is not spontaneously created in the scintillator but it is presumably coming into the FV from somewhere, we do not expect its spatial distribution to be uniform and, therefore, we exclude it from the fit. The included species (Table 5.7) are all expected to be distributed uniformly. The distribution of ^{11}C has been shown to be uniform within 3 m from the centre of the detector [119] and we expect the other cosmogenic isotopes ^{10}C and ^6He to be no different. Likewise ^{40}K and ^{234m}Pa , which come from permanent contaminations in the scintillator, should have uniform spatial distributions. The stability of the fit under small variations in the configuration, and the related systematic uncertainty is discussed in Sec. 5.10.3.

5.10 Results

5.10.1 Fit result

The final fit result for the energy spectra are shown in Fig. 5.15 and 5.16, while the corresponding best fits for the pulse-shape and radial distributions are shown in Fig. 5.17 and 5.18, respectively. Fig. 5.19 shows the $\Delta\chi^2$ profiles as a function of both *pep* ν and CNO νs interaction rates. The returned minimised $-\ln L$ values by the fit are in good agreement with expectations (Sec. 5.10.2). Table 5.12 summarises the mean values, limits and statistical and systematic uncertainties (Sec. 5.10.3). As may be observed from the table, in both fits the CNO νs interaction rate is nailed to zero. Therefore, we have performed a likelihood ratio test (validated in Sec. 5.10.2) to estimate the upper limits. Finally, Fig. 5.20 (left) shows the $\Delta\chi^2$ profile from which these values have been obtained. Fig. 5.21 presents the best fit value for the *pep* ν interaction rate when the CNO νs interaction rate is fixed at different values and Fig 5.20 (right) shows the $\Delta\chi^2$ profile for the *pep* ν interaction rates.

As may be observed in Fig. 5.15 and 5.16, the ^{11}C , ^{10}C and ^6He rates are much smaller in the spectrum of events after the TFC veto, as expected (Sec. 5.5.3). With the results from the fit we can estimate the fraction of ^{11}C background after the veto to be 0.094 ± 0.009 .

The last column of Table 5.12 shows the expected rates for the fit species based on other sources. For the *pep* ν and CNO νs interaction rates, the results are consistent with the expectations from both the High-Z and Low-Z SSMs. The results for the cosmogenic isotopes ^{10}C and ^6He are also consistent with those obtained from extrapolations from KamLAND data (Sec. 5.3.2) and the value for ^{85}Kr is $\sim 2\sigma$ away from the one measured by the delayed coincidence method. The upper limits on the ^{234m}Pa rate are lower than the expected value calculated from the ^{238}U contamination in the detector (Sec. 5.3.1). We note, though, that in the measurement of the ^{238}U contamination, certain assumptions have been made regarding which and what fraction of the $^{214}\text{BiPo}$ candidates are in secular equilibrium with ^{238}U . Yet, as $^{214}\text{BiPo}$ is much further down the decay chain than ^{234m}Pa and can enter the fiducial volume, not only from ^{222}Rn emanated by the vessels or from outside sources, but also from an original contamination of ^{226}Ra in the scintillator, this value could be overestimated.

The measurement of the external background rates are at least a factor of 5 lower than the expectations. The γ -ray propagation from the PMTs to the FV by the Monte Carlo has been validated with the external radioactive source (Sec. 5.8) and, therefore, we suspect that this disagreement is associated with the measurement of the radioactivity of the PMT components in [137]. Additionally, there is a $\sim 1\sigma$ difference between the values obtained for the ^7Be ν interaction and ^{11}C decay rates between this analysis and the ^7Be ν analysis [25]. This may be larger than expected, as the data sets used in the two analyses have most events in common and, therefore, are strongly correlated. For the ^7Be ν interaction rate, the discrepancy may be systematic, as the procedure to select the central value (i.e. decide which fit configuration to consider "standard") was different. The systematic checks in Sec. 5.10.4.1 and 5.10.4.2 clarify this issue. As for ^{11}C , its production is cosmogenic and, therefore, its rate is not only time dependent but also driven by high multiplicity events, making it much more sensitive to differences

Component	Central Value cpd/100 tons	Statistical Unc. cpd/100tons	Systematic Unc. cpd/100tons	Expected value cpd/100tons
<i>pep</i> ν	3.13	0.55	0.30	2.80 ± 0.04
^7Be ν	48.3	2.0	0.9	$46.0 \pm 1.5 \pm 1.6$
^{85}Kr	19.3	2.0	1.9	$30.4 \pm 5.3 \pm 1.3$
^{210}Bi	54.5	2.4	1.4	NA
^{11}C	27.4	0.3	0.1	$28.5 \pm 0.2 \pm 0.7$
^{10}C	0.62	0.2	0.1	0.54 ± 0.04
^6He	0.7 (0)	0.6 (0.5)	1	0.31 ± 0.04
Ext. ^{208}Tl	1.64 (1.94)	0.11 (0.13)	0.01 (0.02)	> 5.7
Ext. ^{214}Bi	0.67 (0.41)	0.12 (0.13)	0.01 (0.02)	> 6.6
Ext. ^{40}K	0.16	0.12	0.03	> 0.2
Tot. Ext. γ	2.49	0.2	0.03	> 12.5
	68% Limit	95% Limit	99% Limit	
CNO νs	4	12	19	5.4 ± 0.8 ($3.8^{+0.6}_{-0.5}$)
^{40}K	0.11	0.42	0.69	NA
^{234m}Pa	0.12	0.46	0.75	1.78 ± 0.06

Table 5.12: Table summarising the final results and their corresponding uncertainties. The statistical uncertainty is the one returned by the fitter, which has been validated for the *pep* ν interaction rate in Sec. 5.10.2. For ^{210}Bi , the symmetric uncertainty returned by the fitter does not represent well the $\Delta\chi^2$ profile, as can be suspected from the strong correlation with the CNO ν s interaction rate (Fig. 5.22). For species that are fit to zero, the upper confidence limits are obtained from the $\Delta\chi^2$ profile, as in Fig. 5.20 for CNO ν s. The total systematic uncertainty has been obtained following the methodology outlined in Sec. 5.10.3. Differences between best-fit rates from the npe and nhits fits have been included within the systematic uncertainty, except for external ^{208}Tl and ^{214}Bi , for which the rates and uncertainties are given separately i.e. npe (nhits). For the case of ^6He , its central value is zero in the nhits fit and the number given in parentheses for the uncertainty is the 68% U.L., while the corresponding 95% U.L. is 1.5 cpd/100tons. The last column shows the expected values for the different species based on other sources. The expected interaction rates for *pep* ν and CNO ν s are obtained from the latest High-Z (Low-Z) SSMs [60]. The expected rates for ^7Be ν interactions and ^{11}C decays are from the ^7Be ν analysis [25]. The expected ^{85}Kr rate comes from the delayed coincidence analysis [25]. The expected rates for ^{234m}Pa and ^{10}C and ^6He have already been presented in Tables 5.3 and 5.4, respectively. The expected rates from backgrounds from the PMTs (Table 5.5) are taken as lower limits on the total external background. No previous valid estimates for ^{210}Bi and ^{40}K are available.

Upper Limit (<i>pep</i> ν rate @ SSM)	CNO ν s interaction rate cpd/100tons	Solar CNO ν s flux $10^8 \text{cm}^{-2} \text{s}^{-1}$	% of total solar ν flux
68%	4.0 ± 1.3	3.9 ± 1.2	0.6 ± 0.2
95%	7.6 ± 1.2	7.4 ± 1.2	1.1 ± 0.2
99%	10.0 ± 1.1	9.7 ± 1.1	1.5 ± 0.2

Table 5.13: Upper limits for the CNO ν s interaction rate when the *pep* ν interaction rate is fixed at the SSM prediction of 2.8cpd/100tons. The corresponding $\Delta\chi^2$ profile can be seen in Fig. 5.20 (right). The uncertainties are systematic and were obtained following the methodology outlined in Sec. 5.10.3. The uncertainty introduced by the differences in the predicted *pep* ν flux from the High-Z and Low-Z SSMs is negligible.

Distributions considered	<i>pep</i> ν	^7Be ν	^{11}C	Ext. ^{214}Bi
Single energy spectrum	0.6 ± 2.8	50.2 ± 3.0	1.66 ± 0.60	0.64 ± 0.24
Only energy spectra	2.44 ± 0.80	49.9 ± 1.9	1.82 ± 0.48	0.40 ± 0.23
Energy spectra + radial dist	3.75 ± 0.96	50.0 ± 1.9	1.41 ± 0.41	0.73 ± 0.13
Energy spectra + PS-BDT	3.37 ± 0.55	48.4 ± 1.8	2.78 ± 0.17	0.44 ± 0.16
No complementary spectrum	3.45 ± 0.64	47.9 ± 1.8	2.46 ± 0.16	0.72 ± 0.13
All	3.33 ± 0.57	48.3 ± 1.7	2.48 ± 0.16	0.68 ± 0.12

Table 5.14: Differences in the central values and uncertainties of some characteristic species returned by the fit with the standard options (Tables 5.7, 5.9, 5.10 and 5.11) when different event distributions are included; the energy estimator is npe; central value and uncertainties are expressed in cpd/100tons. The ^{11}C rate presented corresponds to the one in the TFC-subtracted spectrum. The results from the last row are those from the full fit result presented in Fig. 5.16, 5.17 (right) and 5.18 (right). The uncertainty in the rates decrease as more distributions are considered. The distribution whose inclusion in the fit has the greatest effect in the *pep* ν interaction rate uncertainty is that of the PS-BDT parameter. Differences in the central values are also observed and, for the case of the ν interaction rates, these are smaller than the fit uncertainty.

in exposure than the rates for other species. Furthermore, we have included in this analysis many background species under the ^{11}C spectrum that were not in the ^7Be ν analysis, namely ^{10}C , ^6He , ^{234m}Pa and external γ -rays, which have taken over some of the counts in the ^{11}C energy range, leading to the observed smaller value for its decay rate.

Fig. 5.20 (right) shows the limits for the CNO ν s interaction rates after fixing the *pep* ν rate at the central value of the High-Z SSM prediction of 2.80 cpd/100tons. The variation in the result from fixing the *pep* ν interaction rate within the uncertainties of the SSMs, including the different predictions from the High-Z and Low-Z models, are smaller than the differences due to the choice of energy estimator. For the case of the npe variable, there is a non-zero central value at 2 cpd/100tons. The 68% U.L. does not change significantly, while the 95% and 99% U.L. become much stronger (see Table 5.13). The strong constraint in the CNO ν s interaction rate from fixing the *pep* ν rate to the SSM predictions is also evident in Fig. 5.24 (right).

Table 5.14 shows how the central values and uncertainties for some characteristic species in the fit change as different event distributions (Sec. 5.9.2, 5.9.3 and 5.9.4) are included in the fit. As expected, the larger the number of distributions considered, the smaller the uncertainty in the fitted rates. For the neutrino interaction rates, variations in the central values are smaller than the uncertainty returned by the fit, while for ^{11}C and external ^{214}Bi , which are background species in the PS-BDT and radial distribution fits, respectively (Table 5.7), their rates seem to be highly dependent on the inclusion of those distributions.

5.10.2 Validation of fit method and statistical uncertainties

The fit method and the reliability of the fit results have been validated with the use of data-like samples of known input composition. Using this method, we have tested the goodness of fit (Fig. 5.23), the absence of biases in the fit results and the reliability of the statistical uncertainty given by the fit (Fig. 5.23, right), the interpretation of the likelihood ratio test as a $\Delta\chi^2$ test (Fig. 5.24, left) and the frequentist interpretation of confidence limits (Fig. 5.24, right).

In order to create data-like samples, we simulate random events distributed with PDFs from the best fit to the data spectrum. Both energy spectra, PS-BDT and radial distributions of data-like events are simulated. The total number of events simulated is a random number from a Gaussian distribution with mean and variance equal to the number of events in the real data spectrum. For PS-BDT and radial distributions, the number of event to simulate in each bin is obtained from the energy spectrum in the corresponding energy range, and the distribution is obtained from the reference PDFs in that range. All the simulations of histograms have been constructed from the reference distribution using the `FillRandom` method of `TH1` class in ROOT [143]. The data-like samples have then been fitted with the same configuration as for the real data.

The goodness of the fit has been tested by comparing the minimum $-\ln L$ value obtained in the real data fit with the ones obtained from fits to the simulated data-like samples. The result of the goodness of fit test is shown in Fig. 5.23: the fit is good for both energy estimators and the p-value is ~ 0.3 .

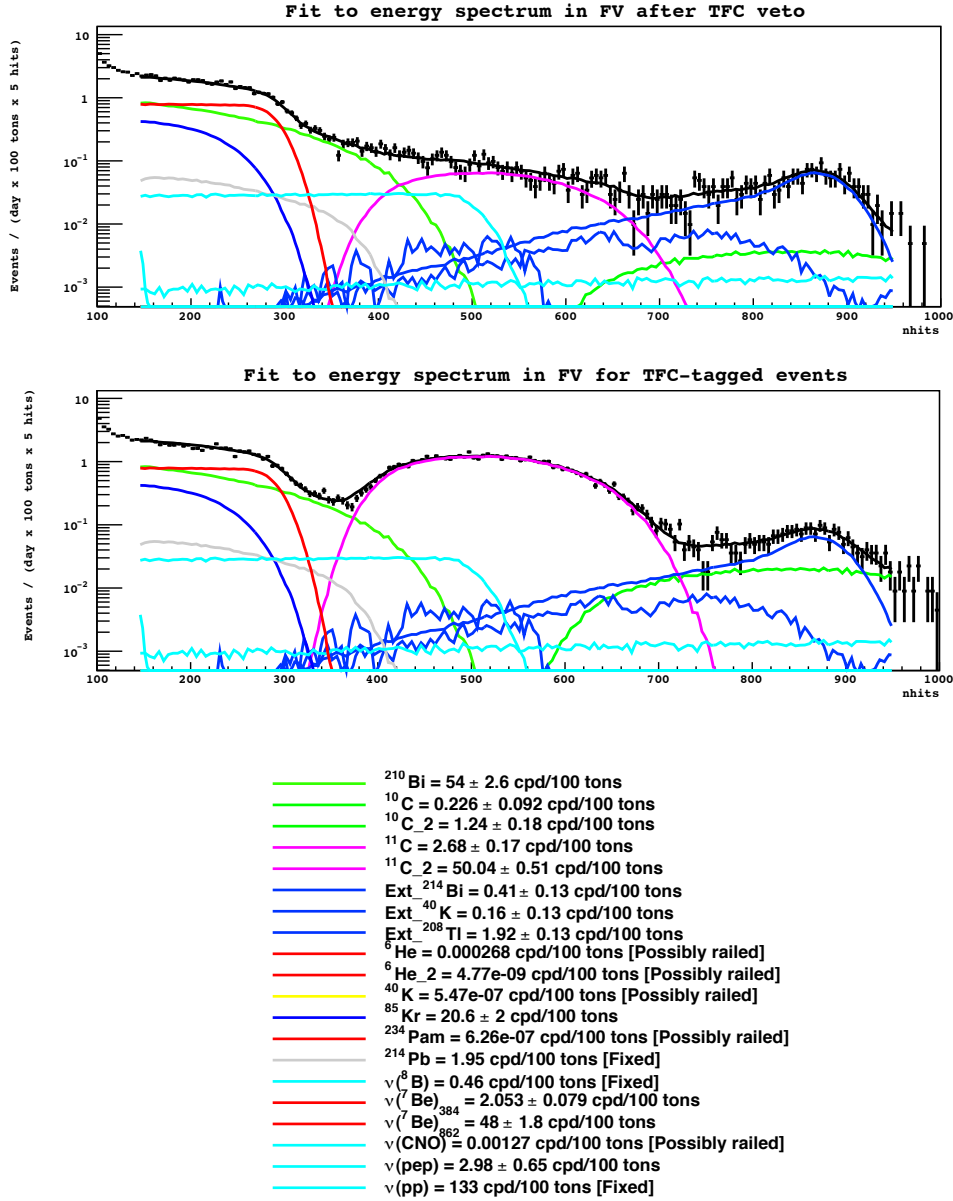


Figure 5.15: Energy spectra for the best fit result performed on the nhits energy estimator. The top panel shows the best fit to the TFC-subtracted spectrum, while the bottom presents the fit to the complementary, TFC-vetoed events. Details of the fit can be found in Sec. 5.9.2.6. The best-fit values for the rates of the species included in the fit are shown in the legend. For the species whose rates are independent in the two spectra, the names with the suffix “_2” correspond to those in the complementary spectrum. Limits for species that are labelled as “railed” can be found in Table 5.12.

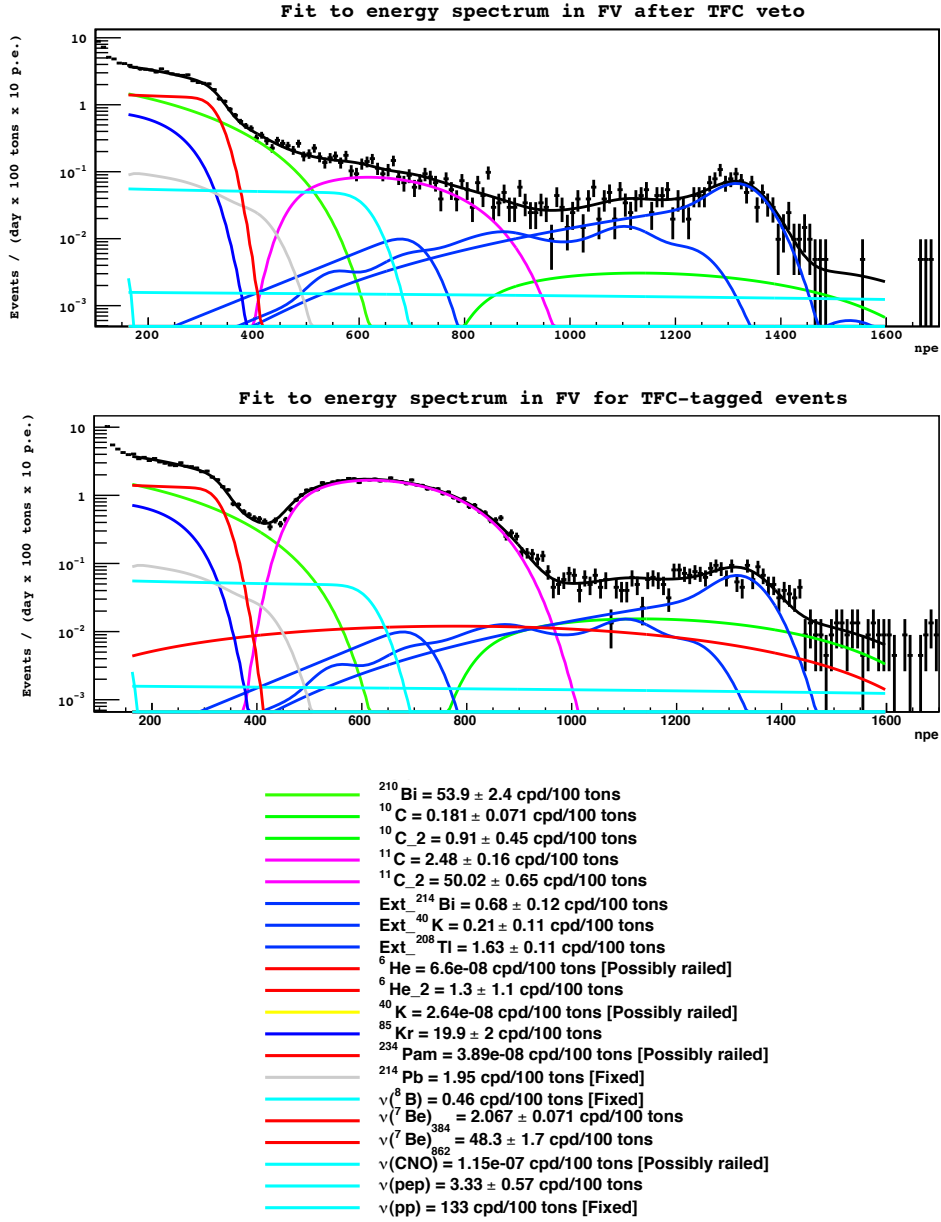


Figure 5.16: Energy spectra for the best fit result performed on the npe energy estimator. The top panel shows the best fit to the TFC-subtracted spectrum, while the bottom presents the fit to the complementary, TFC-vetoed events. Details of the fit can be found in Sec. 5.9.2.6. The best-fit values for the rates of the species included in the fit are shown in the legend. For the species whose rates are independent in the two spectra, the names with the suffix “_2” correspond to those in the complementary spectrum. Limits for species that are labelled as “railed” can be found in Table 5.12.

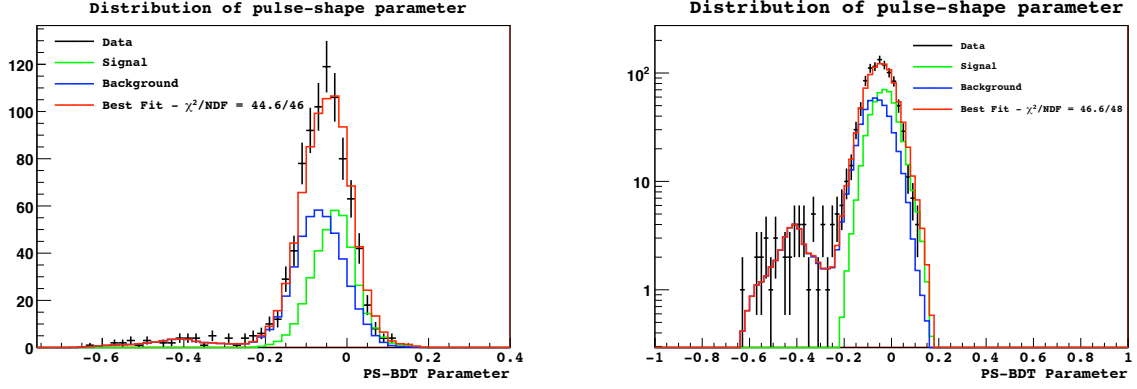


Figure 5.17: **Left panel:** Distribution of PS-BDT parameter in the energy range 400–650 nhits. **Right panel:** Distribution of PS-BDT parameter in the energy range 450–900 npe; the scale is logarithmic. In both cases, the total PDF distribution from the best-fit result is shown, as well as the result from a χ^2 -test to evaluate the goodness of the fit.

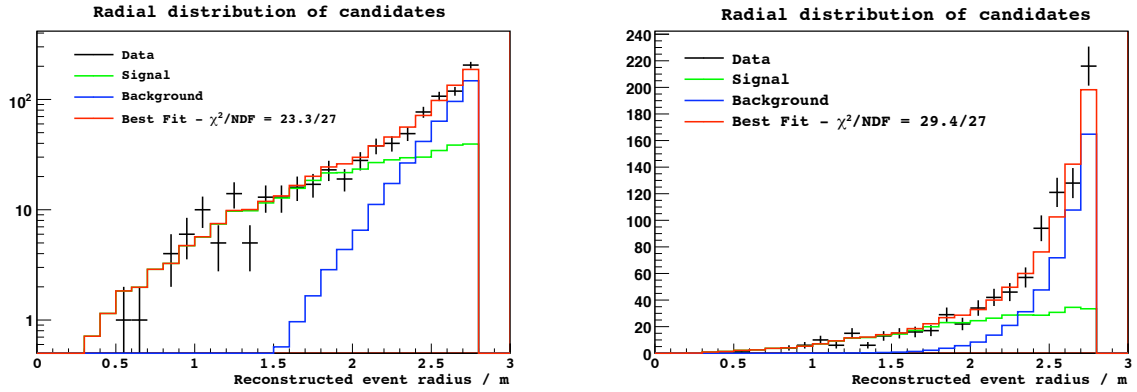


Figure 5.18: **Left panel:** Radial distribution of events in the energy range 500–900 nhits; the scale is logarithmic. **Right panel:** Radial distribution of events in the energy range 600–1400 npe. In both cases, the total PDF distribution from the best-fit result is shown, as well as the result from a χ^2 -test to evaluate the goodness of the fit.

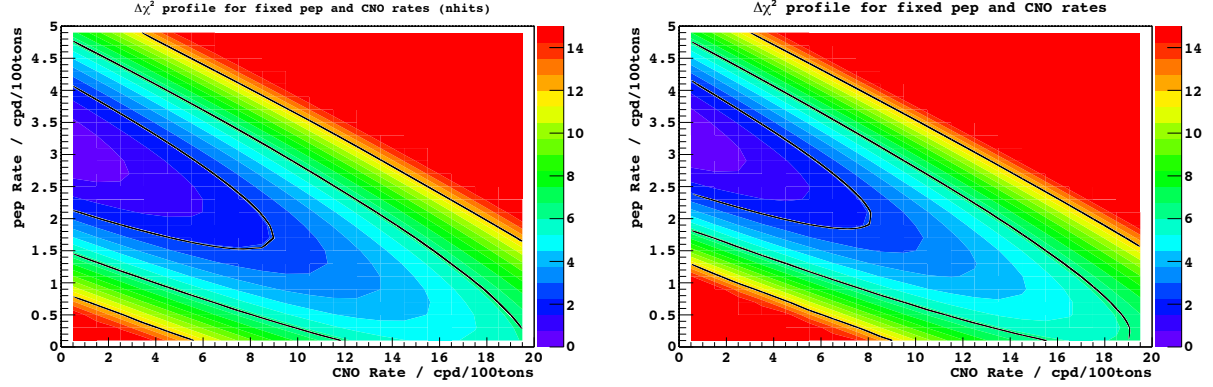


Figure 5.19: $\Delta\chi^2$ profile obtained from a likelihood-ratio test between the likelihood of the best-fit result and the maximum likelihood returned by the fit when pep ν and CNO ν s interaction rates are fixed to different values. The black lines on the plot represent the 1σ , 2σ and 3σ contours. This result was obtained starting from the best fit presented in Fig. 5.15 and 5.16. Systematic uncertainties are not included. **Left panel:** The fits were performed using the nhits energy estimator. **Right panel:** The fits were performed using the npe energy estimator.

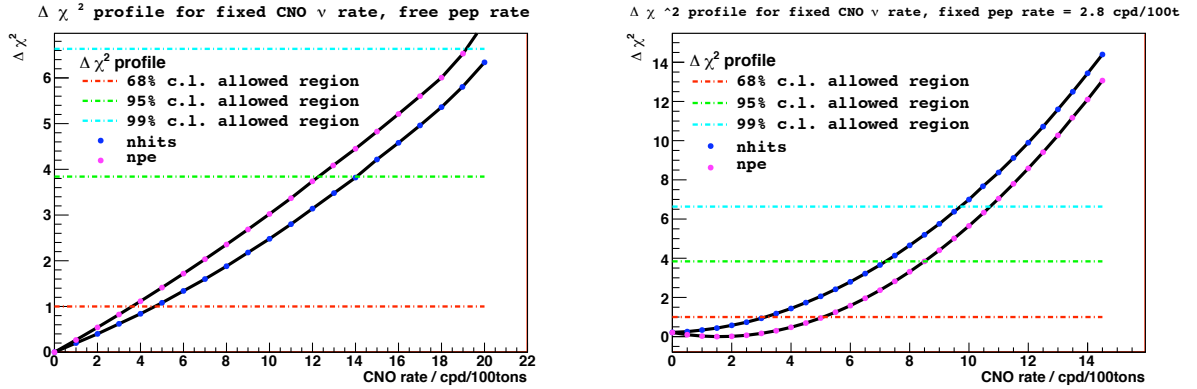


Figure 5.20: $\Delta\chi^2$ profile obtained from a likelihood-ratio test between the likelihood of the best-fit result and the maximum likelihood returned by the fit when the CNO ν s rate is fixed to different values. The blue (violet) points are the result of the test using nhits (npe) variable. Differences between npe and nhits are considered in the evaluation of the systematic uncertainty of the confidence limits. **Left panel:** the pep ν rate was left free in the fit (the best-fit value for the pep ν rate at fixed CNO ν s rate is displayed in Fig. 5.21); **Right panel:** the pep ν rate was fixed to the SSM High-Z prediction of 2.8 cpd/100tons (a similar test has also been performed by fixing the pep ν rate to the SSM Low-Z prediction of 2.86 cpd/100tons; the $\Delta\chi^2$ profile in this configuration is very similar).

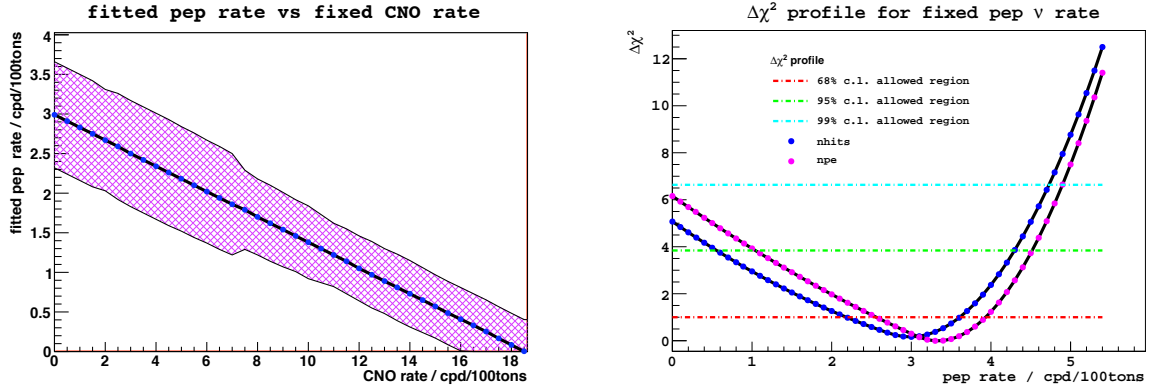


Figure 5.21: **Left panel:** $pep\ \nu$ interaction rate returned by the fit for different (fixed) CNO νs interaction rates. The shaded area is the statistical uncertainty. The fit has been performed using nhits energy estimator **Right panel:** $\Delta\chi^2$ profile obtained from a likelihood-ratio test between the likelihood of the best-fit result and the maximum likelihood returned by the fit when the $pep\ \nu$ rate is fixed to different values. The profiles are consistent with the returned values by the fit of 2.98 ± 0.65 (nhits) and 3.33 ± 0.57 (npe) cpd/100tons

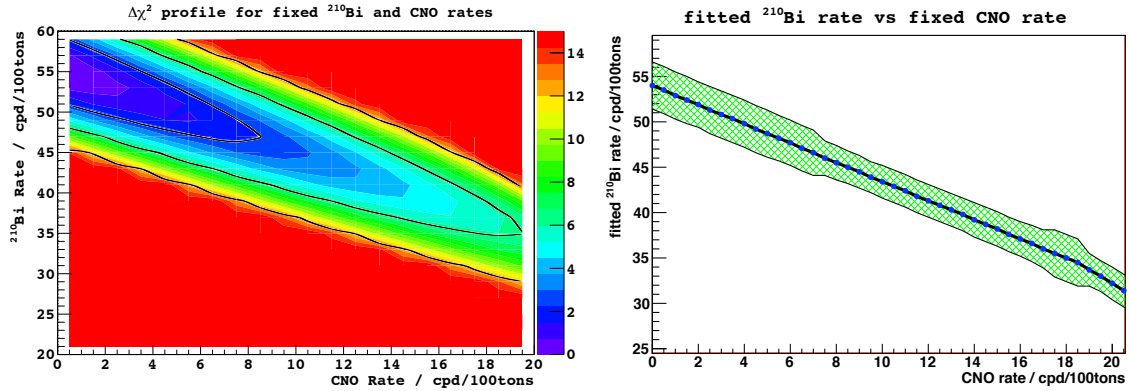


Figure 5.22: Correlation between CNO νs interaction rate and ^{210}Bi decay rate. **Left panel:** $\Delta\chi^2$ profile obtained from a likelihood-ratio test between the likelihood of the best-fit result and the maximum likelihood returned by the fit when ^{210}Bi and CNO νs interaction rates are fixed to different values. The black lines on the plot represent the 1σ , 2σ and 3σ contours. The fits were performed with the npe energy estimator. **Right panel:** ^{210}Bi rate returned by the fit for different (fixed) CNO νs interaction rate. The shaded area is the statistical (fit) uncertainty. The fits were performed using the nhits energy estimator. Another exercise was done with the $pep\ \nu$ interaction rate fixed to the SSM prediction of 2.8 cpd/100tons with very similar results.

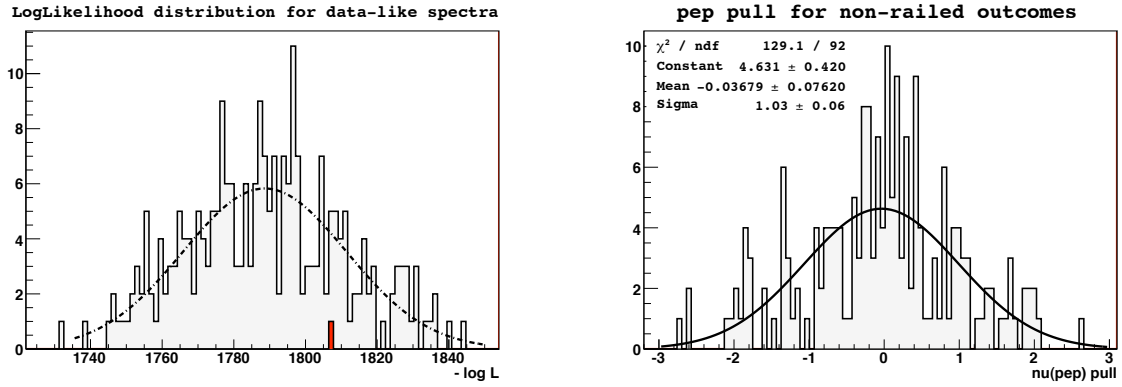


Figure 5.23: **Left panel:** $-\ln L$ distribution obtained fitting 250 data-like samples; the red entry is the minimum $-\ln L$ from the real data fit; the energy estimator is nhits;; **Right panel:** Pull distribution for the *pep* interaction rate, obtained from fitting 250 data-like samples of known input composition; the energy estimator is nhits. The outcomes are distributed as a Gaussian with the mean equal to the simulated interaction rate and the standard deviation equal to the uncertainty returned by the fit.

The central value and symmetric 1σ uncertainty for the *pep* ν interaction rate returned by the fit is consistent with the $\Delta\chi^2$ profile (Fig. 5.23, left). Yet, the standard interpretation of the uncertainty does not hold beyond 1σ , as the profile is asymmetric, with a smaller gradient to the left side of the central value and, therefore, a weaker constraint from below. We have also tested the absence of bias in the fit results and the reliability of the corresponding uncertainty by studying the distribution of the pulls for 250 data-like samples. The pull of a fit parameter is defined as the quantity: (fit parameter value - true parameter value)/(uncertainty on fit parameter). The pull for the *pep* ν interaction rate is shown in Fig. 5.23 (right): the outcomes of fits to data-like samples are distributed as a Gaussian consistent with the mean equal to the simulated *pep* ν rate and the standard deviation equal to the uncertainty returned by the fit.

The possibility of using the likelihood ratio test as a $\Delta\chi^2$ test has been checked by studying the distribution of the test's outcomes for data-like samples. In fact, if $\Delta 2\ln L$ can be interpreted as a $\Delta\chi^2$, the outcomes of the test should be distributed as a χ^2 distribution with the number of degrees of freedom equal to the decrease in the number of free parameters in the fit. To test this, we have simulated 100 data-like samples with the CNO ν s interaction rate at 10 cpd/100tons, and fitted twice, at first leaving CNO ν s rate free, and then fixing CNO ν s rate to the simulated value. For each simulated spectrum, we computed the $\Delta\chi^2$ using the minimum $-\ln L$ from the two fits. The outcomes of the $\Delta\chi^2$ are shown in Fig. 5.24 (left): the distribution follows a χ^2 distribution with one degree of freedom, as expected.

The frequentist interpretation of the CNO ν s interaction rate limits has been tested studying the distribution of CNO ν s interaction rate outcomes for 250 data-like samples. The outcomes of the data-like fits, shown in Fig. 5.24 (right), are compatible with the probability interpretation of the $\Delta\chi^2$ obtained from the likelihood ratio test in Fig. 5.20.

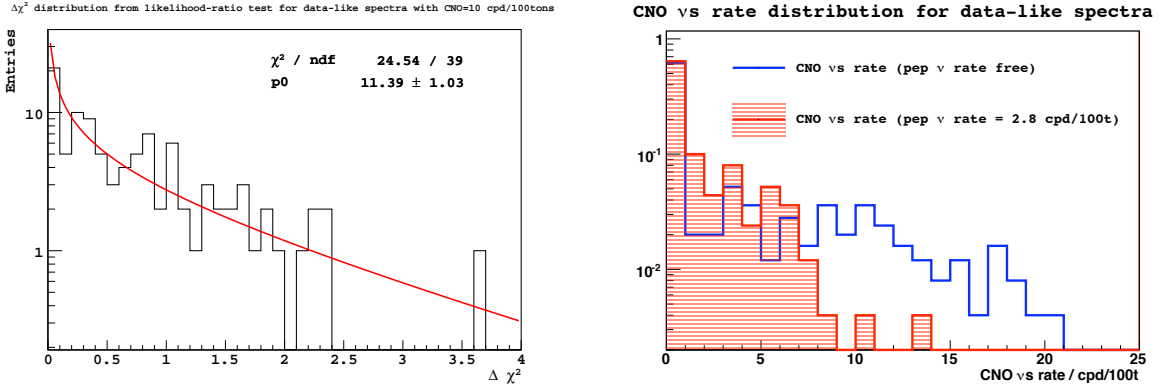


Figure 5.24: **Left:** $\Delta\chi^2$ distribution from likelihood-ratio tests to 100 data-like samples with the CNO ν s interaction rate simulated at 10 cpd/100tons. Each simulated spectrum has been fit with the standard options and again with the CNO ν s interaction rate fixed at the simulated value. The outcomes are distributed like a χ^2 distribution with 1 degree of freedom (red line), as expected. **Right:** Distribution of CNO ν s interaction rate outcomes, obtained from fitting 250 data-like samples with the spectral composition given by the best fit (Fig. 5.15); the fits have been done to distributions of the nhits energy estimator. The outcomes of the fits are compatible with the probability interpretation of the $\Delta\chi^2$ obtained from the likelihood ratio test in Fig. 5.20.

5.10.3 Systematic uncertainties

The sources of systematic uncertainties in this analysis, as well as the method to evaluate them, are very similar to the ones in the ${}^7\text{Be } \nu$ analysis (see [25] and the PhD thesis [119]). The estimated dominant sources of systematic uncertainties for the *pep* ν and CNO ν s interaction rates are listed in Table 5.15. The most relevant of these are the fit configuration (including the energy estimator used in the fit, Sec. 5.10.3.5) and the energy scale (Sec. 5.9.1, Sec. 5.10.3.3), which contribute a $\sim 7.3\%$ uncertainty in the *pep* ν rate. The uncertainty from the fiducial mass estimation (Sec. 5.5.2, Sec. 5.10.3.1) contributes with an additional $\sim 1\%$. The determination of the livetime and the relative exposure after the TFC veto (Sec. 5.5, Sec. 5.10.3.2) introduce an uncertainty $< 1\%$. Other negligible sources of systematic uncertainties, such as the difference in CNO ν s spectral composition (Sec. 5.2.2) and radioactive discussed not included in the fit (Sec. 5.3) have already been discussed.

5.10.3.1 Uncertainty from the fiducial mass determination

The evaluation of the systematic uncertainty related to the fiducial volume determination from position reconstruction has been performed in the same way as in the ${}^7\text{Be } \nu$ analysis [25, 119]. The uncertainty has been evaluated in two cases, using the same energy range of ${}^7\text{Be } \nu$ analysis, and a higher energy range that also includes electron recoils from *pep* ν and CNO ν s interactions (300–600 npe). The results are $+0.4, -1.1\%$ and $+0.6, -0.9\%$, respectively. Conservatively, we quote $+0.6, -1.1\%$ as the systematic uncertainty in the neutrino rates due to the fiducial mass determination.

Source of systematics uncertainty	% uncertainty	Absolute unc. cpd/100tons
Position Reconstruction	+0.6 -1.1	+0.01 -0.03
TFC veto & livetime determination	< 1	< 0.03
Energy variable & fit configuration	5.7	0.18
Energy response	4.1	0.13
Energy scale of Ext. γ	<1	0.01
γ -rays in pulse shape distributions	2.7	0.08
Low statistics in PS-BDT reference shapes	5.0	0.15
Inclusion of independent ^{85}Kr estimate	+3.9 -0.0	+0.12 -0.0
^{210}Bi spectral shape	+1.0 -5.0	+0.03 -0.15
Uncertainty in ^8B ν and <i>pp</i> ν flux	<1	0.01
Total Energy variable, energy scale, fit config.	7.3	0.23
Total Systematic Uncertainty	10.0	0.31

Table 5.15: Summary of the dominant systematic uncertainties in this analysis. The estimated value for the uncertainty in the *pep* ν interaction rate is shown; the absolute uncertainty corresponds to the central value of 3.13 cpd/100ton. The uncertainties introduced by these sources in the $\Delta\chi^2$ values for the CNO ν s interaction rate are shown in Table 5.16.

CNO ν s rate	$\Delta\chi^2$
4	1.0 ± 0.6
8	4.2 ± 1.3
10	6.7 ± 1.6

Table 5.16: Mean and rms of the $\Delta\chi^2$ distribution for the systematic tests when the CNO ν s interaction rate is fixed to different values. The $\Delta\chi^2$ was obtained from a likelihood ratio test with the result obtained when the CNO ν s rate was left free in the fit. The *pep* ν rate was always fixed to the SSM prediction of 2.8 cpd/100tons. The tests carried out include those summarised in Table 5.17, in addition to fits with PDFs for which the energy scale has been varied within uncertainty. Other sources of uncertainty, which are in common with the *pep* ν rate, are much smaller and can be neglected (see Table 5.15).

5.10.3.2 Uncertainty from the livetime and relative exposure

The computation of the livetime prior to the TFC veto has been performed in the same way of the ${}^7\text{Be}$ ν analysis [25]. The related systematic uncertainty is smaller than the loss of exposure due to fast coincidences (see the PhD thesis [119]), which has not been corrected for in this analysis. As this correction is much smaller than the systematic uncertainty arising from the fit configuration and energy scale (Table 5.15), a more precise evaluation is not necessary. The statistical uncertainty associated with the counting method used to estimate the relative exposure after the TFC vetoes (Sec. 5.5.3) is $< 0.5\%$, due to the large number of events considered (${}^{210}\text{Po}$ or simulated). The discrepancy between the two methods, which is $< 1\%$, is possibly due to systematic effects associated with the non-uniform spatial and time distribution of the ${}^{210}\text{Po}$ and can be considered an upper limit on the accuracy of the method. Overall, we quote an uncertainty in the exposure introduced by the livetime estimation and the TFC veto that is $< 1\%$.

5.10.3.3 Uncertainty from the energy scale

The calibration of the energy scale has been discussed in Sec. 4.3.1 and Sec. 5.9. To study the systematic uncertainty in the pep ν rate associated with it, we took different approaches for the different energy estimators.

For the nhits energy estimator, we performed fits using energy spectra PDFs with different energy scale parameters that are $\pm 2\sigma$ from the best-fit value, as determined by likelihood-ratio tests. For the light yield, the scaling used to produce the spectra was $\pm 0.2\%$ from the best fit value. We also considered a PDF with the light yield scaled by -0.4% and with the ${}^{11}\text{C}$ spectrum shifted by 4 hits, as well as one with worsened detector resolution. Considering the differences between the best-fit pep ν rate and those obtained from fits with these PDFs, we estimate a 1σ uncertainty in the pep ν interaction rate of 4.1% .

To estimate the corresponding uncertainty in the fit to the npe energy estimator, we have done a scan on the light yield about the best fit central value of 500 pe/MeV, noting the change in minimised $-\ln L$. We have kept the effective light yield of the external background species (in pe/MeV) and the starting point of the ${}^{11}\text{C}$ spectrum (in npe) to their best-fit values. The 1σ uncertainty in the light yield for uniform species is determined to be ± 2 pe/MeV and the associated uncertainty in the pep ν interaction rate is 1.7% . Additionally, to evaluate the effect of the energy resolution in the pep ν interaction rate, we performed a fit with the resolution parameters set to $+2\sigma$ of the result obtained from the fit to the ${}^{210}\text{Po}$ energy peak. The interaction rate increased by 0.3% , which is a negligible effect.

5.10.3.4 Energy scale of external background spectrum

In order to align the peak of the simulated ${}^{208}\text{Tl}$ energy spectrum (Sec. 5.8, Fig. 5.14), to the peak of the real data ${}^{208}\text{Tl}$, a shift of 5 nhits (over ~ 900 nhits) is needed. In order to evaluate the effect of the uncertainties of the external background energy scale, we have compared the results of the fit with the ${}^{208}\text{Tl}$ spectrum shifted of 5 nhits, the fit with no

Parameter	npe variable	nhits variable
Energy variable	npe	nhits
Bin width	5, 10	5, 10
Fit start point	160, 165, 170	140, 145, 150
Fit end point	1560–1640	920–960
PS-BDT Bin width	90, 100, 120	50, 110, 120
PS-BDT start point	400, 450	400–430
PS-BDT end point	880–900	620–680
PS-BDT Smoothing	180–220	180–220
Rdist Bin width	40, 50, 70	25, 40
Rdist start point	580–620	490–510
Rdist end point	1380–1440	890–910
^{214}Pb rate	1.95 ± 0.07	1.95 ± 0.07

Table 5.17: Variation in the parameter configuration of the fit for the systematics study. In the case of the ^{214}Pb rate, we vary the fixed rate according to a Gaussian distribution with the specified σ .

shift in ^{208}Tl spectrum, and the fit with a corresponding scale (instead of a shift) in the ^{208}Tl spectrum. For every of this checks, the change in *pep* ν fitted rate is less than 1%: in the first case (standard fit, 5 nhits shift), the *pep* ν rate is 2.98 ± 0.65 cpd/100tons, in the second case (no shift), the *pep* ν rate is 2.97 ± 0.66 cpd/100tons, in the third case (scale instead of shift) the *pep* ν rate is 2.99 ± 0.66 cpd/100tons. Also the ^{208}Tl fitted rate is changed by less than 1% among the three checks.

5.10.3.5 Uncertainty from the fit configuration

The fit method and fit parameters configuration has been described in Sec. 5.9. To study the stability of the fit under small variations in the configuration, and to evaluate the corresponding systematics uncertainties in the neutrino interaction rates, we performed a large number of fits, randomly changing the configuration parameters. We have taken the rms of the *pep* ν rate distribution as the systematic uncertainty from the fit configuration. For the case of the CNO ν s rate, where we quote upper limits, we have performed likelihood ratio tests under different fit configurations and from the resulting distribution of the $\Delta\chi^2$ obtained values for its mean and uncertainty (rms of the distribution). From these we can then extract the systematic uncertainty in the confidence limits. The range of allowed configuration parameters used to evaluate the systematic uncertainty is listed in Table 5.17. The energy estimator (and corresponding spectrum) used for the fit is included as one of the configuration parameters to vary. We quote 5.7% as the systematic uncertainty in the *pep* ν rate due to the fit configuration.

5.10.3.6 Uncertainty from the presence of γ -ray events in PS-BDT fit

In order to exclude from the PS-BDT distributions the ^{214}Bi events in the test sample that have some considerable contribution from γ -rays (Sec. 5.7.3), as well as most of the external γ -ray background from the data, we have decreased the energy end point of the PS-BDT fit to 700 npe. In this case, the resulting value for the *pep* ν rate in the npe fit changes from 3.33 ± 0.57 to 3.42 ± 0.51 cpd/100tons, a 2.7% increase in the central value.

5.10.3.7 Uncertainty from the limited statistics in reference PS-BDT distributions

The impact of the limited statistics in the reference PS-BDT distributions has been determined by performing fits where the bin content of the reference shapes was randomly modified according to Poisson statistics. We have taken the rms of the *pep* ν rate distribution as the systematic uncertainty from the fit configuration. The resulting *pep* ν interaction rate follows a Gaussian distribution with $\sigma/\mu = 0.05$. We quote 5% as the systematic uncertainty in the *pep* ν rate due to the limited statistics in the reference PS-BDT distributions.

5.10.3.8 Introduction of the independent ^{85}Kr estimate in the fit

As discussed in Sec. 5.10.1, the ^{85}Kr value returned by the fit is $\sim 2\sigma$ away from the independent measurement obtained in the coincidence analysis [25]. It is possible to include this information in the function to minimise in the fit. We have done this by adding a Gaussian-approximated term to the total negative log-likelihood:

$$-\ln L_G = \frac{(R - R_0)^2}{2\sigma_{R_0}^2} \quad (5.11)$$

where R is the rate in the fit and R_0 and σ_{R_0} are the central value and standard deviation of the independent constraint.

The resulting value for the *pep* ν rate in the npe fit is 3.46 ± 0.53 cpd/100tons, an increase in the central value of 3.9%. As expected, the best fit value from ^{85}Kr increases, from 19.9 ± 1.8 cpd/100tons to 21.3 ± 1.8 cpd/100tons.

5.10.3.9 Uncertainty from ^{210}Bi spectral shape

We have taken particular care in studying the uncertainty in the ^{210}Bi spectrum, as it could potentially have a large systematic effect in the *pep* ν and CNO ν s interaction rate results, as it offers a significant contribution to the count rate near the *pep* ν shoulder, the region which is crucial for determining the neutrino rates. We have performed different fits, using ^{210}Bi spectral shapes with correction factors $C(W)$ obtained from different experimental measurements [144, 145, 146, 147]. We quote as +1.0% –5.0% the systematic uncertainty due to the ^{210}Bi spectral shape.

5.10.3.10 Uncertainty from the fixed solar ν species

The *pp* ν and ^8B ν rate in the fit are fixed to the High-Z SSM prediction (see Sec. 5.9.2 and Table 5.7)[60]. In order to evaluate the correlation of *pp* ν and ^8B ν rate with the *pep* ν value in the fit, and in particular whether the result is stable under the uncertainties of the SSM predicted flux for ^8B ν , we have performed some fits to the nhits spectrum with different fixed values of *pp* ν and ^8B ν . The *pp* ν fixed rate has been changed by $\pm 2\%$ (~ 4 -5 times the SSM uncertainty); this resulted in no change at all in the *pep* fitted value. The ^8B ν fixed rate has been changed by $\pm 30\%$ (~ 3 times the SSM uncertainty); the *pep* ν rate fitted value changes by less than 1%, from 2.98 ± 0.65 cpd/100tons to 3.00 ± 0.65 cpd/100tons when the ^8B ν rate is increased by 30%, and to 2.97 ± 0.66 when the ^8B ν rate is decreased by 30%. These checks shows the minimal impact that fixing *pp* ν and ^8B ν rates has in the results. In particular, floating the ^8B ν flux to any SSM prediction or experimental measurement does not change the result. Therefore, over reasonable ranges of parameter space, the result can be taken to be uncorrelated to those inputs.

5.10.4 Consistency checks

This section describes some of the checks we performed in order to prove the consistency and the stability of the analysis.

5.10.4.1 Exclusion of Period 8

In February 2010 the new Laben firmware was installed, which led to a 1–2% increase in the nhits variable. No change in the npe spectrum was observed but the extra hits may have an effect in the position reconstruction and Gatti parameter, which could affect the data selection cuts (Sec. 5.5). In order to understand the impact of the new firmware in our analysis, we have performed the fit to the data excluding Period 8, which includes the data acquired after the new firmware was introduced and accounts for $\sim 10\%$ of the exposure (Table 5.6). In the case of the npe variable, the fitted *pep* rate increases by 1% to 3.36 ± 0.60 cpd/100tons, while for the nhits variable it increases by 3.6%, from 2.98 ± 0.65 cpd/100tons to 3.09 ± 0.67 cpd/100tons. The $\Delta\chi^2$ profile and the limits for the CNO ν s rate are very close to the one in Fig. 5.20. In both cases the ^{210}Bi rate is 8% lower and the ^7Be ν rate decreases by 4% to 46 ± 2 cpd/100 tons. This may be related to the high ^7Be ν rate obtained from a fit to Period 8 in the ^7Be ν analysis [119].

5.10.4.2 Starting point at ^7Be analysis value

For this analysis, we have chosen the starting point of the fit at 160 npe, which is higher than that used in the ^7Be ν analysis, based on the robustness of the fit under small changes of this parameter. If we decrease the starting point to 140 npe (for the ^7Be ν analysis the value was 145 npe), the fit returns an interaction rate for the ^7Be ν (0.862 MeV) of 46.7 ± 1.6 cpd/100tons, much closer to the value obtained in the ^7Be ν analysis [25], and a value for the *pep* ν interaction rate of 3.20 ± 0.53 cpd/100tons, a decrease of 3.9%.

ν	Interaction rate [counts/(day·100ton)]	Solar- ν flux [$10^8\text{cm}^{-2}\text{s}^{-1}$]	Data/SSM ratio
<i>pep</i>	$3.1 \pm 0.6_{\text{stat}} \pm 0.3_{\text{syst}}$	1.6 ± 0.3	1.1 ± 0.2
CNO	< 7.9 ($< 7.1_{\text{stat only}}$)	< 7.7	< 1.5

Table 5.18: The best estimates for the *pep* and CNO solar neutrino interaction rates. The statistical uncertainties are not Gaussian as can be seen in Fig. 5.19 and in Fig. 5.21 (right). For the results in the last two columns both statistical and systematic uncertainties are considered. Total fluxes have been obtained assuming MSW-LMA and using the scattering cross-sections from [2, 104, 148] and a scintillator e^- density of $(3.307 \pm 0.003) \times 10^{29} \text{ ton}^{-1}$. The last column gives the ratio between our measurement and the High Metallicity (GS98) SSM [60].

5.10.4.3 Inclusion of uncertainties due to statistical α subtraction

As mentioned in Sec. 5.9.1, for the main result in this analysis, we have ignored the uncertainty introduced by the statistical subtraction of α -like events (Sec 5.5.4). To check that this indeed does not affect our result, we have performed a fit to the npe spectrum with the negative log-likelihood term modified to a Gaussian approximation (analogous to Eq. 5.11) for bins in which the uncertainty squared is greater than the bin content i.e. the uncertainty is not the Poisson uncertainty. As the bins affected by the procedure are those in the ^{210}Po energy region, where the content of β -like events is large, as they are below the end point of the electron recoil spectrum from ^7Be ν neutrinos, the Gaussian approximation should be good. The results are as expected, the likelihood of the best fit decreases and the largest effect is in the uncertainties of the ^{85}Kr and ^7Be ν neutrino rates, whose values change from 19.9 ± 1.8 cpd/100tons to 19.9 ± 2.0 cpd/100tons and 48.3 ± 1.7 cpd/100tons to 48.2 ± 2.0 cpd/100tons, respectively. The *pep* ν rate increases by 1%, from 3.33 ± 0.57 cpd/100tons to 3.36 ± 0.57 cpd/100tons.

5.10.5 The flux of *pep* and CNO solar neutrinos

Table 5.18 summarises the results for the *pep* and CNO neutrino interaction rates. The absence of the solar neutrino signal is rejected at 99.97% C.L. using a likelihood ratio test between the result when the *pep* and CNO neutrino interaction rates were fixed to zero and the best-fit result, as discussed in Sec. 5.10.1. Likewise, the absence of a *pep* neutrino signal is rejected at 98% C.L. Due to the similarity between the e^- recoil spectrum from CNO neutrinos and the spectral shape of ^{210}Bi decay, whose rate is ~ 10 times greater, we can only provide an upper limit on the CNO ν s interaction rate. The 95% C.L. limit reported in Table 5.18 has been obtained from a likelihood ratio test with the *pep* ν rate fixed to the SSM prediction [60] under the assumption of MSW-LMA, (2.80 ± 0.04) counts/(day·100ton), which leads to the strongest test of the solar metallicity.

Table 5.18 also shows the solar neutrino fluxes inferred from our best estimates of the *pep* and CNO neutrino interaction rates, assuming the MSW-LMA solution, and the

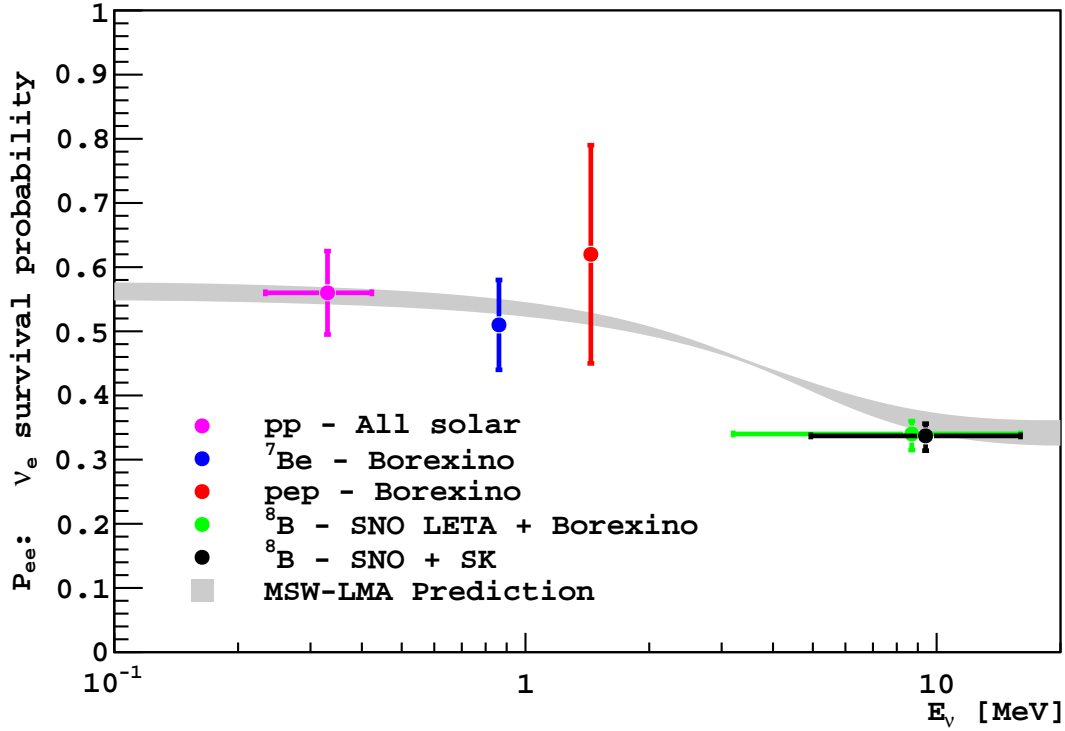


Figure 5.25: Electron neutrino survival probability (P_{ee}) as a function of energy. The red line corresponds to the measurement presented in this PhD thesis. The pp and ^7Be measurements of P_{ee} given in [25] are also shown. The ^8B ν measurements of P_{ee} were obtained from [21, 24, 81], as indicated in the legend. The MSW-LMA prediction band is the 1σ range of the mixing parameters given in [2].

ratio of these values to the High Metallicity (GS98) SSM predictions [60]. Both results are consistent with the predicted High and Low Metallicity SSM fluxes assuming MSW-LMA. Under the assumption of no neutrino flavor oscillations, we would expect a pep neutrino interaction rate in Borexino of (4.47 ± 0.05) counts/(day·100ton); the observed interaction rate disfavors this hypothesis at 97% C.L. If this discrepancy is due to ν_e oscillation to ν_μ or ν_τ we find $P_{ee} = 0.62 \pm 0.17$ at 1.44 MeV. This result is shown alongside other solar neutrino P_{ee} measurements and the MSW-LMA prediction in Fig. 5.25.

5.11 Conclusions and outlook

We have achieved the necessary sensitivity to provide, for the first time, evidence of the signal from pep neutrinos and to place the strongest constraint on the CNO neutrino flux to date. This has been made possible by the combination of low levels of intrinsic background in Borexino and the implementation of novel background discrimination techniques. The result for the pep neutrino interaction rate does not yet have the sufficient precision to disentangle between the P_{ee} predictions of various oscillation models, and the constraint on the CNO neutrino flux cannot yet discern between the High and

Low Metallicity SSM. However, the success in the reduction of ^{11}C background raises the prospect for higher precision measurements of pep and CNO neutrino interaction rates by Borexino after further running, especially if the next dominant background, ^{210}Bi , is reduced by scintillator re-purification.

Chapter 6

Conclusions

The Borexino experiment has achieved the necessary sensitivity to provide, for the first time, evidence of the rare signal from *pep* neutrinos and to place the strongest constraint on the CNO neutrino flux to date. The absence of the *pep* and CNO solar neutrino interaction is rejected at 99.97% C.L., likewise the absence of a *pep* neutrino signal is rejected at 98% C.L. Due to the small statistics sample and the similarity between the electron recoil spectrum of CNO solar neutrinos and the spectral shape of the internal radioactive contaminant ^{210}Bi whose rate is ~ 10 times greater, only an upper limit on the CNO interactions could be provided.

The rate of the *pep* solar neutrino interactions in Borexino is 3.1 ± 0.6 (stat) ± 0.3 (syst) counts/(day·100ton). Assuming the *pep* neutrino flux predicted by the Solar Standard Model, the constraint on the CNO solar neutrino interaction rate is 7.9 counts/(day·100ton) at 95% C.L. Assuming the MSW-LMA solution to solar neutrino oscillations, these values correspond to solar neutrino fluxes of $(1.6 \pm 0.3) \times 10^8 \text{ cm}^{-2}\text{s}^{-1}$ and $7.7 \times 10^8 \text{ cm}^{-2}\text{s}^{-1}$, respectively, in agreement with both High and Low Metallicity Standard Solar Models. These results represent the first direct evidence of the *pep* neutrino signal and the strongest constraint of the CNO solar neutrino flux to date.

Under the assumption of no neutrino flavor oscillations, we would expect a *pep* neutrino interaction rate in Borexino of (4.47 ± 0.05) counts/(day·100ton); the observed interaction rate disfavors this hypothesis at 97% C.L. If this discrepancy is due to ν_e oscillation to ν_μ or ν_τ we find $P_{ee} = 0.62 \pm 0.17$ at 1.44 MeV.

Bibliography

- [1] G. Bellini et al. First evidence of *pep* solar neutrinos by direct detection in Borexino. *Phys. Rev. Lett.*, 108:051302, 2012. III, 4, 31, 35
- [2] K. Nakamura et al. The Review of Particle Physics. *J. Phys. G.*, 37:075021, 2010. 1, 3, 5, 6, 10, 11, 13, 35, 70, 95, 100, 119, 120
- [3] C.L. Cowan, F.B. Reines, H.W. Kruse, and A.D. McGuire. Detection of the Free Neutrino: a Confirmation. *Science*, 124:103–104, 1956. 1
- [4] G. Danby et al. Final tau-neutrino results from the DONuT experiment. *Phys. Rev. D*, 78:052002, 2008. 1, 2
- [5] K. Kodama et al. Observation of High-Energy Neutrino Reactions and the Existence of Two Kinds of Neutrinos. *Phys. Rev. Lett.*, 9:36–44, 1962. 1
- [6] John N. Bahcall. *Neutrino Astrophysics*. Cambridge University Press, 1989. 1, 15, 16, 17, 18, 20, 22, 23
- [7] Lawrence M. Krauss, Sheldon L. Glashow, and David N. Schramm. Antineutrino astronomy and geophysics. *Nature*, 310:191–198, 1984. 2
- [8] Thomas K. Gaisser. *Cosmic rays and particle physics*. Cambridge University Press, 1990. 2
- [9] K.S. Hirata et al. Observation of a neutrino burst from the supernova SN1987A. *Phys. Rev. Lett.*, 58:1490, 1987. 2
- [10] M. Malek et al. Search for Supernova Relic Neutrinos at Super-Kamiokande. *Phys. Rev. Lett.*, 90:061101, Feb 2003. 2
- [11] K. Schreckenbach, G. Colvin, W. Gelletly, and F. Von Feilitzsch. Determination of the Anti-Neutrino Spectrum from U-235 Thermal Neutron Fission Products up to 9.5-MeV. *Phys. Lett.*, B160:325–330, 1985. 2
- [12] A. A. Hahn et al. Anti-Neutrino Spectra from Pu-241 and Pu-239 Thermal Neutron Fission Products. *Phys. Lett.*, B218:365–368, 1989. 2
- [13] B. Pontecorvo. Neutrino Experiments and the Problem of Conservation of Leptonic Charge. *Sov. Phys. JETP*, 26:984–988, 1968. 4

- [14] B.T. Cleveland et al. Measurement of the Solar Electron Neutrino Flux with the Homestake Chlorine Detector. *Astrophys. J.*, 496:505, 1988. 4, 22
- [15] Y. Fukuda et al. Solar Neutrino Data Covering Solar Cycle 22. *Phys. Rev. Lett.*, 77:1683, 1996. 4
- [16] P. Anselmann et al. Solar neutrinos observed by GALLEX at Gran Sasso. *Phys. Lett.*, B285:376–389, 1992. 4, 26
- [17] W. Hampel et al. GALLEX solar neutrino observations: Results for GALLEX IV. *Phys. Lett. B*, 447:127, 1999. 4, 26
- [18] M. Altman et al. Complete results for five years of GNO solar neutrino observations. *Phys. Lett. B*, 616:174, 2005. 4, 26
- [19] A. Abdurashitov et al. Measurement of the solar neutrino capture rate with Gallium metal, Part III. *Phys. Rev. C*, 80:015807, 2009. 4, 26
- [20] S. Fukuda et al. Determination of solar neutrino oscillation parameters using 1496 days of Super-Kamiokande I data. *Phys. Lett. B*, 539:179–187, 2002. 4
- [21] J. P. Cravens et al. Solar neutrino measurements in Super-Kamiokande-II. *Phys. Rev. D*, 78:032002, Aug 2008. 4, 27, 120
- [22] Q.R. Ahmad et al. Measurement of the Rate of $\nu_e + d \rightarrow p + p + e^-$ Interactions Produced by ^8B Solar Neutrinos at the Sudbury Neutrino Observatory. *Phys. Rev. Lett.*, 87:071301, 2001. 4, 15, 22, 27, 28
- [23] Q.R. Ahmad et al. Direct Evidence for Neutrino Flavor Transformation from Neutral-Current Interactions in the Sudbury Neutrino Observatory. *Phys. Rev. Lett.*, 89:011301, 2002. 4, 15, 22, 27, 28
- [24] B. Aharmim et al. Low Energy Threshold Analysis of the Phase I and Phase II Data Sets of the Sudbury Neutrino Observatory. *Phys. Rev. C*, 81:055504, 2010. 4, 120
- [25] G. Bellini et al. Precision Measurement of the ^7Be Solar Neutrino Interaction Rate in Borexino. *Phys. Rev. Lett.*, 107:141302, Sep 2011. 4, 21, 27, 31, 35, 36, 42, 43, 55, 57, 60, 67, 69, 71, 72, 73, 79, 82, 99, 100, 103, 104, 113, 115, 117, 118, 120
- [26] G. Bellini et al. Absence of a day-night asymmetry in the ^7Be solar neutrino rate in Borexino. *Phys. Lett. B*, 707:22–26, 2012. 4, 25, 28, 31, 35
- [27] Y. Fukuda et al. Evidence for Oscillation of Atmospheric Neutrinos. *Phys. Rev. Lett.*, 81:1562, 1998. 4
- [28] Y. Ashie et al. Evidence for an Oscillatory Signature in Atmospheric Neutrino Oscillations. *Phys. Rev. Lett.*, 93:101801, 2004. 4

- [29] K. Eguchi et al. First Results from KamLAND: Evidence for Reactor Anti-Neutrino Disappearance. *Phys. Rev. Lett.*, 90:021802, 2003. 4, 28
- [30] T. Araki et al. Measurement of Neutrino Oscillation with KamLAND: Evidence of Spectral Distortion. *Phys. Rev. Lett.*, 94:081801, 2005. 4
- [31] S. Abe et al. Precision Measurement of Neutrino Oscillation Parameters with KamLAND. *Phys. Rev. Lett.*, 100:221803, 2008. 4, 13
- [32] Y. Abe et al. Indication for the disappearance of reactor electron antineutrinos in the Double Chooz experiment. arXiv:1112.6353 [hep-ph], 2011. 4, 12
- [33] M.H. Ahn et al. Measurement of neutrino oscillation by the K2K experiment. *Phys. Rev. D*, 74:072003, 2006. 4
- [34] D.G. Miceal et al. Observation of Muon Neutrino Disappearance with the MINOS Detectors in the NuMI Neutrino Beam. *Phys. Rev. Lett.*, 97:191801, 2006. 4
- [35] P. Adamson et al. Measurement of Neutrino Oscillations with the MINOS Detectors in the NuMI Beam. *Phys. Rev. Lett.*, 101:131802, 2008. 4
- [36] P. Adamson et al. Improved search for muon-neutrino to electron-neutrino oscillations in MINOS. *Phys. Rev. Lett.*, 107:181802, 2011. 4, 12
- [37] N. Agafonova et al. Observation of a first ν_τ candidate in the OPERA experiment in the CNGS beam. *Phys. Lett. B*, 691:138, 2010. 4
- [38] K. Abe et al. Indication of Electron Neutrino Appearance from an Accelerator-Produced Off-Axis Muon Neutrino Beam. *Phys. Rev. Lett.*, 107:041801, 2011. 4, 12
- [39] G. Pontecorvo. Mesonium and anti-mesonium. *Sov. Phys. JETP*, 6:429, 1957. 4, 5
- [40] Z. Maki, M. Nakagawa, and S. Sakata. Remarks on the unified model of elementary particles. *Prog. Theor. Phys.*, 28:870, 1962. 4, 5
- [41] L. Wolfenstein. Neutrino oscillations in matter. *Phys. Rev. D*, 107:2369, 1978. 5, 6, 8, 9, 24, 28
- [42] S. Mikheev and A.Y. Smirnov. Resonance enhancement of oscillations in matter and solar neutrino spectroscopy. *Sov. J. Nucl. Phys.*, 42:913, 1985. 5, 6, 9, 24, 25, 28
- [43] E.Kh. Akhmedov and A.Y. Smirnov. Paradoxes of neutrino oscillations. *Phys. Atom. Nucl.*, 72:1363, 2009. 5
- [44] V. Gribov and B. Pontecorvo. Neutrino astronomy and lepton charge. *Phys. Lett. B*, 28:493, 1969. 7

- [45] V. Barger et al. Matter effects on three-neutrino oscillations. *Phys. Lett. D*, 22:2718, 1980. 8, 9
- [46] P. Langacker et al. On the Mikheyev-Smirnov-Wolfenstein (MSW) Mechanism of Amplification of Neutrino Oscillations in Matter. *Nucl. Phys. B*, 282:589, 1987. 10
- [47] A. Aguilar et al. Evidence for neutrino oscillations from the observation of anti-neutrino(electron) appearance in a anti-neutrino(muon) beam. *Phys. Rev. D*, 64:112007, 2001. 10
- [48] A.A. Aguilar-Arevalo et al. Search for Electron Neutrino Appearance at the $\Delta m^2 \sim 1 \text{ eV}^2$ Scale. *Phys. Rev. Lett.*, 98:231801, 2007. 10
- [49] The ALEPH Collaboration, The DELPHI Collaboration, The L3 Collaboration, The OPAL Collaboration, The SLD Collaboration, The LEP Electroweak Working Group, and The SLD Electroweak and Heavy Flavour Groups. Precision electroweak measurements on the Z resonance. *Physics Report*, 427:257–454, 2006. 10
- [50] F. Boehm et al. Final results from the Palo Verde neutrino oscillation experiment. *Phys. Rev. D*, 64:112001, 2001. 12
- [51] M. Apollonio et al. Search for neutrino oscillations on a long base-line at the CHOOZ nuclear power station. *Eur. Phys. J. C*, 27:331–374, 2003. 12
- [52] The Daya Bay Collaboration. A Precision Measurement of the Neutrino Mixing Angle θ_{13} using Reactor Antineutrinos at Daya Bay. arXiv:0701029 [hep-ph], 2007. 12
- [53] J.K. Ahn et al. RENO: An Experiment for Neutrino Oscillation Parameter θ_{13} Using Reactor Neutrinos at Yonggwang. arXiv:1003.1391[hep-ph], 2010. 12
- [54] S.M. Bilenky and S.T. Petcov. Massive neutrinos and neutrino oscillations. *Rev. Mod. Phys.*, 59:671, 1987. 13
- [55] R. Davis, D.S. Harmer, and K.C. Hoffman. Search for Neutrinos from the Sun. *Phys. Rev. Lett.*, 20:1205, 1968. 15, 22, 26
- [56] Raymond Davis. Solar Neutrinos. II. Experimental. *Phys. Rev. Lett.*, 12:303–305, Mar 1964. 15
- [57] J.N. Bahcall, A.M. Serenelli, and S Basu. New Solar Opacities, Abundances, Helioseismology and Neutrino Fluxes. *Astrophys. J. Suppl.*, 621:L85, 2005. 17, 19, 28
- [58] J.N. Bahcall, A.M. Serenelli, and S Basu. 10,000 Standard Solar Models: A Monte Carlo Simulation. *Astrophys. J. Suppl.*, 165:400, 2006. 17, 23, 68, 70

- [59] C. Pena-Garay and A.M. Serenelli. Solar neutrinos and the solar composition problem. arXiv: 0811.2424[astro-ph], accepted for publication on PRL, 2008. 17, 18, 35
- [60] A. Serenelli, W. Haxton, and C. Peña-Garay. Solar models with accretion. I. Application to the solar abundance problem. *The Astrophysical Journal*, 743:24, 2011. 17, 18, 20, 68, 69, 70, 72, 98, 104, 118, 119, 120
- [61] N. Grevesse and A.J. Sauval. Standard Solar Composition. *Space Sci. Rev.*, 85:161, 1998. 17
- [62] M. Asplund, N. Grevesse, and A. J. Sauval. The Solar Chemical Composition. *ASP Conference Series*, 336:25, 2005. 17, 18
- [63] M. Asplund, N. Grevesse, A. J. Sauval, and P. Scott. New solar composition: the problem with solar models revisited. *The Astrophysical Journal Letters*, 705:123, 2009. 17, 18
- [64] S. Basu. The Solar Metallicity Problem: What is the Solution? In *Proc. GONG 2008/SOHO XXI Solar-stellar dynamos as revealed by helio and asteroseismology*, volume 416, page 193, 2009. 17, 18
- [65] C. Allende Prieto and D. Lambert. The Forbidden abundance of oxygen in the Sun. *Astrophys. J.*, 556:L63–L66, 2001. 17
- [66] C. Allende Prieto and D. Lambert. A reappraisal of the solar photospheric C/O ratio. *Astrophys. J.*, 573:L137–L140, 2002. 17
- [67] M. Asplund, N. Grevesse, A. J. Sauval, C. Allende Prieto, and D. Kiselman. Line formation in solar granulation. IV. [O I], O I and OH lines and the photospheric O abundance. *Astronomy and Astrophysics*, 417:751–768, 2004. 17
- [68] M. Asplund, N. Grevesse, A. J. Sauval, C. Allende Prieto, and R. Blomme. Line formation in solar granulation. VI. [C I], C I, CH and C2 lines and the photospheric C abundance. *Astronomy and Astrophysics*, 431:693–705, 2005. 17
- [69] M. Asplund. Line formation in solar granulation. III. The photospheric Si and meteoritic Fe abundances. *Astronomy and Astrophysics*, 359:755–758, 2000. 17
- [70] John N. Bahcall. The luminosity constraint on solar neutrino fluxes. *Phys. Rev. C*, 65:025801, 2002. 20
- [71] C. Casella et al. First Measurement of the $d(p,\gamma)^3\text{He}$ cross section down to the solar Gamow peak. *Nucl. Phys. A*, 706:203–216, 2002. 21
- [72] M. Junker et al. Cross section of $^3\text{He}(^3\text{He},2p)^4\text{He}$ measured at solar energies. *Phys. Rev. C*, 57:2700–2710, May 1998. 21
- [73] R. Bonetti et al. First Measurement of the $^3\text{He}(^3\text{He},2p)^4\text{He}$ Cross Section down to the Lower Edge of the Solar Gamow Peak. *Phys. Rev. Lett.*, 82:5205–5208, Jun 1999. 21

- [74] D. Bemmerer et al. Activation Measurement of the ${}^3\text{He}(\alpha,\gamma){}^7\text{Be}$ Cross Section at Low Energy. *Phys. Rev. Lett.*, 97:122502, Sep 2006. 21
- [75] H. Costantini et al. The ${}^3\text{He}(\alpha,\gamma){}^7\text{Be}$ S-factor at solar energies: The prompt γ experiment at LUNA. *Nucl. Phys. A*, 814:144–158, 2008. 21
- [76] Y. Fukuda et al. Solar ${}^8\text{B}$ and hep Neutrino Measurements from 1258 Days of Super-Kamiokande Data. *Phys. Rev. Lett.*, 86:5651, 2001. 21, 28
- [77] The Borexino Collaboration. Direct Measurement of the ${}^7\text{Be}$ Solar Neutrino Flux with 192 Days of Borexino Data. *Phys. Rev. Lett.*, 101:091302, 2008. 21, 27, 43, 57
- [78] C. Arpesella et al. First real time detection of ${}^7\text{Be}$ solar neutrinos by Borexino. *Phys. Lett.*, B658:101–108, 2008. 21, 27, 57
- [79] B. Aharmim et al. Electron energy spectra, fluxes, and day-night asymmetries of ${}^8\text{B}$ solar neutrinos from measurements with NaCl dissolved in the heavy-water detector at the Sudbury Neutrino Observatory. *Phys. Rev. C*, 72:055502, 2005. 22, 27, 28
- [80] B. Aharmim et al. An Independent Measurement of the Total Active ${}^8\text{B}$ Solar Neutrino Flux Using an Array of ${}^3\text{He}$ Proportional Counters at the Sudbury Neutrino Observatory. *Phys. Rev. Lett.*, 101:111301, 2008. 22, 27
- [81] G. Bellini et al. Measurement of the solar ${}^8\text{B}$ neutrino rate with a liquid scintillator target and 3 Mev energy threshold in the Borexino detector. *Phys. Rev. D*, 82:033006, Aug 2010. 22, 27, 31, 35, 73, 74, 120
- [82] A. Formicola et al. Astrophysical S-factor of ${}^{14}\text{N}(\text{p},\gamma){}^{15}\text{O}$. *Phys. Lett. B*, 591:61–68, 2008. 23
- [83] M. Marta et al. The ${}^{14}\text{N}(\text{p},\gamma){}^{15}\text{O}$ reaction studied with a composite germanium detector. *Phys. Rev. C*, 83:045804, Apr 2011. 23
- [84] P. J. LeBlanc et al. Constraining the S factor of ${}^{15}\text{N}(\text{p},\gamma){}^{16}\text{O}$ at astrophysical energies. *Phys. Rev. C*, 82:055804, Nov 2010. 23
- [85] S.T. Petcov. Analytic treatment of high-order adiabatic approximations of two-neutrino oscillations in matter. *Phys. Lett. B*, 200:373, 1988. 24
- [86] M. Bruggen, Haxton W.C., and Quian Y.Z. Landau-zener treatments of solar neutrino oscillations. *Phys. Rev. D*, 51:4028, 1995. 24, 25
- [87] A.Yu Smirnov and S.P. Mikheev. Neutrino Oscillations In Matter With Varying Density. In *Proc. of the VIth Moriond Workshop on Massive Neutrinos in Astrophysics and Particle Physics*, page 355, 1986. 24
- [88] S. Toshev. Exact analytical solution of the two-neutrino evolution equation in matter with exponentially varying density. *Phys. Lett. B*, 196:170, 1987. 24

- [89] S.T. Petcov. Exact analytic description of neutrino oscillations in matter with an exponentially varying density for an arbitrary number of neutrino species. *Phys. Lett. B*, 214:259, 1988. 25
- [90] S.P. Mikheev and A.Y. Smirnov. 3 ν oscillations in matter and solar neutrino data. *Phys. Lett. B*, 200:560, 1987. 25
- [91] G. Pontecorvo. report PD-205. Technical report, Chalk River Lab., 1946. 26
- [92] A.I. Abazov et al. Search for neutrinos from sun using the reaction Ga-71 (electron-neutrino e-) Ge-71. *Phys. Rev. Lett.*, 67:3332, 1991. 26
- [93] K.S. Hirata et al. Observation of ^8B solar neutrinos in the Kamiokande-II detector. *Phys. Rev. Lett.*, 63:16, 1989. 27
- [94] Y. Fukuda et al. Measurements of the Solar Neutrino Flux from Super-Kamiokande's First 300 Days. *Phys. Rev. Lett.*, 81:1158, 1998. 27
- [95] J. Hosaka et al. Solar neutrino measurements in Super-Kamiokande-I. *Phys. Rev. D*, 73:112001, 2006. 27
- [96] G. Alimonti et al. The Borexino detector at the Laboratori Nazionali del Gran Sasso. *Nucl. Instr. and Meth. A*, 600:568–593, 2009. 27, 31, 35, 36, 37, 53, 63, 71
- [97] John N. Bahcall, M.C. Gonzalez-Garcia, and C. Pena-Garay. Solar neutrinos before and after KamLAND. *JHEP*, 02:009, 2003. 28
- [98] B. Aharmim et al. Combined Analysis of all Three Phases of Solar Neutrino Data from the Sudbury Neutrino Observatory. arXiv: 1109.0763[hep-ph], 2011. 28, 29
- [99] G. Bellini et al. Study of solar and other unknown anti-neutrino fluxes with Borexino at LNGS. *Phys. Lett. B*, 696:191–196, 2011. 31
- [100] G. Bellini et al. Observation of Geo-Neutrinos. *Phys. Lett. B*, 687:299–304, 2010. 31, 72, 73, 75
- [101] G. Bellini et al. New experimental limits on the Pauli-forbidden transitions in ^{12}C nuclei obtained with 485 days Borexino data. *Phys. Rev. C*, 81:034317, Mar 2010. 31
- [102] G. Alimonti et al. Ultra-low background measurements in a large volume underground detector. *Astropart. Phys.*, 8:141–157, 1998. 32
- [103] G. Alimonti et al. A large-scale low-background liquid scintillation detector: the counting test facility at Gran Sasso. *Nucl. Instr. and Meth. A*, 406:411–426, 1998. 32
- [104] John N. Bahcall. Solar neutrinos: Radiative corrections in neutrino-electron scattering experiments. *Phys. Rev. D*, 51:6151–6158, 1995. 34, 100, 119

- [105] G. Bellini et al. Muon and Cosmogenic Neutron Detection in Borexino. *JINST*, 6:P05005, 2011. 35, 36, 59, 75, 82
- [106] G. Alimonti et al. Science and technology of Borexino: a real-time detector for low energy solar neutrinos. *Astropart. Phys.*, 16:205–234, 2002. 35, 36
- [107] J. Benzinger et al. A Scintillator Purification System for the Borexino Solar Neutrino Detector. *Nucl. Instr. and Meth. A*, 587:277–291, 2008. 35, 36, 73
- [108] G. Alimonti et al. The liquid handling systems for the Borexino solar neutrino detector. *Nucl. Instr. and Meth. A*, 609:58–78, 2009. 35, 36
- [109] F. Elisei et al. Measurements of liquid scintillator properties for the borexino detector. *Nucl. Instr. Met. A*, 400:53–68, 1997. 35, 37, 51
- [110] M. Chen et al. Quenching of undesired fluorescence in a liquid scintillator particle detector. *Nucl. Instr. and Meth. A*, 420:189–201, 1999. 35
- [111] G. Alimonti et al. Light propagation in a large volume liquid scintillator. *Nucl. Instr. and Meth. A*, 440:360–371, 2000. 35, 37, 52
- [112] J. Benizinger et al. The nylon scintillator containment vessels for the Borexino solar neutrino experiment. *Nucl. Instr. and Meth. A*, 582:509–534, 2007. 35, 76
- [113] A. Ianni et al. The Measurements of 2200 ETL9351 type photomultipliers for the Borexino experiment with the photomultiplier testing facility at LNGS. *Nucl. Instr. and Meth. A*, 537:683–697, 2005. 35, 52
- [114] A. Brigatti et al. The Photomultiplier tube testing facility for the Borexino experiment at LNGS. *Nucl. Instr. and Meth. A*, 537:521, 2005. 35
- [115] J.B. Birks. *Photophysics of Aromatic Molecules*. Wiley-Interscience, 1970. 37, 38, 50
- [116] H.O. Back et al. Pulse-Shape discrimination with the Counting Test Facility. *Nucl. Instr. and Meth. A*, 584:98–113, 2008. 39
- [117] E. Gatti and F. De Martini. A New Linear Method of Discrimination between Elementary Particles in Scintillation Counters. *Nuclear Electronics*, 2:265–276, 1962. 39, 40
- [118] Stefano Perasso. *Monte Carlo based measurement of the ^7Be solar neutrino flux in Borexino*. PhD thesis, Università degli Studi di Genova, 2010. 40, 84, 99
- [119] Richard Saldanha. *Precision measurement of the ^7Be Solar Neutrino Interaction Rate in Borexino*. PhD thesis, Princeton University, January 2012. 40, 78, 84, 99, 100, 102, 113, 115, 118
- [120] Y. Kino et al. Positron Annihilation in Liquid Scintillator for Electron Antineutrino Detection. *Jour. Nucl. Radiochem. Sci.*, 1:63, 200. 40, 48

- [121] D. Franco et al. Positronium signature in organic liquid scintillators for neutrino experiments. *Phys. Rev. C*, 83:015504, 2011. 41, 48, 87, 88, 89
- [122] G. Alimonti et al. Measurement of the ^{14}C abundance in a low-background liquid scintillator. *Nucl. Instr. Meth. A*, 406:411–426, 1998. 42
- [123] C. Galbiati et al. Cosmogenic ^{11}C production and sensitivity of organic scintillator detectors to pep and CNO neutrinos. *Phys. Rev. C*, 71:055805, 2005. 42, 81
- [124] Werner Maneschg. *Low-energy solar neutrino spectroscopy with Borexino : Towards the detection of the solar pep and CNO neutrino flux*. PhD thesis, MPI fuer Kernphysik, May 2011. 45, 55, 93
- [125] W. Maneschg et al. Production and characterization of a custom-made ^{228}Th source with reduced neutron source strength for the Borexino experiment. arXiv:1110.1217[physics.ins-det], 2011. 45, 55, 93
- [126] A. Agostinelli et al. GEANT4 – a simulation toolkit. *Nucl. Instr. Meth. A*, 506:250–303, 2003. 47
- [127] John Bahcall. John Bahcall website <http://www.sns.ias.edu/~jnb/>, 2005. 48
- [128] P.C. de Holanda et al. Toward precision measurements in solar neutrinos. arXiv:0404042v3 [hep-ph], 2004. 48, 100
- [129] J.K. Tuli. Evaluated Nuclear Structure Data File. Technical report, Brookhaven National Laboratory, April 1987. 48
- [130] W. Maneschg. Comparison of the particle generators and rdm/snu in the Borexino simulation package G4bx. Borexino Internal Memo, 2010. 48, 100
- [131] F. Rohrlich and B.C. Carlson. Positron-Electron Difference in Energy Loss and Multiple Scattering. *Phys. Rev.*, 93:38, 1954. 51
- [132] H. Gumus. New stopping power formula for intermediate energy electrons. *Appl. Radiat. Isot.*, 66:1886–1890, 2008. 51
- [133] L. Oberauer, C. Grieb, F. von Feilitzsch, and I. Manno. Light concentrators for Borexino and CTF. *Nucl. Instr. and Meth. A*, 530:453–462, 2004. 52
- [134] Steven E. Hardy. *Measuring the ^7Be Neutrino Flux From the Sun: Calibration of the Borexino Solar Neutrino Detector*. PhD thesis, Virginia Polytechnic Institute and State University, March 2010. 55, 57, 58
- [135] O.Ju Smirnov. An approximation of the ideal scintillation detector line shape with a generalized gamma distribution. *Nucl. Instr. and Meth.*, 595:410–418, 2008. 61
- [136] S. Abe et al. Study of the Production of Radioactive Isotopes through Cosmic Muon Spallation in KamLAND. *Phys. Rev. C*, 81:025807, 2010. 74

- [137] C. Arpesella et al. Measurements of extremely low radioactivity levels in BOREXINO. *Astropart. Phys.*, 18:1–25, 2002. 76, 93, 103
- [138] Margherita Buizza Avanzini. *The ^8B Solar Neutrino Analysis in Borexino and Simulations of Muon Interaction Products in Borexino and Double Chooz*. PhD thesis, Università degli Studi di Milano, 2011. 76
- [139] B. Caccianiga et al. Minutes of the Meetings. Internal Memo of the Borexino ^7Be Cuts Committee, 2010. 77, 78
- [140] M. Deutsh. Proposal for a Cosmic Ray Detection System for the Borexino Solar Neutrino Experiment. Technical report, Massachusetts Institute of Technology, 1996. 82
- [141] H.O. Back et al. CNO and pep neutrino spectroscopy in Borexino: Measurement of the deep-underground production of cosmogenic ^{11}C in an organic liquid scintillator. *Phys. Rev. C*, 74:045805, 2006. 82
- [142] A. Hoecker and others. TMVA 4 Toolkit for Multivariate Data Analysis with ROOT Users Guide <http://tmva.sourceforge.net/docu/TMVAUsersGuide.pdf>, nov 2009. 88
- [143] R. Brun and others. ROOT: A Data Analysis Framework <http://root.cern.ch>, jun 2011. 88, 106
- [144] E. Plassmann and Langer L. Das β -Spektrum Des RaE. *Nucl. Phys.*, 31:293, 1962. 100, 117
- [145] E. Plassmann and Langer L. Beta Spectrum of Radium E. *Phys. Rev.*, 96:6, 1954. 117
- [146] A. Grau Charles and Grau Malonda A. Precision measurement of the RaE shape factor. *Nucl. Phys. A*, 596:83, 1996. 117
- [147] A. Grau Charles. Beta shapefactor determinations by the cutoff energy yield method. *Nucl. Instr. Meth. A*, 551:312, 2005. 117
- [148] J. Erler and M.J. Ramsey-Musolf. The Weak Mixing Angle at Low Energies. *Phys. Rev. D*, 72:073003, 2005. 119

Acknowledgements

Un gran numero di persone meritano una menzione di ringraziamento; alcune hanno contribuito significativamente a questo importante risultato, altre mi hanno sostenuto o mi hanno aiutato, altre ancora hanno avuto un importante ruolo nei miei anni da dottorando.

Una menzione particolare è per il mio relatore, Marco Pallavicini. Marco è un fisico da Serie A e i suoi insegnamenti, sia diretti che indiretti, sono davvero preziosi e mi hanno aiutato a crescere come fisico. O almeno, questa è la mia opinione.

Un ringraziamento dal profondo dell'animo va alla nostra imperatrice Gemma Testera. Con Gemma ho lavorato davvero bene e mi sono divertito parecchio. Gemma è piena di qualità che la rendono eccezionale come donna e come fisica, e lavorare fianco a fianco con lei mi ha aiutato a sviluppare le mie abilità da fisico.

Special thanks to the members of the *Borexino pep dream team* which I so proudly belong.

To Alvaro, one of the brighter physicist I have ever met. Without Alvaro the result of the *pep* analysis would be extremely less significant. Those days in June and July, when we made this analysis converge, were extremely tough. However, I bring with me an extremely good memory of those days. The satisfaction for the accomplishment of the analysis, carried out on that sleepless night before the General Meeting, is going to be one of the greatest emotions in my career as a physicist.

To Richard, because it is easy to work with Richard, and his knowledge and skill are extremely precious. The help you gave us with the fitter is priceless.

A Davide, perché con Davide lavoro sempre molto bene, ed è sempre un piacere chiacchierare con lui. Mi sono divertito parecchio nelle *pep* week e le varie volte che abbiamo collaborato a Genova, Milano o Gran Sasso. Sono felice che questa collaborazione continuerà nella mia prossima avventura in Dark Side.

Ad Alessandro, perché è un mostro di bravura e di competenza, e mi consiglia spesso letture interessanti. Si impara sempre qualcosa da Alessandro, anche solo per osmosi. Mi sono divertito nei periodi al Gran Sasso, e spero sarà così anche in futuro.

A Margherita, perché è un'ottima fisica e una vera donna. La tua abilità nel simulare qualsiasi cosa in qualsiasi situazione e impiegando una frazione di tempo trascurabile is really amazing. Purtroppo la nostra collaborazione si fermerà, almeno per qualche anno, ma auguro a te e alla piccola Elicottera tutta la serenità e la gioia che vi meritate.

And finally to the Dark Lord Cristiano, *Commander in Chief* of the *pep* working group and external advisor of my thesis. Cristiano is a skilled politician and manager.

His management of the *pep* working group was outstanding.

I want to thank a large number of people within the Borexino collaboration.

Livia, mi diverto sempre con te, nonostante i miei occhi siano in costante pericolo ogni volta che sei nelle vicinanze. Lavorare con te è stato piacevole, ed è stato molto piacevole seguire insieme la scuola estiva a Varenna. Magari un giorno davvero riusciremo a riscrivere la RunValidation macro.

Sandra, i lunghissimi viaggi Arenzano – Genova sarebbero stati interminabili senza di te.

George, the God of Electronics. Thanks for the constant help during my months as Run Coordinator.

Pablo, porque la pasión de la noche está caliente como una espada de fuego.

Amanda, because she brings happiness to the cold winter days in Assergi, and because she has an amazing superpower.

Yusuke, arigato gozaimasu. Kaizoku oni ore wa naru.

Alex, for his very useful comments about the *pep* and CNO analysis and the paper.

Tizio, Caio e Sempronio per l'aiuto costante durante questi anni.

Un ringraziamento alle persone a Genova che mi piace incrociare nei corridoi o nei rispettivi uffici.

Marco B, fisico teorico di rara qualità e calcolatore umano spesso più affidabile di Mathematica. Chiacchierare con Marco è sempre un piacere, e spero che un giorno i nostri percorsi convergano nuovamente alla stessa Università.

Sara B (che non è di Genova, ma è isomorfa a Genova grazie a Marco), anche se le piace troppo la statistica Bayesiana.

Giulia perché sei sempre un faro di riferimento, e hai svolto tutta la burocrazia per questa tesi al posto mio.

Giovanni (Ridolfi) per avermi insegnato quello che so sulla teoria quantistica dei campi e la rinormalizzazione, e per aver letto i capitoli introduttivi di questa tesi.

Gabriele Filipelli e la sua *crew*, per tutte le chiacchierate quando giravo per il dipartimento in cerca di ispirazione (o mentre attendevo i risultati di qualche simulazione), e per la stima che mi dimostrate quando mi chiedete opinioni o delucidazioni su qualsiasi argomento inerente alla fisica.

Alessio e Guido, che hanno spesso buoni consigli da elargire.

Quello lì, quella là e quegli altri perché è bello incontrare facce familiari al DiFi.

Special thanks to Son Goku, because he always protect our planet from evil menaces like Saiyans, Freezer, Cell, and Majin Bu. Also, many thanks to Eiichiro Oda because every week I can read a new amazing chapter of One Piece.

Alcune persone speciali che meritano un ringraziamento particolare.

Mamma e Papà, perché altrimenti non esisterei, e il mio Zio.

Francesca, è stato bello essere il relatore della tua tesi. Mi dispiace che non sarai una dottoranda in Borexino, ma sono felice che continuerai a frequentare i Laboratori nella tua nuova avventura lunare.

Carlotta, per aver reso più piacevoli i lunghi inverni Abruzzesi, la lontana fuga a New York e la calda estate Spagnola.

Marzia, la mia gemellina. E' bello capirci al volo e grazie per tutte le volte che mi hai ascoltato e tutti i consigli che mi hai dato. Mi raccomando, non fare cazzate.

Irena, la mia sorellina. Penso che tu sia una fisica molto promettente. Mi piacerebbe lavorare insieme a te in un futuro. E' sempre un piacere chiacchierare con te e scambiarsi consigli su qualsiasi cosa. Ricorderò con piacere la fuga da Varenna.

Il ringraziamento più importante è per la mia preziosissima creatura meravigliosa. Hai reso questi tre anni degni di essere vissuti. Sei il Sole che illumina le mie giornate. Grazie per tutte le piccole e grandi cose che condividiamo, per tutte le gioie che riesci a regalarmi, per la tua stessa esistenza.